



NTNU – Trondheim
Norwegian University of
Science and Technology

Impact behaviour of stiffened aluminium plates

Bente Larsen Kårstad
Birgitte Skajaa

Civil and Environmental Engineering

Submission date: June 2015

Supervisor: Magnus Langseth, KT

Co-supervisor: Odd Sture Hopperstad, KT
David Morin, KT

Norwegian University of Science and Technology
Department of Structural Engineering



MASTER THESIS 2015

SUBJECT AREA: Structural mechanics	DATE: June 14 th 2015	NO. OF PAGES: 22+134+31
---------------------------------------	-------------------------------------	----------------------------

TITLE:

Impact behaviour of stiffened aluminium plates

Oppførsel til avstivede platefelt i aluminium utsatt for støtlaster

BY:

Bente Larsen Kårstad and
Birgitte Skajaa



SUMMARY:

In this master thesis, impact loading against stiffened aluminium plates of the aluminium alloy AA6082-T6 was studied. The main objective was to study the behaviour of extruded aluminium profiles welded together when exposed to impact loading from a ship, and how to model it in a large scale analysis. The study was part of a cooperation between SIMLab at NTNU, Hydro Aluminium and Sapa, as a part of the project "Coastal Highway Route E39".

Eight plates were tested in the laboratory experiment, four by applying quasi-static loading and four by applying dynamic loading, with a cylindrical indenter in the centre of the plate, transversal and longitudinal to the stiffeners. The dynamic experiments were conducted using the kicking machine at the Department of Structural Engineering, NTNU. The experiments were attempted simulated and validated using shell elements in a nonlinear element analysis in Abaqus/Explicit. In order to perform the laboratory experiments, a rig fixing the aluminium plates in the test machine was designed.

In the experiments a good correlation was detected between the quasi-static and dynamic tests. This gave grounds to conclude that quasi-static experiments could give satisfying validation for this type of experiment on the aluminium alloy, AA6082-T6.

The numerical model was implemented with two different criteria to detect fracture, the Cockcroft-Latham (CL) fracture criterion and the Bressan-Williams-Hill (BWH) instability criterion. The material implementation was simplified by using the von Mises yield criterion, where the anisotropic properties of the AA6082-T6 were neglected. The CL fracture criterion gave acceptable estimates of initiation of fracture when the mesh size is equal to the thickness of the plate. With a coarser mesh, the accuracy of this criterion decreased significantly. The BWH instability criterion gave acceptable estimates of initiation of fracture for mesh sizes varying from equal to the thickness to five times the thickness. The estimates showed to be somewhat conservative for this criterion, and a slight mesh sensitivity was detected.

In the material tests, a large degree of anisotropy was detected for aluminium alloy AA6082-T6, and a large difference between the material properties in the plate, stiffeners and the friction stir welds was found. This made the material implementation more complicated than first assumed, and the simplification with an isotropic yield criterion less accurate. An anisotropic yield criterion would more accurately describe the material behavior in the experiments, and could therefore give improved estimates.

RESPONSIBLE TEACHER: Magnus Langseth

SUPERVISOR(S): Magnus Langseth, Odd Sture Hopperstad and David Morin

CARRIED OUT AT: Norwegian University of Science and Technology (NTNU)



MASTEROPPGAVE 2015

FAGOMRÅDE: Beregningsmekanikk	DATO: 14.06.2015	ANTALL SIDER: 22+134+31
----------------------------------	---------------------	----------------------------

TITTEL:

Oppførsel til avstivede platefelt i aluminium utsatt for støtlaster

Impact behaviour of stiffened aluminium plates

UTFØRT AV:

Bente Larsen Kårstad og
Birgitte Skajaa



SAMMENDRAG:

I denne masteroppgaven har oppførselen til avstivede platefelt av aluminiumlegeringen AA6082-T6 utsatt for støtlaster blitt studert. Hovedmålet var å vurdere oppførselen av sveiste aluminiumprofiler utsatt for støtlaster fra et skip, og videre vurdere hvordan de kan modelleres i en storskala analyse. Denne masteroppgaven var en del av et samarbeid mellom SIMLab ved NTNU, Hydro Aluminium og Sapa, som en del av prosjektet "Fergefri E39".

Åtte plater ble testet i laboratoriet, fire under kvasi-statisk belastning og fire under dynamisk belastning, med en sylindrisk nese som traff tversgående og langsgående i forhold til stivere, midt i platefeltet. De dynamiske forsøkene ble utført i Sparkemaskinen ved Institutt for konstruksjonsteknikk, NTNU. Forsøkene ble forsøkt simulert og validert ved å anvende skallelementer i en ikkelineær analyse i Abaqus/Explicit. For å kunne utføre laboratorieforsøkene ble en rigg utformet for innfesting av aluminiumsplatene i testmaskinen.

I eksperimentene ble det observert god korrelasjon mellom de kvasi-statiske og dynamiske testene. Dette ga grunnlag for å kunne konkludere med at kvasi-statiske eksperimenter kan gi tilfredsstillende validering for denne type forsøk på aluminiumslegering AA6082, med temper T6.

Den numeriske modellen ble gjennomført med to ulike kriterium for å beskrive brudd, bruddkriteriet Cockcroft-Latham (CL) og instabilitetskriteriet Bressan-Williams-Hill (BWH). Materialmodellen ble forenklet ved å implementere det isotrope flytekriteriet von Mises, hvor de anisotrope egenskapene til AA6082-T6 blir neglisjert. CL-bruddkriteriet ga akseptable estimat for oppstart av brudd når elementstørrelsen i den numeriske modellen er lik tykkelsen av platen. Med større elementer minket nøyaktigheten av dette kriteriet betraktelig. Instabilitetskriteriet BWH, viste akseptable estimater for oppstart av brudd for varierende elementstørrelser, fra lik tykkelsen til fem ganger tykkelsen. Estimaten var noe konservative for dette kriteriet, og en viss sensitivitet i forhold til elementstørrelsen ble oppdaget.

I materialtestene ble det observert en stor grad av anisotropi i aluminiumslegering AA6082-T6, og det ble funnet en stor forskjell mellom materialegenskapene i platen, stiverene og friksjonsveisene. Dette gjorde implementeringen av materialet i den numeriske modellen mer komplisert enn først antatt, og forenklingen med et isotropt flytekriterium mindre nøyaktig. For å kunne bedre gjenskape flyteflaten og dermed oppførselen av materialet i forsøkene burde et anisotrop flytekriterium bli implementert.

FAGLÆRER: Magnus Langseth

VEILEDER(E): Magnus Langseth, Odd Sture Hopperstad og David Morin

UTFØRT VED: Norges Teknisk Naturvitenskapelige Universitet (NTNU)

MASTEROPPGAVE 2015

for

Bente Larsen Kårstad og Birgitte Skajaa

Oppførsel til avstivede platefelt i aluminium utsatt for støtlaster

Impact behaviour of stiffened aluminium plates

Samferdselsdepartementet har bedt Statens vegvesen om å utrede hvilket potensiale en fergefri E39 vil ha for næringsliv og tilhørende bo- og arbeidsregioner. Prosjektet skal også vurdere teknologiske løsninger for fjordkryssinger, og hvordan konstruksjonene eventuelt kan utnyttes til å produsere energi fra sol, bølger, strøm og vind. I tillegg skal også gjennomførings- og kontraktstrategier inngå i prosjektet. E39 går langs kysten fra Kristiansand til Trondheim, og er i dag ca. 1100 km lang. Også økonomiske vurderinger av ferjefri E39 skal inngå, dvs. både kostnader og gevinster, inkludert samfunnsøkonomiske analyser.

Som et ledd i prosjektet fjordkryssinger så er det ønskelig å vurdere bruk av aluminium blant annet på grunn av reduserte vedlikeholdskostnader og lav vekt i forhold til styrke. En av utfordringene er å vurdere hvordan store platefelt i aluminium sveiset sammen av ekstruderte profiler oppfører seg under en støtlast fra et skip og hvordan disse skal modelleres i en storskala analyse. Denne masteroppgaven er et ledd i dette prosjektet og er et samarbeid mellom SIMLab ved NTNU, Hydro Aluminium og Sapa.

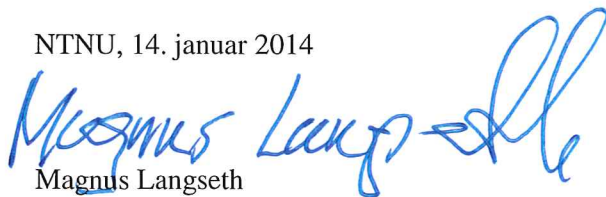
Følgende foreløpige plan er definert for denne oppgaven:

- Det skal gjennomføres et litteraturstudium knyttet til oppførsel og modellering av avstivede platefelt i aluminium og stål utsatt for en konsentrert støtlast.
- Studentene skal delta i prosjektering av en rigg i laboratoriet hvor generiske støtforsøk på sveiste platefelt skal gjennomføres. I dette ligger blant annet en vurdering av platestørrelse, oppleggsdetaljer, kontaktareal mellom platefelt og støtlegeme osv. Prosjekteringen skal baseres på numeriske analyser samt forenklete beregninger.
- Gjennomføring av et eksperimentelt program, dvs. materialtester og komponenttester.
- Etablering av en numerisk modell samt validering basert på de tester som er utført.
- Parameterstudier og retningslinjer for modellering.
- Rapportering.

Veiledere: Magnus Langseth, Odd Sture Hopperstad og David Morin

Kandidatene kan fravike den foreslåtte plan, men kun etter avtale med veilederne. Hovedoppgaven skal skrives på engelsk og utformes som en forskningsrapport og i henhold til gjeldende regler for en hovedoppgave. Oppgaven skal leveres til Institutt for konstruksjonsteknikk, NTNU innen 10. juni 2015.

NTNU, 14. januar 2014



Magnus Langseth
Professor

Acknowledgements

During this master's thesis, our supervisors have been Professor Magnus Langseth, Professor Odd Sture Hopperstad and Postdoc. David Morin at the Structural Impact Laboratory (SIMLab), Department of Structural Engineering, Norwegian University of Science and Technology (NTNU). We wish to show our gratitude for their encouraging guidance, support and input.

A special thanks to Postdoc. David Morin for his patient assistance and modeling contribution in the Finite Element Analysis (FEA) program Abaqus.


Production Manager Göran Olsson at R&D Sapa and Dr. Ole Runar Myhr at Hydro Aluminium are acknowledged for their contribution in regards of delivering the aluminium plates and for valuable input.

Laboratory experiments conducted in this master thesis were carried out at the SIMLab laboratories at the Department of Structural Engineering, NTNU. We would like to acknowledge the assistance of the laboratory staff. Especially Senior Engineer Trond Auestad and Staff Engineer Tore Wisth, who contributed in designing and building the test rig and carried out all the experiments.

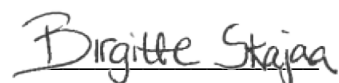
We would like to thank Sindre Sølvernes for collaboration on designing the test rig and for valuable discussion.

The SIMLab research group are acknowledged research group for an inspiring and friendly working environment.

Trondheim, June 14th, 2015



Bente Larsen Kårstad



Birgitte Skajaa

Abstract

In this master thesis, impact loading against stiffened aluminium plates of the aluminium alloy AA6082-T6 was studied. The main objective was to study the behaviour of extruded aluminium profiles welded together when exposed to impact loading from a ship, and how to model it in a large scale analysis. The study was part of a cooperation between SIMLab at NTNU, Hydro Aluminium and Sapa, as a part of the project “Coastal Highway Route E39”.

Eight plates were tested in the laboratory experiment, four by applying quasi-static loading and four by applying dynamic loading, with a cylindrical indenter in the centre of the plate, transversal and longitudinal to the stiffeners. The dynamic experiments were conducted using the kicking machine at the Department of Structural Engineering, NTNU. The experiments were attempted simulated and validated using shell elements in a nonlinear element analysis in Abaqus/Explicit. In order to perform the laboratory experiments, a rig fixing the aluminium plates in the test machine was designed.

In the experiments a good correlation was detected between the quasi-static and dynamic tests. This gave grounds to conclude that quasi-static experiments could give satisfying validation for this type of experiment on the aluminium alloy, AA6082-T6

The numerical model was implemented with two different criteria to detect fracture, the Cockcroft-Latham (CL) fracture criterion and the Bressan-Williams-Hill (BWH) instability criterion. The material implementation was simplified by using the von Mises yield criterion, where the anisotropic properties of the AA6082-T6 were neglected. The CL fracture criterion gave acceptable estimates of initiation of fracture when the mesh size is equal to the thickness of the plate. With a coarser mesh, the accuracy of this criterion decreased significantly. The BWH instability criterion gave acceptable estimates of initiation of fracture for mesh sizes varying from equal to the thickness to five times the thickness. The estimates showed to be somewhat conservative for this criterion, and a slight mesh sensitivity was detected.

In the material tests, a large degree of anisotropy was detected for aluminium alloy AA6082-T6, and a large difference between the material properties in the plate, stiffeners and the friction stir welds was found. This made the material implementation more complicated than first assumed, and the simplification with an isotropic yield criterion less accurate. An anisotropic yield criterion would more accurately describe the material behavior in the experiments, and could therefore give improved estimates.

Table of Contents

ACKNOWLEDGEMENTS	VII
ABSTRACT	IX
1 INTRODUCTION.....	1
1.1 BACKGROUND.....	1
1.2 OBJECTIVE AND SCOPE.....	2
1.3 PREVIOUS WORK.....	3
2 MATERIAL MECHANICS	7
2.1 ALUMINIUM ALLOYS.....	7
2.1.1 AA6082-T6.....	8
2.2 FRICTION STIR WELDING.....	9
2.3 TENSILE TEST	10
2.3.1 Necking.....	12
2.3.2 Flow-stress ratio and R-ratio	13
2.4 MATERIAL MODELLING.....	15
2.4.1 Yield Criterion	15
2.4.2 Plastic Flow Rule.....	17
2.4.3 Elastic-Plastic Materials with Isotropic Hardening.....	19
2.5 FAILURE MODES.....	21
2.5.1 Plugging	21
2.5.2 Tearing	21
2.5.3 Petaling	22
2.6 FRACTURE.....	22
2.6.1 Fracture Mechanisms in Metals	22
2.6.2 The Cockcroft-Latham fracture criterion	28
2.6.3 The Bressan-Williams-Hill Instability criterion.....	29
3 FINITE ELEMENT METHOD.....	35
3.1 EXPLICIT ANALYSIS.....	35
3.1.1 Explicit Direct Integration.....	36
3.1.2 Contact.....	39
3.2 PLATE THEORY	41
3.3 SHELL ELEMENTS	42
3.4 ENERGY BALANCE	43
3.4.1 Energy Absorption.....	43

Table of Contents

3.4.2	<i>Energy Balance in Quasi-Static Analyses</i>	45
4	EXPERIMENTAL SET-UP	47
4.1	IMPACT LOAD	47
4.1.1	<i>The Kicking Machine</i>	48
4.2	SUPPORT FOR QUASI-STATIC TEST	48
4.3	INTRODUCTORY MODEL.....	49
4.3.1	<i>Material</i>	50
4.4	REVISIONS OF PLATE AND RIG	51
4.4.1	<i>Revision 1</i>	52
4.4.2	<i>Revision 2</i>	55
4.4.3	<i>Revision 3</i>	56
4.4.4	<i>Revision 4</i>	58
4.4.5	<i>Revision 5</i>	58
5	PRELIMINARY ANALYSIS	61
5.1	ANALYTICAL CALCULATIONS	61
5.1.1	<i>Nominal Capacity of Bolts</i>	61
5.1.2	<i>Capacity of Support for Quasi-Static Test</i>	62
5.2	DEFORMABLE RIG MODEL.....	62
5.2.1	<i>Quasi-Static Analysis</i>	65
5.2.2	<i>Indenter Shapes</i>	66
5.2.3	<i>Mesh size on plate</i>	70
5.2.4	<i>Friction Coefficient between Support and Plate</i>	72
5.2.5	<i>Friction Coefficient between Indenter and Plate</i>	72
5.2.6	<i>Control of Forces in Rig</i>	73
5.3	REVISION OF PRELIMINARY MODEL	74
6	TENSILE TESTS	75
6.1	UNIAXIAL TENSILE TEST	75
6.1.1	<i>Test geometry</i>	76
6.2	EXPERIMENTAL RESULTS.....	78
6.2.1	<i>Flow stress ratio and R-ratio</i>	83
6.3	IDENTIFICATION OF MATERIAL PARAMETERS	84
6.3.1	<i>Numerical Modeling of Tensile Test</i>	85
6.3.2	<i>Base Material</i>	86
6.3.3	<i>Friction Stir Welds</i>	88
6.4	DISCUSSION AND REVISION OF PRELIMINARY MODEL.....	89
7	COMPONENT TESTS	93

7.1	QUASI-STATIC TEST.....	94
7.1.1	<i>Experimental Results</i>	95
7.2	ENERGY CALCULATIONS	100
7.3	DYNAMIC TEST.....	101
7.3.1	<i>Experimental Results</i>	103
7.4	DISCUSSION.....	107
7.4.1	<i>Quasi-static</i>	107
7.4.2	<i>Dynamic</i>	107
8	NUMERICAL SIMULATIONS AND DISCUSSION	109
8.1	COCKCROFT-LATHAM FRACTURE CRITERION	109
8.1.1	<i>Various Detailed Models</i>	112
8.1.2	<i>Selected Model</i>	117
8.2	THE BRESSAN-WILLIAMS-HILL INSTABILITY CRITERION	120
8.2.1	<i>Comparison between the BWH Instability Criterion and the CL Fracture Criterion</i>	125
8.2.2	<i>Marciniak-Kuczynski Analyses</i>	127
9	CONCLUSIONS AND PROPOSALS FOR FUTURE WORK	129
9.1	CONCLUSIONS.....	129
9.2	PROPOSALS FOR FUTURE WORK	130
	REFERENCES	131
	APPENDICES	135

List of Figures

FIGURE 1-1: ILLUSTRATION OF PROPOSAL BY REINERTSEN AS AND PARTNERS	1
FIGURE 2-1: FACE CENTERED CUBIC (FCC).....	8
FIGURE 2-2: SCHEMATIC DRAWING OF FRICTION STIR WELDING	9
FIGURE 2-3: A) EXEMPLARY TENSILE TEST SPECIMEN AND B) ENGINEERING STRESS STRAIN CURVE	10
FIGURE 2-4: GRAPHICAL ILLUSTRATION OF THE DIFFUSE NECKING CRITERION.	13
FIGURE 2-5: ELASTIC DOMAIN, YIELD SURFACE AND INADMISSIBLE REGION FOR A TWO-DIMENSIONAL STRESS STATE	16
FIGURE 2-6: GEOMETRICAL REPRESENTATION OF THE ASSOCIATED FLOW RULE FOR VON MISES YIELD SURFACE.	18
FIGURE 2-7: FAILURE BY PLUGGING	21
FIGURE 2-8: FAILURE BY PETALING	22
FIGURE 2-9: THREE MICROMECHANISMS OF FRACTURE IN METALS.....	23
FIGURE 2-10: VOID NUCLEATION, GROWTH, AND COALESCENCE IN DUCTILE METALS.....	24
FIGURE 2-11: FORMATION OF THE CUP AND CONE FRACTURE SURFACE IN UNIAXIAL TENSION	25
FIGURE 2-12: A) YIELDING, B) VOID NUCLEATION AND C) SHEAR FRACTURE	26
FIGURE 2-13: MECHANISM FOR DUCTILE CRACK GROWTH:	26
FIGURE 2-14: DUCTILE GROWTH OF AN EDGE CRACK, ILLUSTRATING THE TUNNELING EFFECT AND SHEAR LIPS.....	27
FIGURE 2-15: DUCTILE CRACK GROWTH IN A 45° ZIGZAG PATTERN	27
FIGURE 2-16: TYPICAL FORMING LIMIT DIAGRAM (FLD).....	30
FIGURE 2-17: LOCAL SHEAR INSTABILITY IN MATERIAL ELEMENT	31
FIGURE 3-1: THE PENALTY CONTACT METHOD.....	40
FIGURE 3-2: A) STRESSES AND DISTRIBUTED LATERAL FORCE Q ON A DIFFERENTIAL ELEMENT OF A PLATE B) MOMENT AND TRANSVERSE SHEAR FORCES ASSOCIATED WITH STRESSES IN A).....	41
FIGURE 3-3: A) LOAD BEARING BY BENDING AND B) MEMBRANE ACTION.....	42
FIGURE 3-4: ENERGY HISTORY FOR QUASI-STATIC TENSILE TEST	45
FIGURE 4-1: CYLINDRICAL INDENTER SHAPE IN ABAQUS.....	47
FIGURE 4-2: THE KICKING MACHINE	48
FIGURE 4-3: A) QUASI-STATIC SETUP AND B) SUPPORT FOR QUASI-STATIC TEST	49
FIGURE 4-4: ABAQUS MODEL – REVISION 1	50
FIGURE 4-5: EXTRUDED ALUMINIUM PROFILE	51
FIGURE 4-6: NEW EXTRUDED ALUMINIUM PROFILE.....	52

List of Figures

FIGURE 4-7: REVISION 1 - SIDE VIEW OF PLATE AND RIG [MM].....	53
FIGURE 4-8: REVISION 1- ALUMINIUM PROFILES AND PLATES WITH CUTOUTS FOR BOLTS [MM].....	53
FIGURE 4-9: REVISION 1 - ALUMINIUM PROFILES AND PLATES PLACED IN THE RIG	54
FIGURE 4-10: REVISION 1- VON MISES STRESSES IN THE PLATE.....	55
FIGURE 4-11: REVISION 2- CUTOUTS IN SUPPORT [MM]	55
FIGURE 4-12: REVISION 2 – DISPLACEMENT IN THE VERTICAL DIRECTION	56
FIGURE 4-13: REVISION 4 - SUPPORT, WITH L100x50x8.....	57
FIGURE 4-14: REVISION 4 – DEFORMATION IN THE PLATE.....	57
FIGURE 4-15: REVISION 4 – ROTATION OF STIFFENERS.....	57
FIGURE 4-16: REVISION 5 - PLATE FOR NEW ALUMINIUM PROFILE.....	58
FIGURE 4-17: REVISION 5 – RIG FOR NEW ALUMINIUM PROFILE	59
FIGURE 4-18: REVISION 6 - SIDE VIEW OF PLATE AND RIG	59
FIGURE 4-19: REVISION 6 – A) EQUIVALENT PLASTIC STRAIN IN THE IMPACT AREA AND B) ROTATION OF THE STIFFENERS	60
FIGURE 5-1: ABAQUS MODEL – ONE QUARTER OF PLATE AND RIG.....	63
FIGURE 5-2: DYNAMIC SIMULATION OF RIGID-RIG MODEL VERSUS DEFORMABLE-RIG MODEL	64
FIGURE 5-3: DYNAMIC VERSUS QUASI-STATIC ANALYSIS FOR THE DEFORMABLE-RIG MODEL	65
FIGURE 5-4: ENERGY HISTORY IN QUASI-STATIC ANALYSIS FOR THE DEFORMABLE-RIG MODEL.....	66
FIGURE 5-5: INDENTER 1, QUARTER OF THE CYLINDRICAL INDENTER.....	66
FIGURE 5-6: INDENTER 2, QUARTER OF THE CYLINDRICAL INDENTER WITH ROUNDED EDGES.....	67
FIGURE 5-7: A) EQUIVALENT PLASTIC STRAIN WITH INDENTER 1 AND B) INDENTER 2.	68
FIGURE 5-8: INDENTER 2 IN TRANSVERSAL AND LONGITUDINAL DIRECTION	69
FIGURE 5-9: INDENTER 3 - 100MM	69
FIGURE 5-10: EQUIVALENT PLASTIC STRAIN INDENTER 3.....	70
FIGURE 5-11: CYLINDRICAL INDENTER WITH ROUNDED EDGES (INDENTER 2) AND SPHERICAL INDENTER (INDENTER 3).....	70
FIGURE 5-12: EFFECT OF MESH SIZE ON PLATE ON A) FORCE-DISPLACEMENT AND ON B) DAMAGE FACTOR.....	71
FIGURE 5-13: EFFECT OF FRICTION COEFFICIENT BETWEEN TEFLON AND PLATE	72
FIGURE 5-14: EFFECT OF FRICTION COEFFICIENT BETWEEN INDENTER AND PLATE.....	73
FIGURE 6-1: A) UNIAXIAL TENSILE TEST SETUP IN INSTRON HYDRAULIC MACHINE AND B) SPECIMEN WITH EXTENSOMETER.....	76
FIGURE 6-2: TENSILE TEST SPECIMENS.....	77
FIGURE 6-3: TEST SPECIMENS ON THE PLATE.	78

FIGURE 6-4: ENGINEERING STRESS-STRAIN CURVES FOR SPECIMENS IN ALL DIRECTIONS, FOR WEB AND FOR FSW.	79
FIGURE 6-5: ENGINEERING AND TRUE STRESS-STRAIN CURVES FOR REPRESENTATIVE SAMPLES.	80
FIGURE 6-6: PRINCIPAL STRAIN FIELD MAPS IN ALL DIRECTIONS OF BASE MATERIAL.	81
FIGURE 6-7: FRACTURE IN REPRESENTATIVE SAMPLES	82
FIGURE 6-8: REPRESENTATIVE RESULTS FOR A) THE SPECIFIC PLASTIC WORK AND B) THE FLOW STRESS RATIO.	83
FIGURE 6-9: R-RATIO FOR MATERIAL SAMPLES IN ALL DIRECTION	84
FIGURE 6-10: ABAQUS/IMPLICIT MODEL OF UT110 TENSILE SPECIMEN	85
FIGURE 6-11: ABAQUS/IMPLICIT SHELL MODEL OF UT200 TENSILE SPECIMEN.	86
FIGURE 6-12: THE POWER LAW VERSUS THE ENGINEERING STRESS STRAIN CURVE FOR	87
FIGURE 6-13: DIRECT CALIBRATION VERSUS OPTIMIZED VOCE RULE	88
FIGURE 6-14: DIRECT CALIBRATED POWER LAW COMPARED TO THE OPTIMIZED POWER LAW	89
FIGURE 6-15: STIFFENER MATERIAL COMPARED WITH BASE MATERIAL.	90
FIGURE 6-16: EQUIVALENT PLASTIC STRAIN (PEEQ) IN THE NUMERICAL SIMULATION OF THE UT200 SPECIMEN OVER THE WELD. ...	91
FIGURE 7-1: PLATES DELIVERED BY SAPA	93
FIGURE 7-2: CYLINDRICAL INDENTER WITH ROUNDED EDGES.	93
FIGURE 7-3: SET-UP FOR QUASI-STATIC TEST	94
FIGURE 7-4: SETUP OF THE PLATE IN THE RIG.	95
FIGURE 7-5: EXPERIMENTAL RESULTS FOR THE QUASI-STATIC TEST OF TRANSVERSALLY PLACED INDENTER.	95
FIGURE 7-6: FRACTURE IN A) QSTE1 AND B) QSTE2.	96
FIGURE 7-7 A)-D): FRACTURE IN PLATE WITH TRANSVERSALLY PLACED INDENTER.	97
FIGURE 7-8: EXPERIMENTAL RESULTS FOR QUASI-STATIC TEST OF LONGITUDINAL PLACED INDENTER	98
FIGURE 7-9: A) FRACTURE IN QSLE1 FROM BEHIND AND B) TOP VIEW OF FRACTURE ON QSLE2.	99
FIGURE 7-10: FRACTURE IN QSLE2.	99
FIGURE 7-11: FRACTURE IN A) QSLE2 AND B) QSLE1.	100
FIGURE 7-12: A) THE KICKING MACHINE AND THE RECEIVING WALL AND B) THE RECEIVING WALL.	101
FIGURE 7-13: STEP-BY-STEP ILLUSTRATION OF MOUNTING THE PLATE AND RIG IN THE KICKING MACHINE.	102
FIGURE 7-14: INDENTER MOUNTED IN THE TRANSVERSAL DIRECTION ON THE TROLLEY.	103
FIGURE 7-15: EXPERIMENTAL RESULTS FOR DTE1 AND DTE2.	104
FIGURE 7-16: A) MAXIMUM DISPLACEMENT IN DTE1, B) AND DEFORMED PLATE AFTER IMPACT. NECKING IN THE STIFFENERS AND CRACK IN THE PLATE OF C) DTE1 AND D) DTE2	104

List of Figures

FIGURE 7-17: EXPERIMENTAL RESULTS FOR DTE1 AND DTE2.....	105
FIGURE 7-18: FRACTURE IN DLE1.	105
FIGURE 7-19: FRACTURES IN PLATES FROM DYNAMIC TESTS.	106
FIGURE 7-20: QUASI-STATIC EXPERIMENT – TRANSVERSAL VERSUS LONGITUDINALLY PLACED INDENTER.....	107
FIGURE 7-21: QUASI-STATIC VERSUS DYNAMIC EXPERIMENTAL RESULTS	108
FIGURE 8-1: THE COCKCROFT-LATHAM CRITERION WITH POWER LAW AND VOCE RULE FOR DYNAMIC SIMULATIONS WITH TRANSVERSE INDENTER.....	110
FIGURE 8-2: THE COCKCROFT-LATHAM CRITERION WITH POWER LAW AND VOCE RULE FOR DYNAMIC SIMULATIONS WITH THE LONGITUDINAL INDENTER.	111
FIGURE 8-3: QUASI-STATIC EXPERIMENT VERSUS QUASI-STATIC ANALYSIS	112
FIGURE 8-4: QUASI-STATIC EXPERIMENT WITH TRANSVERSAL INDENTER (QSTE1) VERSUS QUASI-STATIC ANALYSIS WITH BASE MATERIAL ON THE WHOLE PLATE (QSTA VOCE RULE BM) AND WITH INCLUDED MATERIAL IN THE STIFFENERS (QSTA VOCE RULE SM)	113
FIGURE 8-5: DYNAMIC EXPERIMENT WITH TRANSVERSAL INDENTER (DTE1) VERSUS DYNAMIC ANALYSIS WITH ONLY BASE MATERIAL (DTA VOCE RULE BM) AND WITH STIFFENER MATERIAL INCLUDED (DTA VOCE RULE SM).....	113
FIGURE 8-6: DYNAMIC ANALYSIS, FORCE-DISPLACEMENT PLOT OF PLATE WITHOUT FSW COMPARED TO PLATE WITH FSW.....	114
FIGURE 8-7: QUASI-STATIC ANALYSIS, FORCE-DISPLACEMENT PLOT OF PLATE WITHOUT FSW COMPARED TO PLATE WITH FSW	115
FIGURE 8-8: NUMERICAL MODEL WITH FSW AND "LIPS".....	116
FIGURE 8-9: FORCE-DISPLACEMENT PLOT OF PLATE WITHOUT "LIP" COMPARED TO PLATE WITH "LIP"	116
FIGURE 8-10: FORCE-DISPLACEMENT PLOT OF PLATE WITH ASSUMED THICKNESS AND AVERAGE OF MEASURED THICKNESS	117
FIGURE 8-11: NECKING OF STIFFENERS IN A) EXPERIMENT AND B) NUMERICAL SIMULATION	118
FIGURE 8-12: VELOCITY-TIME PLOTS FOR ANALYSIS VERSUS EXPERIMENTS.....	118
FIGURE 8-13: EXPERIMENT VERSUS ANALYSIS ENERGY-DISPLACEMENT PLOT FOR A) TRANSVERSE INDENTER AND B) LONGITUDINAL INDENTER.....	119
FIGURE 8-14: DYNAMIC ANALYSES VERSUS QUASI-STATIC ANALYSES	120
FIGURE 8-15: BWH FLDS	121
FIGURE 8-16: DYNAMIC ANALYSIS WITH BWH INSTABILITY CRITERION COMPARED TO EXPERIMENT FOR THE A) TRANSVERSE AND B) LONGITUDINAL INDENTER	122
FIGURE 8-17: DYNAMIC ANALYSIS WITH BWH INSTABILITY CRITERION WITH FSW INCLUDED COMPARED TO EXPERIMENTS.....	123
FIGURE 8-18: MAXIMUM PRINCIPAL STRESS VERSUS σ_1 FROM THE BWH CRITERION	123
FIGURE 8-19: QUASI-STATIC ANALYSIS FOR THE BWH CRITERION WITHOUT THE FSW	124

FIGURE 8-20: ABSORBED ENERGY VERSUS DISPLACEMENT PLOTS FOR DYNAMIC ANALYSES	125
FIGURE 8-21: DYNAMIC EXPERIMENT VERSUS CL DYNAMIC ANALYSIS WITH DIFFERENT MESH SIZES.....	126
FIGURE 8-22: FLD FOR BWH WITH ALL MESH SIZES AND MK WITH VON MISES AND HERSHEY YIELD CRITERION COMPARED	127
FIGURE 8-23: DYNAMIC ANALYSIS FOR THE MK FLD WITHOUT THE FSW	128

List of Tables

TABLE 2-1: FLOW STRESS RATIO FOR AA6082-T6 AT STRAIN RATE 10^{-3} s ⁻¹	14
TABLE 2-2: REPRESENTATIVE TEST RESULTS: THE R-RATIOS AND FLOW STRESS RATIOS	15
TABLE 4-1: CHEMICAL COMPOSITION OF AA6082-T6.....	50
TABLE 4-2: HARDENING PARAMETERS.....	51
TABLE 5-1 KEY VALUES FROM THE MATERIAL CARD	63
TABLE 5-2: MATERIAL CHARACTERISTICS OF S355 STEEL	63
TABLE 5-3: COMPUTATIONAL TIME FOR DIFFERENT MESH SIZES.....	71
TABLE 6-1: CHEMICAL COMPOSITION ACCORDING TO EN-573-3:1994.....	75
TABLE 6-2: MATERIAL PROPERTIES ACCORDING TO EN 755-2:2008.....	75
TABLE 6-3: FLOW STRESS RATIO FOR REPRESENTATIVE TEST.....	83
TABLE 6-4: R-RATIO FOR MATERIAL SAMPLES	84
TABLE 6-5: MATERIAL PARAMETERS FOR REPRESENTATIVE SAMPLES	85
TABLE 6-6: POWER LAW PARAMETERS FOR SAMPLE 00-2 AND WEB00-2.....	87
TABLE 6-7: VOCE RULE PARAMETERS FOR SAMPLE 00-2 AND WEB00-2.....	87
TABLE 6-8: COCKCROFT-LATHAM PARAMETER FOR POWER LAW AND VOCE RULE	88
TABLE 6-9: POWER LAW PARAMETERS FOR SAMPLE FSW00-2	89
TABLE 7-1: EXPERIMENTAL RESULTS – EXTERNAL WORK AND VELOCITY IN KICKING MACHINE	100
TABLE 8-1: COMPUTATIONAL TIME FOR REPRESENTATIVE ANALYSES	126

1 Introduction

This master thesis is a cooperation between SIMLab at NTNU, Hydro Aluminium and Sapa, as part of the project “Coastal Highway Route E39” on the western coast of Norway. The objective is to investigate the influence an impact load from a ship will have on extruded and welded aluminium profiles, and how to model this in a large-scale analysis.

1.1 Background

The Coastal Highway Route E39 runs along the western coast of Norway from Kristiansand to Trondheim, and is 1100 km long. Since the summer of 2010, the Norwegian Public Roads Administration (NPRA) has been, and is currently, working on the project “Coastal Highway Route E39” (Statens Vegvesen, 2010). The project is divided into four parts: technical development of fjord crossings, analysis of social impacts, potential solutions for renewable energy, and implementation strategies and contract forms (Statens Vegvesen, 2014). The NPRA was asked by the Ministry of Transport and Communications to study the potential a ferry-free E39 would have on industry and trade, and thus employment and settlement on the west coast of Norway. The project will also consider technological solutions for fjord crossings, and how structures may be utilized to produce energy from the sun, waves, currents and wind. In addition, economical analyzes and contract strategies should be included (Statens Vegvesen, 2015).



Figure 1-1: Illustration of proposal by Reinertsen AS and partners showing a fjord crossing by pontoon bridges and a submerged tunnel (Reinertsen AS, 2015)

It is desirable to consider the use of aluminium in these projects, mainly due to reduced maintenance costs and low weight compared to strength. Aluminium also has high resistance against corrosion, which is an advantage when the material is used for a fjord crossing. The challenge is to consider how welded, extruded profiles of aluminium behave when exposed to impact loading from a ship and how these can be modeled in a large-scale analysis.

1.2 Objective and Scope

The objective of this master thesis is to investigate the behaviour of extruded aluminium profiles welded together when exposed to impact loading from a ship. The objective will be met by a combination of numerical simulation in Abaqus/Explicit and laboratory tests with the kicking machine at SIMLab, NTNU.

The main tasks of the project are:

- Literature study related to the behaviour and modeling of stiffened plates in aluminium and steel exposed to concentrated impact loads.
- Design of a rig to use for testing of the plates in the kicking machine in the SIMLab laboratory. It includes an assessment of plate size, detailing of supports, contact area between plate and impact load. The planning will be based on numerical simulations and simplified calculations.
- Conducting material tests of the aluminium alloy AA6082-T6 to study the material properties in three different directions in relation to the extrusion direction, and in the stiffeners and over the weld.
- Conducting quasi-static and dynamic component tests. The dynamic experiments will be conducted using the kicking machine at the Department of Structural Engineering, NTNU.
- Establishment of a numerical model in Abaqus/Explicit and conducting parameter studies to decide shape of indenter and to study the effect of changing different parameter like friction and mesh size.
- Implementing material card and criteria to detect fracture in the numerical model for validation of the component tests.

This master thesis is limited by the following:

- The material which is studied is the aluminium alloy, AA6082 with temper T6
- Aluminium profiles with thickness *4mm* and T-stiffeners with thickness *3mm*.
- The profiles are welded together using the friction stir weld method.
- The plate will be subjected to concentrated quasi-static and dynamic loading.
- The Cockcroft-Latham fracture criterion and the Bressan-Williams-Hill instability criterion will be used to detect fracture in the numerical model.

1.3 Previous Work

A literature study has been conducted on stiffened plates subjected to concentrated impact loading. The study includes both steel and aluminium plates, different types of indenters and different velocities of the indenters.

Langseth and Larsen (1994) did a plugging capacity test of dropped objects on aluminium alloy plates, using AA5083-H112 and AA6082-T6. Their test showed that AA5083-H112 absorbs 40-70% more energy than AA6082-T6 at plugging, mainly due to an increased yield stress for alloy AA6082-T6, implying a stiffer deformation process for the latter. It also showed that the weight saving of using aluminium instead of steel ranged between 31-38% for AA5083-H112 and 12-15% for AA6082-T6, but required that the thickness of the aluminium plates were twice the thickness of the steel plate (Langseth and Larsen, 1994).

Hilde Giærver Hildrum (2002) wrote her Dr. Eng. thesis on stiffened aluminium plates subjected to impact loading. There, she studied the behaviour of plates subjected to large mass projectiles with low velocity. The study was performed on plates of aluminium alloy AA6082 temper T6 extrusions, welded together with MIG-welds. From the impact test, she found that the estimated incipient fracture velocity was significantly less for a hemispherical ended indenter than a flat ended indenter, and that impact on the weld between the stiffeners gave the lowest incipient fracture velocity (Hildrum, 2002). This coincides well with the results from Wang et al's (2000) study on the behaviour of a double hull subjected to punching load with different spherical indenters, as they found that the structure shows much higher resistance when the cones are blunt than when they are sharp (Wang et al., 2000).

Hildrum (2002) tried to find a relationship between dynamic and quasi-static capacities before fracture by performing additional static punch tests. In the velocity range she studied, she found that static tests of the blunt ended projectile may be used to give a conservative estimate of the incipient fracture impact energy in the dynamic test. This is in contrast to the hemisphere ended projectile, where it may be non-conservative. (Hildrum, 2002)

In Villaviencio and Guedes Soares (2013) paper on impact response of rectangular and square stiffened steel plates supported on two opposite sides, the results showed that the elastic force increased largely with the impact velocity. For impacts not on the stiffener, after the elastic force, the forces increased gradually until maximum. This is due to the development of membrane forces in the plate at the point of impact when the plate deforms plastically (Villaviencio and Guedes Soares, 2013). Similarly, Wang (2002) found that the contribution from plastic bending on a plate under a lateral load is large for small deformations but negligibly small for large deformations. With adequate large deformations, the membrane force dominates the behaviour of the plate (Wang, 2002). Villaviencio and Guedes Soares (2013) also found that when the impact force is applied right above the stiffener, the elastic force is followed by a ‘decaying oscillation’ where the forces remain constant over a short time. After this, the forces increase gradually, with some oscillations, until the maximum load is reached (Villaviencio and Guedes Soares, 2013).

In Langseth et al.’s (1999) paper ‘Impact Loading on Plates: Validation of Numerical Simulations by Testing’, it was noticed that the response for both aluminium and steel is dominated by membrane stresses, which implies that the interface force curves are strongly influenced by the input stress-strain curve. Langseth et al. (1999) states that tests show that 90-95% of the impact energy is absorbed as global strain energy in the plate and only a small fraction locally in the plugging process. This makes the use of shell elements to model the behaviour of thin aluminium plates subjected to impact loading very effective (Langseth et al., 1999).

In Liu et al.’s (2015) paper on simplified analytical methods to evaluate tanker side panels during minor collision incidents, the energy absorbing mechanisms of small-scale stiffened plates were examined. They found that the critical deflection and energy increase with the indenter width due to a decreased stress concentration with a wider contact area, and thus a delayed crack initiation. They also did tests on unstiffened plates which showed that the critical deflection at failure depends on the response of the plate itself, not the stiffeners (Liu et al., 2015). Villaviencio and Guedes Soares (2012) found from tests with drop-weight impact of stiffened steel plates with a spherical indenter that the plastic response is highly sensitive to the extent of restraint at the supports (Villaviencio and Guedes Soares, 2012).

In Alsos et al.'s (2008) paper on the BWH instability criterion, they compared forming limit diagrams (FLDs) determined by the BWH criterion in a set of benchmark cases with FLDs they found in literature, and found very good correlation between the BWH criterion and the benchmark FLDs. This is an important observation since one of the arguments for the BWH criteria is that it can be applied analytically to develop FLDS for both proportional and non-proportional straining (Alsos et al., 2008).

Alsos et al. (2008) also did a numerical comparison of the BWH instability criterion with experiments by implementing it into the finite element code LS-DYNA. This was done to see if the BWH criterion could effectively estimate the onset of instability at a reasonable computational cost. In the criterion, element failure is based on middle through thickness integration points, so there is no effect from bending, and pure plate bending will not cause local necking. Alsos et al. (2008) states that this way of introducing failure may be too conservative, but when comparing the numerical results to the experimental results, they found that failure is initiated right before the actual fracture happens. This is a good approximation, since the BWH criterion predicts local instability, not final fracture. It was also noticed that the BWH criterion predicts failure without being overly sensitive to the mesh size, since it avoids analysis in the post necking zone (Alsos et al., 2008).

2 Material Mechanics

In this chapter, theory regarding the material is described. The main topics include description of aluminium and friction stir welding, a material model where the mechanics of the material is described, relevant failure modes, fracture mechanisms and criterions to predict failure.

2.1 Aluminium Alloys

Aluminium is a relatively soft material compared to other common structural materials such as steel. Aluminium has a density of approximately 2.7 kg/dm^3 , while steel has a density of approximately 7.8 kg/dm^3 . This low density gives aluminium alloys the characteristic of having low weight while still maintaining high strength and extends the use of the material vastly. Aluminium can be made in all shapes also available for steel, and the low weight makes handling easier (Bohne and Aalberg, 2011).

The production of aluminium is costly and energy consuming, which is one of the main reasons why it took time before aluminium became an industrial metal (Bohne and Aalberg, 2011). About one third (35%) of the cost of producing one tonne of aluminium is consumed by electric power, which means that a small gain in energy consumption quickly will affect the total cost (Dialog on Aluminium, 2012).

One of the favorable qualities of aluminium is that it can be 100 % recycled, repeatedly, with no loss in the inherent properties. This is possible because the atomic structure is not altered during melting. Further, the energy required in the recycling process of aluminium is only 5% of the energy required in the primary production (European Aluminium Association, 2009).

There are a few different methods of processing aluminium. Casting is used when producing larger series of components, occasionally with complex shapes. Extrusion of aluminium utilizes the material properties in an optimal way, and has contributed to an increased use of the material. The method of extruding allows for many different shapes of the aluminium profiles (Bohne and Aalberg, 2011). For welding aluminium, there are two common methods, Metal Inert Gas (MIG) welding and Friction Stir Welding (FSW). In this master thesis, FSW has been used and will be described.

Aluminium is a polycrystalline material, where the individual grains have a crystallographic orientation, which differ from the neighboring grains orientations (Wang, 2006). When aluminium crystallizes, it forms a face-centered cubic lattice, see Figure 2-1. This crystal structure is stable from $4K$ to the melting point (Hatch, 1984).

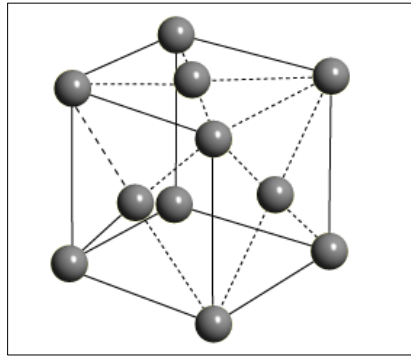


Figure 2-1: Face Centered Cubic (FCC) Structure (Hofmann, 1999)

The material properties of aluminium alloys will never be completely uniform in all directions and some degree of anisotropy will always be present. The nature of this anisotropy depends upon the composition of the alloy and the process history (Gottstein et al., 2010).

2.1.1 AA6082-T6

Alloying elements are added to aluminium to obtain better metal characteristics. In this master thesis, the alloy AA6082-T6 is used. 6xxx alloys are typically used for autobody sheets, structural members and for architectural purposes, with magnesium and silicone as principal alloying elements (Davis, 1993). Al-Mg-Si alloys have many positive characteristics, like moderate high strength, good corrosion resistance and relatively low quench sensitivity (Hatch, 1984). Magnesium gives increased strength and hardness, better weldability, and good resistance against corrosion. Silicone, in combination with magnesium, gives curable alloys with good resistance against corrosion (Bohne and Aalberg, 2011). These qualities, in addition to good formability and suitability for extrusion have led to an extensive use of this alloy in offshore structures (Wang, 2006).

The thermal history of the aluminium profile has an important impact on the strength of the material. The material AA6082-T6, is a so-called heat-treatable alloy, which means that the material can be given a thermal treatment to adjust the mechanical properties. Temper T6 is the peak hardness condition that results from solution heat treatment, quenching and artificial aging. In solution heat treatment, the material is kept at a temperature where the one-phase condition is reached in the equilibrium diagram. Here, precipitates like Mg_2Si are dissolved and the homogeneous solid state is reached. The temperature should avoid the eutectic temperature, and be below the melting point. For 6xxx alloys the solution treatment temperature is between $500^{\circ}C$ - $550^{\circ}C$ (Graeve and Hirsh, 2010). The main purpose with this treatment is to maximize the amount of the hardening solutes like magnesium and silicon in the solid solution

of the aluminum matrix (Hatch, 1984). After this treatment, the alloy is rapidly cooled down by press quenching, to preserve the solid solution. Directly after exiting the extrusion press it is exposed to forced air or water spray. The final process is artificial ageing, where the material is reheated, resulting in more efficient formations of hardening precipitates (Graeve and Hirsh, 2010). The artificial aging results in an increased yield strength but decreased ductility (Key to Metals, 2010). For more information about the T6 temper, see chapter 5 in *Aluminum: properties and Physical Metallurgy* (Hatch, 1984).

2.2 Friction Stir Welding

Friction stir welding is a solid-state technique where sheet and plate materials are welded together below the melting point. It was invented and patented in 1991 at TWI in Cambridge, UK (Kallee et al., 2001). The weld is made by a rotating tool that moves along the joint, producing heat and plastic deformation of the material. The softened material is moved around the tool, and this way the plates are stirred together. The plastic deformation generates a fine microstructure with equiaxed, recrystallized grains that have good mechanical properties. A schematic drawing of friction stir welding is shown in Figure 2-2 (Mishra and Ma, 2005).

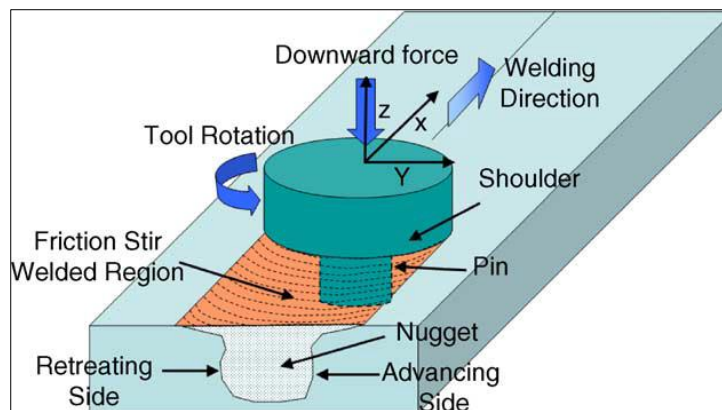


Figure 2-2: Schematic drawing of Friction Stir Welding (Mishra and Ma, 2005)

FSW obviates problems like porosity and hot cracking. The heat input is relatively low and therefore the loss in mechanical properties is less compared to other welding techniques. It is considered to be an energy efficient and environmental friendly joining technique since there are no emissions during the welding. In addition, distortion, shrinkage and residual stresses are very small especially in thin plates (Çam and Mistikoglu, 2014).

The material around the weld can be divided in three different zones based on the microstructure. The centre of the weld is called the nugget zone (NZ), which is exposed to high strains and recrystallization. Next is the thermo-mechanically affected zone (TMAZ) that extends to the tools shoulder. On the outside the material is only affected by the heat from the process, hence the name, heat-affected zone (HAZ) (Moreira et al., 2009).

2.3 Tensile Test

In a uniaxial tensile test, a specimen is pulled in tension until fracture . The main purpose of a tensile test is to find the tensile strength of the material and the evolution of the stress-strain relationship. To avoid dynamic effects, the rate of the loading has to be low enough to be considered quasi-static. Tensile testing should always be performed following ASTM standard (American Association of Testing Materials) or a similar standard.

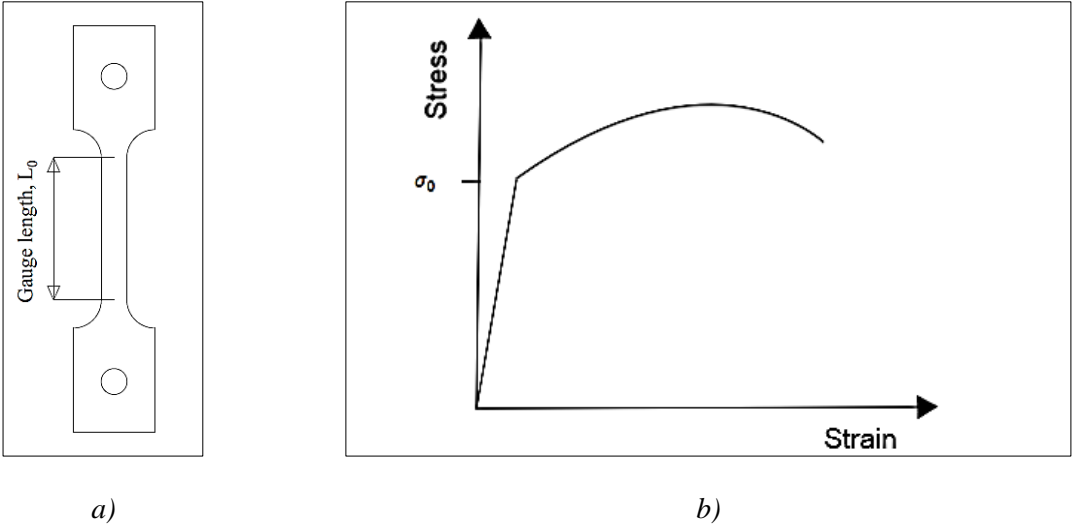


Figure 2-3: a) Exemplary tensile test specimen and b) engineering stress strain curve

The output from the uniaxial tensile test is a force-displacement curve. From this curve, the engineering stress and strain are found, see Figure 2-3 b). In this section it is assumed that the deformation is uniform, and hence the following equations are valid. Engineering stress is calculated by equation 2-1 using the applied force F , and the initial cross section A_0 (Hopperstad and Børvik, 2013)

$$\sigma_e = \frac{F}{A_0} \tag{2-1}$$

Engineering strain is calculated using the time-dependent measured displacement $u_L(t)$ and the initial gauge length l_0 (Figure 2-3 a). The engineering strain (2-2) and the increment of the engineering strain (2-3) are given, respectively:

$$\varepsilon_e(t) = \frac{u_L(t)}{L_0} \quad 2-2$$

$$d\varepsilon_e(t) = \frac{du_L(t)}{L_0} \quad 2-3$$

With large strains, it becomes important to account for the geometrical changes to describe the true behaviour of the material. Applying, $L = L_0 + u_L$ and consequently $dL = du_L$, the strain increment with respect to the current length and the logarithmic true strain is obtained as equation 2-4 and equation 2-5, respectively (Hopperstad and Børvik, 2013):

$$d\varepsilon_l(t) = \frac{du_L(t)}{L} \quad 2-4$$

$$\varepsilon_l = \int_0^{u_L} \frac{du_L}{L} = \int_{L_0}^L \frac{dL}{L} = \ln\left(\frac{L}{L_0}\right) = \ln(1 + \varepsilon_e) \quad 2-5$$

The true stress is found by employing the current cross section of the specimen, A (Equation 2-6). For aluminium, the elastic strain remains small and the plastic deformation is volume preserving, further described in section 2.4.1. When assuming constant volume, $A_0L_0 = AL$. This leads to a relationship between the engineering stress and strain and the true stress (Equation 2-7) (Hopperstad and Børvik, 2013):

$$\sigma_t = \frac{F}{A} \quad 2-6$$

$$\sigma_t = \sigma_e(1 + \varepsilon_e) \quad 2-7$$

In finite element codes like Abaqus, the stress-strain data are given in terms of true stress and true strain by default (Hopperstad and Børvik, 2013). Since the true stress is a direct measure of the traction being carried out per unit area by any internal surface in the specimen, it is possibly the only stress of practical interest as an output from an finite element code like Abaqus, from an engineering viewpoint (Dassault Systems, 2014).

The total strain can be separated into two terms, as seen in equation 2-8, the plastic part, ε^p , is permanent and the elastic part is defined by, $\varepsilon^e = \frac{\sigma}{E}$.

$$\varepsilon = \frac{\sigma}{E} + \varepsilon^p \quad 2-8$$

From this relation, the true plastic strain curve can be calculated using equation 2-9. Where the plastic strain, ε^p , varies with the logarithmic true strain ε_l (equation 2-5) (Hopperstad and Børvik, 2013):

$$\varepsilon^p = \varepsilon_l - \frac{\sigma}{E} \quad 2-9$$

2.3.1 Necking

When the force reaches its maximum value, the deformation localizes and the specimen experiences diffuse necking. The cross-section where necking occurs decreases promptly with the increasing strain. After necking occurs, the straining of the specimen is no longer uniform and thus the equations in the previous section is no longer valid. From equations 2-5 and 2-7, the engineering stress can be expressed as:

$$\sigma_e = \sigma_t \exp(-\varepsilon_l) \quad 2-10$$

The maximum value of the engineering stress is reached as $d\sigma_e = 0$, and by implementing the product and chain rule, the incremental change of the engineering stress becomes:

$$d\sigma_e = d\sigma_t \exp(-\varepsilon_l) - \sigma_t \exp(-\varepsilon_l) d\varepsilon_l = (d\sigma_t - \sigma_t d\varepsilon_l) \exp(-\varepsilon_l) \quad 2-11$$

From this, the diffuse necking criterion is defined in equation 2-12 and shown graphically in Figure 2-4. The figures show that diffuse necking occurs when the slope of the true stress - true strain curve equals the true stress.

$$\frac{d\sigma_t}{d\varepsilon_l} = \sigma_t \quad 2-12$$

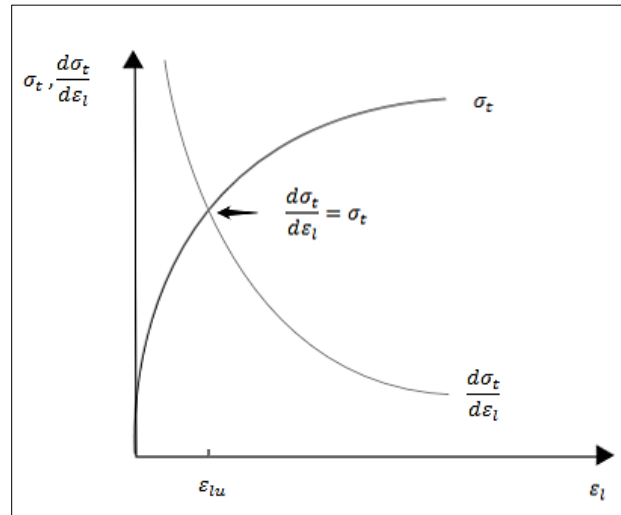


Figure 2-4: Graphical illustration of the diffuse necking criterion. ε_{lu} is the logarithmic strain at necking. Figure inspired by (Hopperstad and Børvik, 2013)

In plates, where the width is much larger than the thickness, localized necking may occur. A sharp localized neck is normally developed on the surface as failure in stretching is initiated. Localized necking can be described by considering a wide, thin sheet specimen loaded in uniaxial tension in the length direction. In diffuse necking, there is contraction strains in both the width and the thickness direction, while with a wide specimen the width direction cannot localize rapidly. Since only the thickness direction is localized, the neck develops gradually and considerable extension is possible after the onset of necking (Hosford and Caddell, 1993).

2.3.2 Flow-stress ratio and R-ratio

Chen et al. (2009) studied the behaviour of extruded AA6xxx aluminium alloys in T6 temper at a wide range of strain rates. They found that AA6xxx alloys do not exhibit significant rate sensitivity in the stress-strain behaviour. In order to study the anisotropy of the extruded aluminium alloys, tensile tests were performed in three different directions with respect to the extrusion direction. The angle α indicates the direction of the specimens relative to the extrusion direction, i.e. $\alpha=0^\circ$ when the extrusion direction is parallel to the longitudinal direction of the specimen (Chen et al., 2009).

The plastic anisotropy is characterized with a flow-stress ratio r_α , which is defined as the ratio between the flow stress σ_f^α in a tensile test with direction α and the flow stress σ_f^0 of a reference test in the extrusion direction, for the same amount of plastic work (equation 2-13). By definition the flow-stress ratio for the reference test in the extrusion direction is equal to unity (Chen et al., 2009).

$$r_\alpha = \left. \frac{\sigma_f^\alpha}{\sigma_f^0} \right|_{W_p} \quad 2-13$$

The specific plastic work W_p in a tensile test in the α direction for a given plastic strain ε_α^p is given as

$$W_p = \int_0^{\varepsilon_\alpha^p} \sigma_f^\alpha d\varepsilon_\alpha^p \quad 2-14$$

Chen et al. (2009) calculated the flow-stress ratio as a function of plastic work up to the point of necking for each alloy in the 45° and 90° directions. The flow-stress ratio converges to a nearly constant value. The values for AA6082-T6 they found are given in Table 2-1, and are based on a test at strain rate 10^{-3} s^{-1} (Chen et al., 2009).

Table 2-1: Flow stress ratio for AA6082-T6 at strain rate 10^{-3} s^{-1} (Chen et al., 2009)

Alloy	r_0	r_{45}	r_{90}
AA6082-T6	1.0	0.919	0.975

Anisotropy may also be described by the R -ratio, which in direction α relative to the extrusion direction is given by (Chen et al., 2009):

$$R_\alpha = \frac{\dot{\varepsilon}_w^p}{\dot{\varepsilon}_t^p} \quad 2-15$$

where $\dot{\varepsilon}_w^p$ and $\dot{\varepsilon}_t^p$ are the plastic strain rates in the width and the thickness direction of the tensile specimen. These rates are often assumed to have the same ratio for increasing strains, therefore the R -ratio can be defined as (Lademo et al., 1999):

$$R_\alpha = \frac{\varepsilon_w^p}{\varepsilon_t^p} \quad 2-16$$

If the strains in the width and the thickness direction are equal for all directions, the material is said to exhibit isotropic flow properties, i.e $R_\alpha = 1$ in all directions, α (Lademo et al., 1999). Wang (2006) found the R -ratio and the flow-stress ratio in different directions for an AW-6082 T6 aluminium sheet, shown in Table 2-2. It can be seen that in relation to the R -ratio this

extrusion exhibited significant anisotropy in the plastic flow, with a value of only 0.37 in the extrusion direction. The flow-stress ratio shows a much lower tendency of anisotropy (Wang, 2006). It can be observed from Table 2-1 and Table 2-2 that in relation to the flow stress ratio, plastic anisotropy of AA6082-T6 is nearly absent.

Table 2-2: Representative test results: the R-ratios and flow stress ratios (Wang, 2006)

R_0	R_{45}	R_{90}	r_0	r_{45}	r_{90}
0.37	1.19	0.87	1.00	0.93	1.02

2.4 Material Modelling

The following chapter will provide a basis for the material mechanics of plasticity and large strains in the area before necking. The theory is mostly based on the Lecture notes from Materials Mechanics by Hopperstad and Børvik (2013).

Aluminium and other structural materials will behave linearly elastic for adequately small deformations. This means that the deformation is reversible, and that there is a linear relationship between stresses and strains (Hooke's Law, equation 2-1). For a certain stress level, σ_0 , the behaviour becomes nonlinear and plastic yielding occurs. After this point the deformations are plastic and therefore irreversible. The transition from elastic to elastic-plastic domain can be gradual or abrupt. Most aluminium alloys exhibit a gradual transition (Hopperstad and Børvik, 2013).

2.4.1 Yield Criterion

The yielding limit may be described mathematically by a yield criterion:

$$f(\boldsymbol{\sigma}) = 0 \quad 2-17$$

where f is the yield function which is a continuous function of the stress tensor $\boldsymbol{\sigma}$. The yield criterion, $f(\boldsymbol{\sigma}) = 0$, defines a surface in the stress space called the yield surface. As seen in Figure 2-5, the elastic domain is enclosed by the yield surface, described by $f(\boldsymbol{\sigma}) < 0$. It is assumed that the yield function cannot have values outside the yield surface which is describe by the inadmissible region, $f(\boldsymbol{\sigma}) > 0$ (Hopperstad and Børvik, 2013).

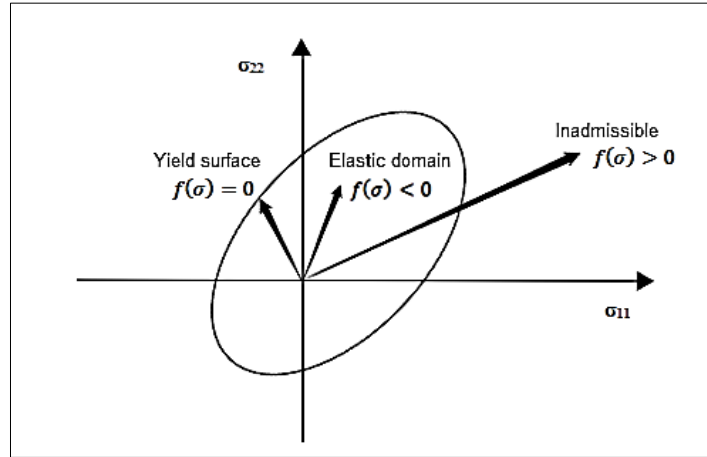


Figure 2-5: Elastic domain, Yield surface and Inadmissible region for a two-dimensional stress state
Figure inspired by (Hopperstad and Børvik, 2013)

The yield function is often written in the form:

$$f(\boldsymbol{\sigma}) = \varphi(\boldsymbol{\sigma}) - \sigma_Y \quad 2-18$$

The equivalent stress, $\sigma_{eq} = \varphi(\boldsymbol{\sigma})$, measures the magnitude of the stress state the material is subjected to. The equivalent stress is here assumed to be a positive homogeneous function. The yield stress, σ_Y , is determined by mechanical tests (Hopperstad and Børvik, 2013).

Metals and alloys are said to be pressure insensitive, because plastic deformation mainly appears due to a shear driven deformation mode called plastic slip (Hopperstad and Børvik, 2013). In Khan and Huang’s book ‘Continuum theory of plasticity’ (1995), they describe Schmid’s Law. Schmid’s Law is based on the statement that yielding begins in a slip system when the shear stress on this slip plane, in the slip direction, reaches a critical value. The yielding is independent of the tensile axial stress and other normal stresses on the lattice plane. This means that it is the shear stress component in the slip direction on the slip plane which initiates plastic deformation, not the applied axial tensile stress (Khan and Huang, 1995). Since pressure insensitivity can be assumed, the yield criterion can be expressed only depending on the deviatoric stress state on the form (Hopperstad and Børvik, 2013):

$$f(\boldsymbol{\sigma}') = 0 \quad 2-19$$

The stress deviator, $\boldsymbol{\sigma}'$, is defined by $\sigma'_{ij} = \sigma_{ij} - \sigma_H \delta_{ij}$, where σ_H is the hydrostatic stress, i.e. the mean stress, and $P = -\sigma_H$ represents the pressure of the stress state. The hydrostatic stress is given in equation 2-20, where σ_{kk} denotes σ_{11} , σ_{22} and σ_{33} and I_σ is the principal invariant

(Hopperstad and Børvik, 2013). More information about the Kronecker delta, δ_{ij} , can be found at 'MathWorld – A Wolfram Web Resource' (Weisstein, 2015).

$$\sigma_H = \frac{1}{3} \sigma_{kk} = \frac{1}{3} I_\sigma \quad 2-20$$

Khan and Huang's (1995) book describes the incompressibility effect of hydrostatic pressure. Plastic incompressibility means that the volume of a material does not change permanently when exposed to a large pressure. See equation 2-21 where incompressibility is described mathematically in terms of true strain. It is also stated that the stress-strain curve is unaffected by hydrostatic pressure in small strain ranges and that the ductility of a material increases under hydrostatic pressure (Khan and Huang, 1995).

$$\varepsilon_1 + \varepsilon_2 + \varepsilon_3 = 0 \quad 2-21$$

The plastic yielding of aluminium alloys is not isotropic, but a simplification with an isotropic yield criterion could be valid when the degree of anisotropy is low. Isotropic yielding implies that the yield function is independent of the direction of loading within the material. The yield function is most conveniently written in terms of the principal invariants of the stress deviator for isotropic and pressure independent materials, $f(J_2, J_3) = 0$, where $J_2 = \frac{1}{2} \sigma'_{ij} \sigma'_{ij}$, and $J_3 = \det(\sigma'_{ij})$ (Hopperstad and Børvik, 2013).

2.4.2 Plastic Flow Rule

The plastic flow rule is generally defined by (Hopperstad and Børvik, 2013):

$$\dot{\varepsilon}_{ij}^p = \dot{\lambda} \frac{\partial g}{\partial \sigma_{ij}} \quad 2-22$$

Where $g = g(\sigma) \geq 0$ is the plastic potential function which is assumed to be a positive homogenous function of order one and $\dot{\lambda}$ is a non-negative scalar called the plastic parameter. This ensures that the plastic strain rate tensor $\dot{\varepsilon}^p$ is defined in a way that gives non-negative dissipation, where the plastic dissipation is given by $D_p = \sigma_{ij} \dot{\varepsilon}_{ij}^p \geq 0$. When the plastic potential is defined by the yield yield function, the associated flow rule is formed (Hopperstad and Børvik, 2013).

$$\dot{\varepsilon}_{ij}^p = \dot{\lambda} \frac{\partial f}{\partial \sigma_{ij}} \quad 2-23$$

2.4.2.1 Von Mises yield criterion

The von Mises criterion is an isotropic and pressure insensitive yield criterion. It is used for isotropic materials in Abaqus CAE (Dassault Systems, 2014). The assumption is that yielding occurs when the second principal invariants of the stress deviator J_2 reach a critical value, k^2 , $J_2 = k^2$. Plasticity theories based on the von Mises criterion are often called J_2 flow theories. The von Mises yield function can be expressed by the stress deviator (Hopperstad and Børvik, 2013).

$$f(\boldsymbol{\sigma}) = \sqrt{\frac{3}{2} \sigma'_{ij} \sigma'_{ij}} - \sigma_Y = 0 \quad 2-24$$

The von Mises yield criterion expressed in terms of principal stress:

$$f(\sigma_1, \sigma_2, \sigma_3) = \sqrt{\frac{1}{2} ((\sigma_1 - \sigma_2)^2 + (\sigma_2 - \sigma_3)^2 + (\sigma_3 - \sigma_1)^2)} - \sigma_Y = 0 \quad 2-25$$

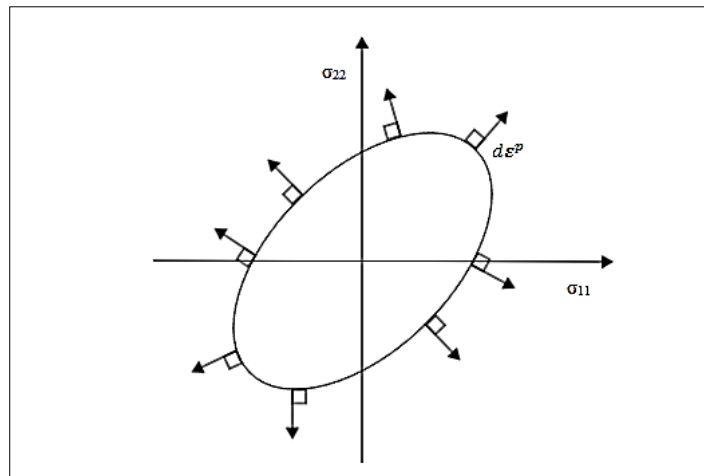


Figure 2-6: Geometrical representation of the associated flow rule for von Mises yield surface. Figure inspired by (Hopperstad and Børvik, 2013)

The associated flow rule implies that the incremental plastic strain vector, $d\boldsymbol{\varepsilon}^p$, is normal to the yield locus, and can therefore be referred to as the *normality rule*. This is shown for the von Mises yielded surface in Figure 2-6. The normality rule entails that the shape of the yield surface determines the stress state at which yielding initiates and the direction of the plastic flow (Hopperstad and Børvik, 2013).

The components of the plastic strain rate tensor $\dot{\boldsymbol{\varepsilon}}^p$ are then described by the following equation which states that the plastic strain rate tensor is deviatoric and proportional to the stress deviator.

$$\dot{\varepsilon}_{ij}^p = \frac{3\dot{\lambda}}{2\sigma_{eq}} \sigma'_{ij} \quad 2-26$$

where $\sigma_{eq} = \sqrt{3J_2}$. The plastic volumetric strain rate is zero, $\dot{\varepsilon}_{ii}^p = 0$, which means that according to von Mises yield criterion and the associated flow rule, plastic deformations will not lead to any change in the volume, i.e. plastic incompressibility. The plastic parameter $\dot{\lambda}$ may be interpreted as an equivalent plastic strain rate, which leads to the definition of equivalent plastic strain (Hopperstad and Børvik, 2013):

$$p = \int_0^t \dot{p} dt \equiv \int_0^t \dot{\lambda} dt \quad 2-27$$

For the associated flow rule, the equivalent plastic strain rate equals the plastic parameter, which leads to the convenient expression for equivalent plastic strain rate (Hopperstad and Børvik, 2013):

$$\dot{p} = \sqrt{\frac{2}{3} \dot{\varepsilon}_{ij}^p \dot{\varepsilon}_{ij}^p} \quad 2-28$$

2.4.3 Elastic-Plastic Materials with Isotropic Hardening

When a material is deformed plastically, work-hardening occurs, which implies that the strength increases up to the point of necking. This plastic deformation of the material leads to movement of dislocations, and additional dislocations are generated. As the number of dislocations increases, the more they will interact, resulting in a strengthening of the material, but a decrease in the ductility (NDT Resource Center, 2014).

Elastic-plastic materials with isotropic hardening, account for work-hardening by letting the yield stress be dependent on the plastic straining. The yield function with isotropic hardening is generally described with the equation 2-29 and 2-30 (Hopperstad and Børvik, 2013):

$$f(\sigma, R) = \varphi(\sigma) - \sigma_Y(R) \leq 0 \quad 2-29$$

$$\sigma_Y(R) = \sigma_0 + R \quad 2-30$$

Where $\varphi(\sigma)$ is the equivalent stress, $\sigma_Y(R)$ is the flow stress and R is the isotropic hardening variable. Under plastic deformation the hardening variable R increases which leads to an increase in flow stress, and results in an expansion of the elastic domain (Hopperstad and Børvik, 2013).

The general isotropic hardening rule (Equation 2-31) describes the rate at which the material is work-hardened. The hardening modulus, h_R , is assumed to depend on the state of the material (Hopperstad and Børvik, 2013).

$$\dot{R} = h_R \dot{\lambda} \quad 2-31$$

The Voce rule and the power law are two nonlinear isotropic work-hardening rules that describe the evolution of the hardening variable R by the equivalent plastic strain. When the plastic strain increases, the power law curve increases indefinitely while the Voce curve saturates. The power law is defined by Equation 2-32 (Hopperstad and Børvik, 2013):

$$R(p) = Kp^n \quad 2-32$$

where K and n are hardening parameters, which are determined from material tests. The Voce rule is given by:

$$R(p) = Q_R(1 - e^{-C_R p}) \quad 2-33$$

where C_R and Q_R are hardening parameters and the latter represents the saturating of R . The Voce rule can also be describe by a sum of equations like in equation 2-34:

$$R(p) = \sum Q_{Ri}(1 - e^{-C_{Ri} p}) \quad 2-34$$

When assuming associated flow rule, given $\dot{p} = \dot{\lambda}$, the hardening modulus for the power law (2-35) and the Voce rule (2-36) are defined as, respectively (Hopperstad and Børvik, 2013):

$$h_R = Knp^{n-1} \quad 2-35$$

$$h_R = C_R(Q_R - R) \quad 2-36$$

2.5 Failure Modes

The failure mode of a plate material is dependent upon the velocity of the indenter, angle of the indenter and the material properties of the plate. Failure of thin or intermediate plates often involves fracture due to the interactions of mechanisms like material properties, geometric characteristics and impact velocity (Backman and Goldsmith, 1978). Failure modes which are relevant for this master thesis are described in the following subsections.

2.5.1 Plugging

Failure due to plugging most commonly occurs in thin to intermediate, hard plates impacted by blunt projectiles. Plugging develops as a result of a slug with nearly the same shape as the moving projectile, as shown in Figure 2-7. The projectile pushes the slug and generates large shears around the slug. The large shear forces generates heat, which decreases the material strength around the slug and results in an instability. This instability is called an adiabatic shearing process (Backman and Goldsmith, 1978).

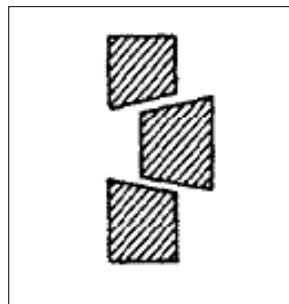


Figure 2-7: Failure by plugging (Backman and Goldsmith, 1978)

2.5.2 Tearing

Failure due to tearing can occur as a plate is impacted by a rigid wedge. When the wedge hits the plate, the plate buckles and bends out of plane. When the ultimate strength of the plate is reached, the load declines without separation of material. As the wedge pushes further, there is separation of material and the load increases (Wang, 2002).

2.5.3 Petaling

Failure due to petaling most commonly occurs in thin plates impacted by blunt projectiles at relatively low impact velocity. As the projectile pushes the plate material forward, large bending moments create deformation of the plate. This produces high radial and circumferential tensile stresses after passage of the initial wave near the lip of the penetrator. As petaling occurs, it is followed by plastic flows or permanent bending, and when the tensile strength of the material is exceeded, a star shaped crack develops (Backman and Goldsmith, 1978).

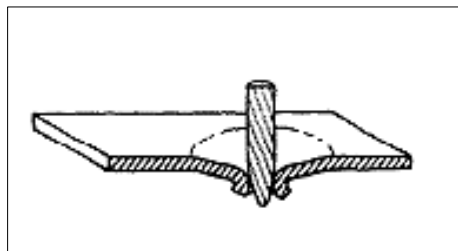


Figure 2-8: Failure by petaling (Backman and Goldsmith, 1978)

2.6 Fracture

In this chapter, microscopic fracture mechanisms and criterions to predict fracture are looked into. The discussed criterions are the Cockcroft-Latham fracture criterion and the BWH instability criterion.

In the constitutive model presented in the previous sections, it is assumed that that yielding is independent of hydrostatic stress. Teirlinck et al. (1988) states that the plastic behaviour is weakly dependent on hydrostatic pressure, but for practical use, the pressure insensitive von Mises yield criterion is sufficient. With fracture, the situation is different because the volume of the piece will increase when voids nucleate and grow (Teirlinck et al., 1988).

2.6.1 Fracture Mechanisms in Metals

When developing materials with optimal toughness, it is essential to understand the microstructural events that lead to fracture. In some cases, it is favourable to approach fracture with solid mechanics, modelling the behaviour of the materials as a continuous mass instead of discrete particles. In other cases, it might be necessary to also look into the microscopic fracture mechanisms. The theory on fracture in this section is mostly based on the *Third edition Fracture Mechanics* book by T.L Anderson (Anderson, 2005).

There are three common micromechanisms of fracture in metals and alloys, they are illustrated in Figure 2-9. In a ductile material, the fracture (Figure 2-9a) is usually a result of nucleation, growth and coalescence of microscopic voids that initiate at inclusions and second-phase particles. In other words, the voids grow together forming a macroscopic flaw, which leads to fracture. Cleavage fracture, often called brittle fracture (Figure 2-9b) describes separation along specific crystallographic planes, resulting in a transgranular and relatively smooth fracture path. Intergranular fracture develops when the preferred fracture path consist with the grain boundaries (Figure 2-9c) (Anderson, 2005).

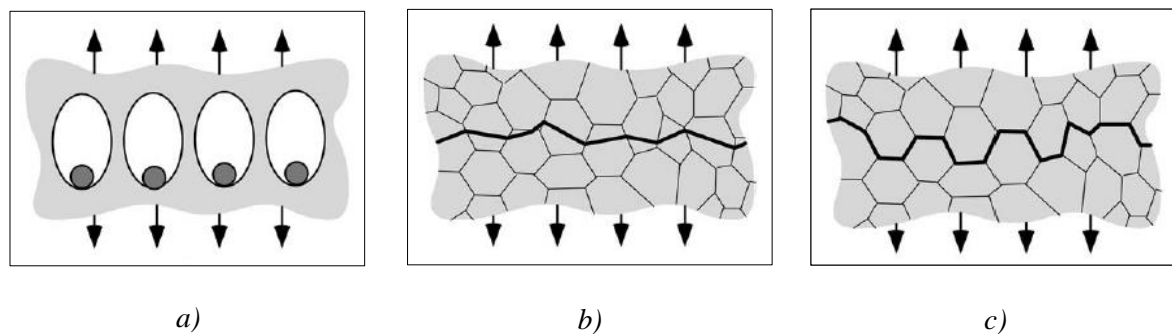


Figure 2-9: Three micromechanisms of fracture in metals (Anderson, 2005) a) Ductile fracture, b) Cleavage fracture and c) Intergranular fracture

2.6.1.1 Ductile material

The material AA6082-T6 is assumed to experience a ductile fracture and thus it is described in more detail in this section. As described in section 2.3.1, a material under uniaxial tension will eventually reach an instability point. This occurs as the strain hardening cannot keep up with the loss in the cross-sectional area, and a necking region arises. The forming of the necking area depends upon the purity of the material. In a tensile specimen of a material with high purity, the reduction in area could be nearly 100% with severely large local plastic strains. Materials with impurities will fail at lower strains, and therefore lower reduction in area (Anderson, 2005). In reality Aluminium is not 100% pure, it will always contain residual impurities, like iron, silicone and copper (Meijers et al., 2010)

The whole process where nucleations initiate at inclusions and form microscopic voids that coalesce and create a macroscopic flow which in the end leads to fracture, is systematically illustrated in Figure 2-10. The interfacial bonds between the particle and the matrix is broken when sufficient stress is applied, this will create a void around a second-phase particle or an inclusion, see Figure 2-10 b). When further plastic strain and hydrostatic stress is applied, the voids grow and eventually coalesce. Figure 2-10 c) shows how each void grows independently

which can be assumed if the initial volume fraction of the voids is low ($<10\%$). Figure 2-10 d) and e) illustrates how plastic strain is localized along a sheet of voids, and how local necking instabilities form between voids. The stress state decides the orientation of the fracture path (Anderson, 2005).

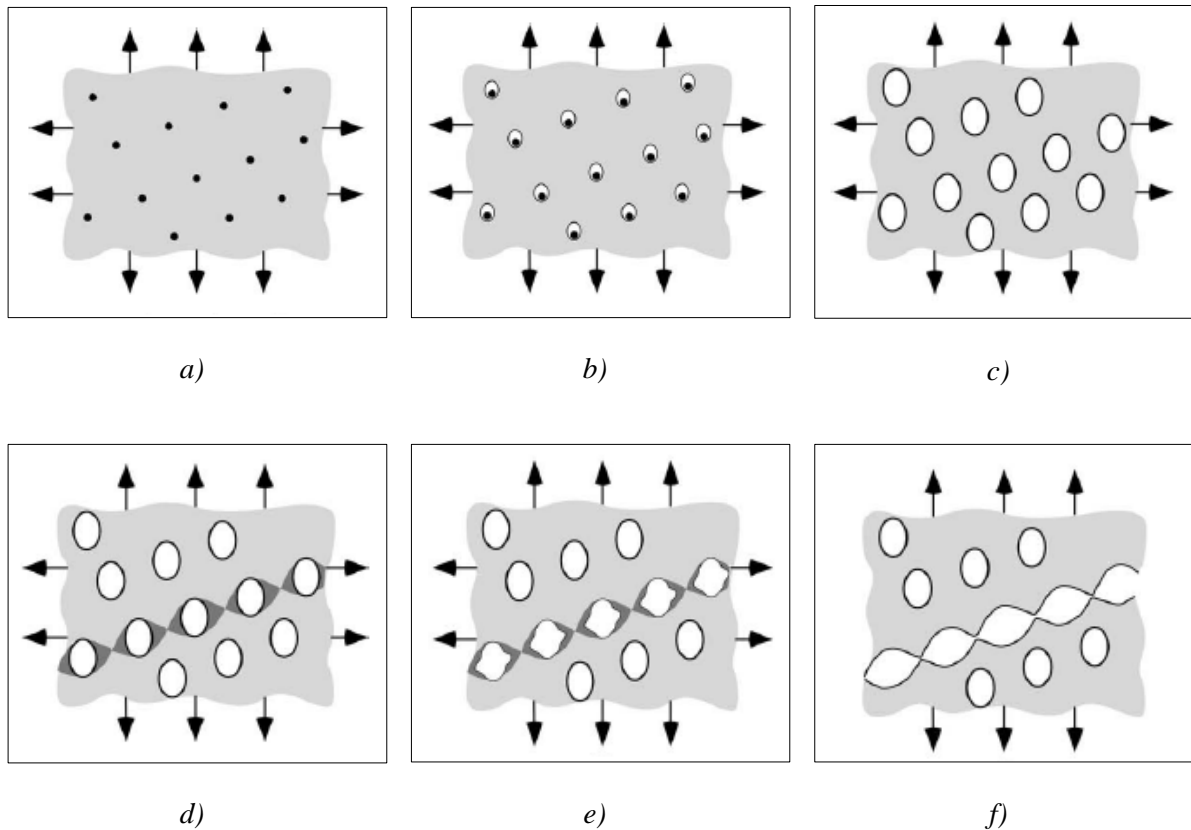


Figure 2-10: Void nucleation, growth, and coalescence in ductile metals. a) Inclusions in a ductile matrix, b) void nucleation, c) void growth, d) strain localization between voids, e) necking between voids and f) void coalescence and fracture (Anderson, 2005)

A precipitation hardened aluminium alloy may have a bimodal distribution of particles, containing relatively large intermetallic particles and a fine dispersion of submicron second-phase precipitates. This Bimodal particle distribution can lead to shear fracture surfaces (Anderson, 2005).

The “cup and cone” fracture surface formation which is often observed in a uniaxial tensile test of circular specimens, is shown in Figure 2-11. Figure 2-11a) shows how a triaxial stress state develops in the necking area, in the center of the specimen, which promotes void nucleation and growth in the larger particles. When applying more strain, the voids grow together and form a penny-shaped flaw. The hydrostatic stress is lower in the outer ring of the specimen, which explains why there are fewer voids there compared to the center. The penny-shaped flaw gives rise to deformation bands at 45° from the tensile direction (Figure 2-11b). This concentration

of strains leads to nucleation of voids in the finer particles (Figure 2-11c). These particles are closely spaced, which leads to instability soon after the voids are formed and total fracture, with the recognizable cup and cone surfaces (Figure 2-11d). The outer region of the fracture is typically smooth while the central region has a fibrous appearance at low magnifications. The outer surface is often referred to as a “shear surface” because of its direction, 45° , from the tensile axis and since there are little evidence of microvoids coalescence at low magnifications (Anderson, 2005). In shear fracture, or *void-sheeting*, voids nucleate in slip bands and with further shear, the voids grow and fracture occurs (Figure 2-12). Shear fracture is less pressure dependent because void which extend in shear do not need to increase in volume (Teirlinck et al., 1988).

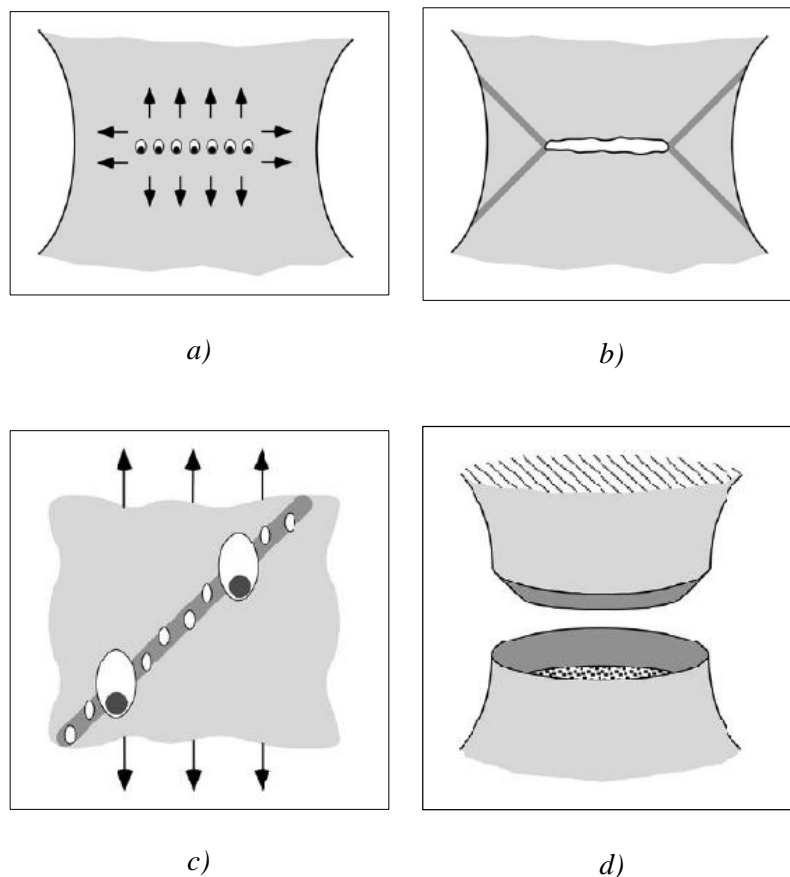


Figure 2-11: Formation of the cup and cone fracture surface in uniaxial tension : a) void growth in a triaxial stress state b) crack and deformation band formation c) nucleation at smaller particles along the deformation bands d) cup and cone fracture (Anderson, 2005)

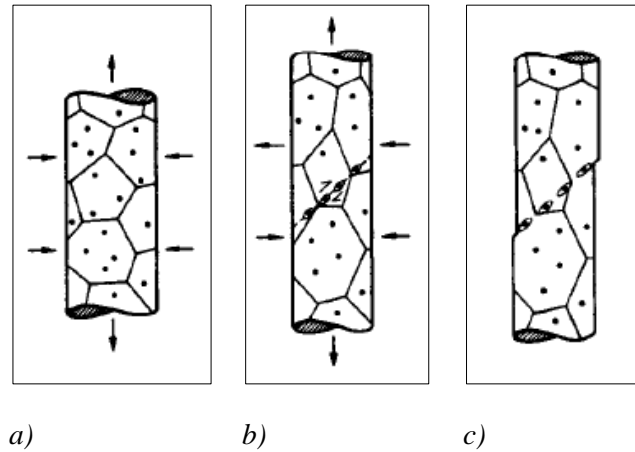


Figure 2-12: a) Yielding, b) void nucleation and c) shear fracture (Teirlinck et al., 1988)

The mechanisms for ductile crack growth on the tip of a pre-existing crack is illustrated in Figure 2-13. When the surface with a crack is loaded, strains and stresses are localized at the crack tip, and when they are sufficient, voids start to nucleate (Figure 2-13a). As the crack becomes more blunt, the voids grow and eventually they coalesce with the crack (Figure 2-13 b, and c). This process continues through the material and the crack grows. A plate with an edge crack that grows by microvoids coalescence may exhibit a *tunnelling effect*, which means that as a result of higher stress triaxiality, the crack grows faster in the center of the plate. Figure 2-14 illustrates how the *tunnelling effect* will produce deformation bands that nucleate voids in small particles. This results in *shear lips*, which means that near a free surface, the crack growth will develop at a 45° angle from the maximum principal stress. Shear lips resemble the cup and cone fracture formation illustrated in Figure 2-11 (Anderson, 2005).

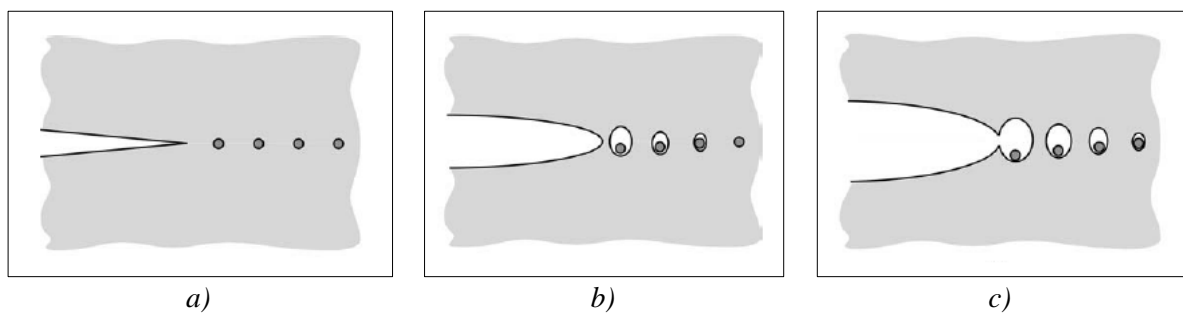


Figure 2-13: Mechanism for ductile crack growth: a) initial state b) void growth at the crack tip c) coalescence of voids with the crack tip (Anderson, 2005)

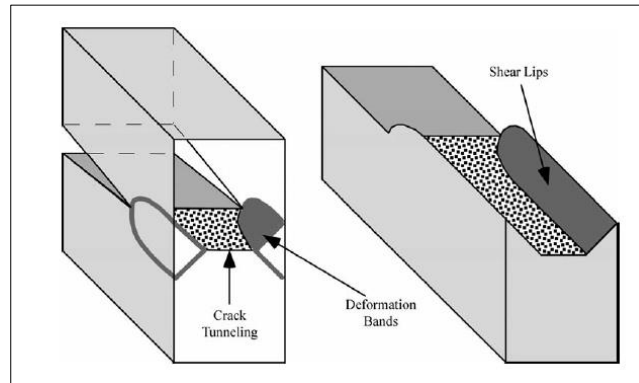


Figure 2-14: Ductile growth of an edge crack, illustrating the tunneling effect and shear lips (Anderson, 2005)

The high-triaxiality crack growth appears to be flat on a global scale but when viewed with a higher magnification, a more complex structure is revealed. Figure 2-15 a) shows the plane of maximum plastic strain, which on a local level is the preferred path for void coalescence. Since global constraints require that the crack generate in its original plane, one outcome is that the crack grows in a $\pm 45^\circ$ zigzag pattern (Figure 2-15 b). Figure 2-15 c) displays this behaviour in a metallographic cross-section of a growing crack (Anderson, 2005).

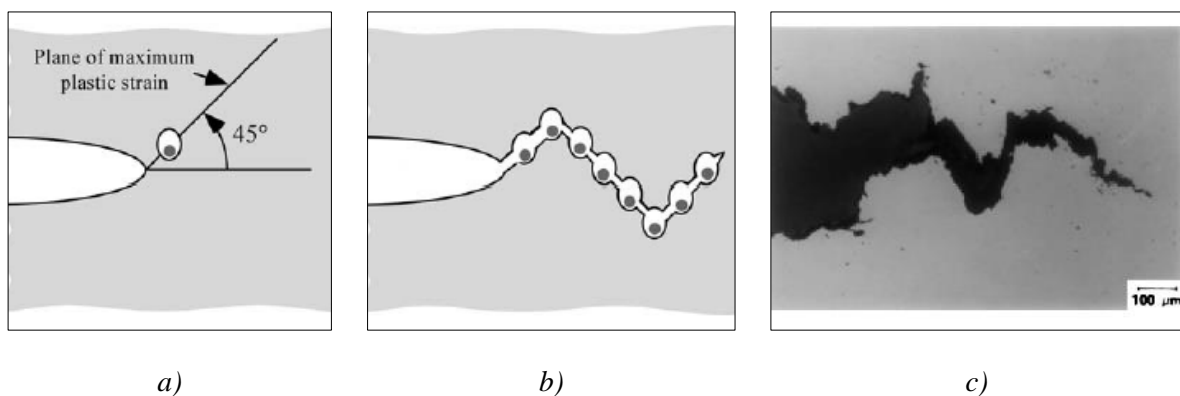


Figure 2-15: Ductile crack growth in a 45° zigzag pattern a) plane of maximum plastic strain, b) Zigzag crack propagation pattern, and c) Optical micrograph (unetched) of ductile crack growth in an A 710 high-strength low-alloy steel. Photograph courtesy of J.P. Guda (Anderson, 2005)

2.6.2 The Cockcroft-Latham fracture criterion

Cockcroft and Latham studied the fact that for a given material, fracture occurs for different strains, dependent on the work processes. They assumed that the criterion on fracture should be based on a combination of stresses and strains, and therefore, they looked at the total plastic work done per unit volume at the fracture point. For a cylindrical test specimen, the stresses at necking can be divided in two parts. The equivalent stress, which is equal the current yield stress, and a hydrostatic tension, which varies from zero at the rim to a peak value at the centreline. The peak stress σ^* is, unlike the current yield stress, influenced by the shape of the necked region. From this, they found that it would be reasonable to take the magnitude of the highest normal stress into account; this is the peak stress, σ^* , for the tensile test. Then, the criterion based on plastic work would be dependent on the necking shape. Cockcroft and Latham proposed the following criteria: That fracture occurs in a ductile material when the expression in equation 2-37 reaches a constant value C for a given temperature and strain rate (Cockcroft and Latham, 1968).

$$\int_0^{\varepsilon_f} \bar{\sigma} \left(\frac{\sigma^*}{\bar{\sigma}} \right) d\bar{\varepsilon} \quad 2-37$$

Where ε_f is the fracture strain, $\bar{\sigma}$ is the equivalent stress, and $\bar{\varepsilon}$ is the equivalent strain. The relation $\left(\frac{\sigma^*}{\bar{\sigma}} \right)$ is a non-dimensional representation of the effect of the highest tensile stress σ^* . For calculation purposes, the expression is reduced to (Cockcroft and Latham, 1968).

$$\int_0^{\varepsilon_f} \sigma^* d\varepsilon = C \quad 2-38$$

The criterion is regarded as a description of the observed behaviour of metals; it is not considered a fundamental law. The criterion suggest that a ductile fracture is dependent on shear stresses and tensile stresses (Cockcroft and Latham, 1968).

Takuda et al. (1999) rewrote equation 2-38, and obtained the following integral (Takuda et al., 1999):

$$I = \frac{1}{C} \int_0^{\varepsilon_f} \sigma^* d\varepsilon \quad 2-39$$

Where the fracture condition is satisfied when and where the integral I amounts to unity (Takuda et al., 1999).

In the SIMLab metal model that will be used in the preliminary studies, the Cockcroft and Latham criterion was implemented. There, the criterion is defined as:

$$\dot{D} = \frac{\langle \hat{\sigma}_1 \rangle}{S_0} \dot{p} \quad 2-40$$

Where $\hat{\sigma}_1$ is the maximum eigenvalue of the Cauchy stress tensor, S_0 is a positive constant which is identified from experimental data, and \dot{p} is the equivalent plastic strain rate. When fracture occurs, D (the damage factor), equals the critical value, D_c , and the following relation (equation 2-41) is given, where p_f is the equivalent plastic strain at fracture (Structural Impact Laboratory, 2014).

$$\int_0^{p_f} \langle \hat{\sigma}_1 \rangle dp = D_c S_0 \quad 2-41$$

The Cockcroft-Latham parameter W_c is introduced as

$$W_c = D_c S_0 \quad 2-42$$

2.6.3 The Bressan-Williams-Hill Instability criterion

A forming limit diagram (FLD) provides the maximum in-plane principal strains that a sheet metal can sustain without localized necking when subjected to proportional strain paths defined by a constant strain ratio. The strain ratio, β , is given by the incremental changes in strain in the minor principal axis divided by the incremental changes in strain in the major principal axis. (Hopperstad, 2013)

$$\beta = \frac{\Delta \varepsilon_2}{\Delta \varepsilon_1} \quad 2-43$$

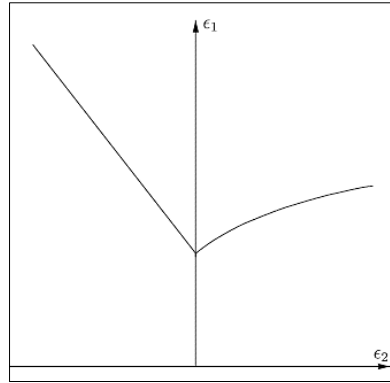


Figure 2-16: Typical forming limit diagram (FLD) (Alsos et al., 2008)

The forming limit diagram is, as mentioned, strain-based and depends on a proportional strain path. He et al. (2014) stated that the material deformation in sheet metal forming process is almost always nonlinear, and in some loading conditions, the loading path can deviate significantly from linearly. To consider the nonlinearity, it is possible to use a stress-based FLD which can be converted from the strain-based FLD, and is not dependent on deformation paths (He et al., 2014).

The Bressan-Williams-Hill (BWH) criterion provides a simplified way to determine the onset of local necking. It describes an analytical forming limit curve in the stress space, which is more or less unaffected by the strain paths, and can thus be expressed as strain-path independent (Alsos et al., 2009). The following derivation of the Bressan-Williams-Hill (BWH) criterion is retrieved from Alsos et al. (2008). They adopted a stress based forming limit approach, and evaluated a combined Bressan-Williams and Hill instability criterion.

To be able to describe both the positive and the negative quadrant of the FLD, the Hill and the Bressan-Williams criterion were combined to the Bressan-Williams-Hill (BWH) criterion. This criterion is shown in equation 2-44 (Alsos et al., 2008).

$$\sigma_1 = \begin{cases} \frac{2K}{\sqrt{3}} \frac{1 + \frac{1}{2}\beta}{\sqrt{\beta^2 + \beta + 1}} \left(\frac{2}{\sqrt{3}} \frac{\hat{\epsilon}_1}{1 + \beta} \sqrt{\beta^2 + \beta + 1} \right)^n & \text{if } \beta \leq 0 \\ \frac{2}{\sqrt{3}} K \frac{\left(\frac{2}{\sqrt{3}} \hat{\epsilon}_1 \right)^n}{\sqrt{1 - \left(\frac{\beta}{2 + \beta} \right)^2}} & \text{otherwise} \end{cases} \quad 2-44$$

Both the Hill's local necking criterion and the Bressan-Williams shear instability criterion will be described in the following paragraphs.

Bressan and Williams (BW) found that a shear based instability criterion could estimate the point of local necking in the positive quadrant of the FLD. This was justified by experiments that showed that in sheet metal, the failure planes lie close to the direction of the maximum shear stress. And thus it is reasonable to assume that the instability in the sheet metals occurs before necking is visible. The expressions found by BW follow three assumptions (Alsos et al., 2008):

1. The shear instability is initiated in the direction through the thickness at which the material element experience no change of length (direction x_t , Figure 2-17), indicating a critical through-thickness shear direction.
2. The instability is triggered by a local shear stress which exceeds a critical value. This means that the initiation of local necking is described as a material property.
3. Elastic strains are neglected, which is reasonable since the plastic strains are large compared to elastic strains at local necking.

From these assumptions and Figure 2-17, the BW criterion was found.

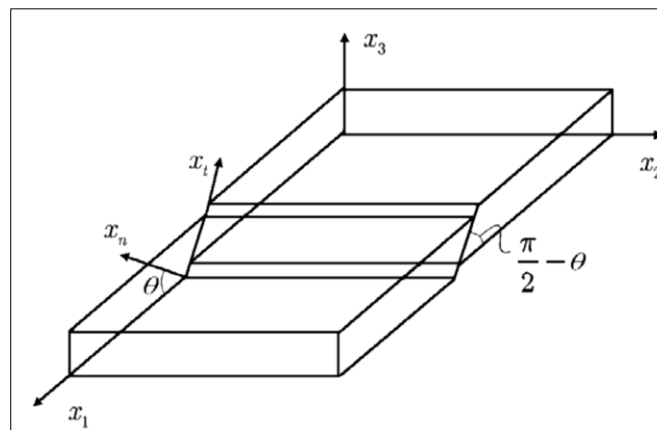


Figure 2-17: Local shear instability in material element (Alsos et al., 2008)

As the shear instability occurs, the inclined plane through the element thickness forms an angle to the shell plane, but does not elongate, so $\dot{\epsilon}_t$ remains zero.

$$\dot{\epsilon}_t = \frac{\dot{\epsilon}_1 + \dot{\epsilon}_3}{2} + \frac{\dot{\epsilon}_1 - \dot{\epsilon}_3}{2} \cos 2 \left(\theta + \frac{\pi}{2} \right) = 0 \quad 2-45$$

If plastic incompressibility (section 2.3), $\dot{\epsilon}_3 = -\dot{\epsilon}_1(1 + \beta)$, is assumed, it is found that:

$$\cos 2\theta = -\frac{\beta}{2 + \beta} \quad 2-46$$

To find the relation between the inclined plane and the stress, the stress state is obtained from the rules of stress transformation.

$$\tau_{cr} = \frac{\sigma_1}{2} \sin 2\theta \quad 2-47$$

The Bressan-Williams criterion is found by combining the two equations (2-46 and 2-47):

$$\sigma_1 = \frac{2\tau_{cr}}{\sqrt{1 - \left(\frac{\beta}{2 + \beta}\right)^2}} \quad 2-48$$

A more detailed derivation of the Bressan-Williams shear based instability criterion is shown in appendix A.1.

The BW criterion is valid for the positive regime of the FLD, and is unstable in the negative quadrant. Therefore, the Hill's local necking criterion was combined with the BW criterion to cover the whole regime. Hill assumed that the strain increments along a local neck, which forms an angle φ with the major principal axis, will be zero. This angle can be expressed by $\varphi = \tan^{-1}\left(\frac{1}{\sqrt{-\beta}}\right)$, which is only valid for negative values of β . The fractions within the material reach a maximum value at the point of local necking, since when a neck is formed, the effect of strain hardening and the diminution in thickness balance each other exactly. This means that the traction increments are equal to zero at the point of necking, which leads to the local necking criterion (Alsos et al., 2008):

$$\frac{d\sigma_1}{d\epsilon_1} = \sigma_1(1 + \beta) \quad 2-49$$

In Hill's local necking criterion, it is assumed that the stress-strain curve can be described by the power law equation, $\sigma_{eq} = K\epsilon_{eq}^n$, which is described in section 2.4.3, and that there is proportionality between stress rates and stresses, $\alpha = \frac{\dot{\sigma}_2}{\dot{\sigma}_1} = \frac{\sigma_2}{\sigma_1}$.

At local necking the equivalent strain is given by $\epsilon_{eq} = \frac{2n}{\sqrt{3}} \frac{\sqrt{\beta^2 + \beta + 1}}{1 + \beta}$. From this equation, a path independent stress based FLC (forming limit curve) can be found, and gives the equivalent stress at local necking:

$$\sigma_{eq} = K \left(\frac{2\hat{\epsilon}_1}{\sqrt{3}} \frac{\sqrt{\beta^2 + \beta + 1}}{1 + \beta} \right)^n \quad 2-50$$

These equations result in the equation for major principal stress in the negative regime:

$$\sigma_1 = \frac{2K}{\sqrt{3}} \frac{1 + \frac{1}{2}\beta}{\sqrt{\beta^2 + \beta + 1}} \left(\frac{2}{\sqrt{3}} \frac{\hat{\epsilon}_1}{1 + \beta} \sqrt{\beta^2 + \beta + 1} \right)^n \quad 2-51$$

A more detailed derivation of Hill's local necking criterion is shown in appendix A.2.

In the BWH instability criterion, the material is assumed to have isotropic plastic properties and is modeled by the plane stress J_2 flow theory. A modified power law formulation represents the equivalent stress-strain relationship and includes the plateau strain ($\epsilon_{plat} = 0$ for aluminium), it is shown in equation (Alsos et al., 2009):

$$\sigma_{eq} = \begin{cases} \sigma_y & \text{if } \epsilon_{eq} \leq \epsilon_{plat} \\ K(\epsilon_{eq} + \epsilon_0)^n & \text{otherwise} \end{cases} \quad 2-52$$

where the strain ϵ_0 is given by:

$$\epsilon_0 = \left(\frac{\sigma_Y}{K} \right)^{1/n} - \epsilon_{plat} \quad 2-53$$

When applying the BWH instability criterion to a finite element code, the failure is checked only in the mid-through-thickness integration point of every shell element. When the criterion is violated in an element, fracture is initiated by removing the element. The criterion searches for local instability, so it only applies to membrane stresses and strains, and thus the effect of bending is left out (Alsos et al., 2009).

3 Finite Element Method

All numerical simulations in this master thesis are completed using the finite element analysis (FEA) software Abaqus/CAE. This chapter gives a brief presentation of the relevant theory for dynamic and quasi-static analyses and numerical modeling. In addition, theory on energy balance is included here.

3.1 Explicit analysis

There are two different direct integration schemes available for solving dynamic problems; Explicit, where the solution is obtained in terms of known quantities, and implicit, where the solution is obtained in terms of unknown quantities. In this master thesis, the explicit method was used. The explicit method is preferable when solving problems regarding discontinuous nonlinearities such as material failure and contact, and is ideal for high speed dynamic simulations where small time increments are required. The method does not require any equation solving, which indicates computational inexpensive time increments, and equilibrium iterations are not necessary, so convergence is not a problem. One problem with the explicit method is that it is conditionally stable which means that it requires very small time steps (Mathisen, 2014e). The explicit, dynamics analysis procedure in Abaqus/Explicit is based on implementing an explicit integration rule together with using a lumped element mass matrix, i.e. a diagonal mass matrix (Dassault Systems, 2014).

The equation of motion for a multi degree of freedom system at a time t can be written as (Mathisen, 2014e):

$$\{R^{ine}(t)\} + \{R^{dmp}(t)\} + \{R^{int}(t)\} = \{R^{ext}(t)\} \quad 3-1$$

Where $\{R^{ext}(t)\}$ is the external force vector for the structure, and the inertia forces, damping forces and internal forces can be expressed by:

$$\{R^{ine}(t)\} = [M]\{\ddot{D}(t)\} \quad 3-2$$

$$\{R^{dmp}(t)\} = [C]\{\dot{D}\} = (\alpha[M] + \beta[K])\{\dot{D}\} \quad 3-3$$

$$\{R^{int}(t)\} = [K]\{D(t)\} \quad 3-4$$

Where $[M]$ is the mass matrix, $[C]$ is the damping matrix and $[K]$ is the stiffness matrix. The displacement, velocity and acceleration, $\{D\}$, $\{\dot{D}\}$ and $\{\ddot{D}\}$ respectively, will be solved by explicit solution method.

From this, the governing equations of structural dynamics can be expressed as (Mathisen, 2014e):

$$[M]\{\ddot{D}(t)\} + [C]\{\dot{D}\} + [K]\{D(t)\} = \{R^{ext}(t)\} \quad 3-5$$

3.1.1 Explicit Direct Integration

In a multi degree of freedom system, the dynamic equilibrium is considered at time t_n to calculate the displacement at time t_{n+1} . The equation of motion (Equation 3-5) can be solved in this manner by employing the central difference method. There are two forms of the central difference method that will be described here, the classical central difference method and the half-step central difference method (Cook et al., 2002).

The central difference method for the velocity and acceleration, is approximated by the following equations, respectively (Cook et al., 2002):

$$\{\dot{D}\}_n = \frac{1}{2\Delta t} (\{D\}_{n+1} - \{D\}_{n-1}) \quad 3-6$$

$$\{\ddot{D}\}_n = \frac{1}{\Delta t^2} (\{D\}_{n+1} - 2\{D\}_n + \{D\}_{n-1}) \quad 3-7$$

Equation 3-6 and 3-7 can be obtained from a Taylor series expansion of $\{D\}_{n+1}$ and $\{D\}_{n-1}$. By neglecting Δt to powers higher than second, the primary error term is proportional to Δt^2 . This means that it has second order accuracy. By substituting equation 3-6 and 3-7 into the equation of motion (Equation 3-5), it provides (Cook et al., 2002):

$$\begin{aligned} & \left[\frac{1}{\Delta t^2} M + \frac{1}{2\Delta t} C \right] \{D\}_{n+1} \\ & = \{R^{ext}\}_n - \{R^{int}\}_n + \frac{2}{\Delta t^2} [M]\{D\}_n - \left[\frac{1}{\Delta t^2} M - \frac{1}{2\Delta t} C \right] \{D\}_{n-1} \end{aligned} \quad 3-8$$

If the mass and damping matrices are not diagonal, it is necessary to establish and factorize an effective stiffness $[K^{eff}]$ in order to obtain the displacement $\{D\}_{n+1}$ (Mathisen, 2014e):

$$\{D\}_{n+1} = [K^{eff}]^{-1}\{R^{eff}\}_n \quad 3-9$$

$$[K^{eff}] = \frac{1}{\Delta t^2}[M] + \frac{1}{2\Delta t}[C] \quad 3-10$$

In a general dynamic response analysis it can be desirable to include stiffness-proportional damping $[C] = \beta[K]$ to damp high-frequency numerical noise. This makes the effective stiffness matrix $[K^{eff}]$ non-diagonal and thus the computational cost per time increases significantly. To overcome this problem, it is possible to establish the equilibrium equations with velocity lagging by half time step (Mathisen, 2014e). Hence, the half-step central difference method is established by the following equations for velocity and acceleration, respectively (Cook et al., 2002):

$$\{\dot{D}\}_{n-1/2} = \frac{1}{\Delta t} (\{D\}_n - \{D\}_{n-1}) \quad 3-11$$

$$\{\dot{D}\}_{n+1/2} = \frac{1}{\Delta t} (\{D\}_{n+1} - \{D\}_n) \quad 3-12$$

$$\{\ddot{D}\}_n = \frac{1}{\Delta t} (\{\dot{D}\}_{n+1/2} - \{\dot{D}\}_{n-1/2}) = \frac{1}{\Delta t^2} (\{D\}_{n+1} - 2\{D\}_n + \{D\}_{n-1}) \quad 3-13$$

The equation of motion is rewritten with velocity lagging by half a time step by using the equations (Cook et al., 2002):

$$\{D\}_{n+1} = \{D\}_n + \Delta t\{\dot{D}\}_{n+1/2} \quad 3-14$$

$$\{\dot{D}\}_{n+1/2} = \{\dot{D}\}_{n-1/2} + \Delta t\{\ddot{D}\}_n \quad 3-15$$

Thus, the equation of motion can be written as:

$$[M]\{\ddot{D}\}_n + [C]\{\dot{D}\}_{n-1/2} + \{R^{int}\}_n = \{R^{ext}(t)\}_n \quad 3-16$$

Combination of these equation provides (Cook et al., 2002):

$$\begin{aligned} \frac{1}{\Delta t^2} [M] \{D\}_{n+1} \\ = \{R^{ext}\}_n - \{R^{int}\}_n + \frac{1}{\Delta t^2} [M] \left(\{D\}_n + \Delta t \{\dot{D}\}_{n-\frac{1}{2}} \right) \\ - [C] \{\dot{D}\}_{n-1/2} \end{aligned} \quad 3-17$$

When $n=0$, $\{\dot{D}\}_{-\frac{1}{2}}$ is needed on the right hand side of the equation. This is obtained by a backward difference approximation (Cook et al., 2002):

$$\{\ddot{D}\}_0 = \frac{1}{\Delta t/2} \left(\{\dot{D}\}_0 - \{\dot{D}\}_{-1/2} \right) \quad 3-18$$

$$\{\dot{D}\}_{-1/2} = \{\dot{D}\}_0 - \frac{\Delta t}{2} \{\ddot{D}\}_0 \quad 3-19$$

Where $\{\ddot{D}\}_0$ is obtained by evaluating the equation of motion at time t_0 :

$$\{\ddot{D}\}_0 = [M]^{-1} \left(\{R^{ext}\}_0 - [K] \{D\}_0 - [C] \{\dot{D}\}_0 \right) \quad 3-20$$

The explicit method is conditionally stable, which means that the solution is only bounded when the time increment Δt is less than the stable time increment Δt_{cr} . In Abaqus/Explicit some damping is introduced to control high frequency oscillations, and thus the time increment is given by (Dassault Systems, 2014):

$$\Delta t \leq \frac{2}{\omega_{max}} \left(\sqrt{1 + \xi^2} - \xi \right) \quad 3-21$$

Where ξ is the damping ratio in the highest mode and reduces the stable time increment.

When there is no damping in the system, the stable time increment is given in terms of the highest eigenvalue of the system, ω_{max} (Dassault Systems, 2014):

$$\Delta t \leq \frac{2}{\omega_{max}} \quad 3-22$$

Abaqus/Explicit computes the stable time increment from the dilatational wave speed, c_d , and the characteristic length of the smallest element in the FE model, L^e (Mathisen, 2014e):

$$c_d = \sqrt{\frac{E}{\rho}} \quad 3-23$$

$$\Delta t \leq \frac{2}{\omega_{max}} = \frac{L^e}{c_d} \quad 3-24$$

E is the elastic modulus for the material and ρ is the mass density. Hence the stable time increment is determined by the smallest, stiffest and least dense element in Abaqus. The physical interpretation of Δt_{cr} is that Δt must be sufficiently small so that information does not propagate more than the distance between adjacent nodes during a single time step. Higher order elements have high frequencies compared to lower order elements, and tend to produce noise when stress waves move across the FE mesh. Thus should higher order elements be avoided when using explicit time integration. Similarly should small lumped masses be avoided since they make the eigenvalue of the system, ω_{max} , very large.

3.1.2 Contact

In a finite element analysis, a contact condition is a special class of discontinuous nonlinear constraints which allow forces to be transmitted from one part of the model to another. There are many different approaches for the solution of contact problems, for instance the Lagrange multiplier method and the penalty method. Abaqus/Explicit enforces contact constraints via the penalty method, only. The penalty method leaves the number of unknowns unchanged, but may in some cases produce an ill-conditioned set of equations (Mathisen, 2014e).

Abaqus/Explicit provides two algorithms for modelling contact; General contact and contact pairs. General contact allows a definition of contact between many or all regions of a model with a single interaction. This interaction typically include all bodies in the model and require very few restrictions on the types of surfaces involved. The surfaces involved in the contact domain can also be disconnected. Contact pairs describes the contact between two surfaces. This algorithm require a more careful definition of contact since every possible contact pair must be defined and it has many restrictions on the types of surfaces involved. The interactions must be defined by specifying each of the individual surface pairs that can interact with each other (Mathisen, 2014e).

3.1.2.1 The Penalty Contact Method

The penalty contact method impose the contact condition by extending the potential energy of the system by a penalty term, where the penalty parameter α can be interpreted as a spring stiffness in the contact interface (Mathisen, 2014e):

$$\Pi_p^* = \Pi_p + \frac{1}{2} \alpha [C(u)]^2 = \frac{1}{2} k u^2 - m g u + \frac{1}{2} \alpha (u - h)^2 \quad 3-25$$

The penalty parameter can be interpreted like this since the potential energy of the penalty term has the same structure as the potential energy of a simple spring, see Figure 3-1.

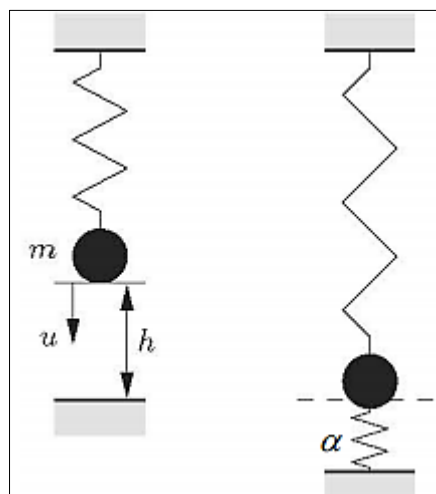


Figure 3-1: The Penalty Contact Method (Mathisen, 2014e)

To make Π_p^* stationary, the following equation needs to be satisfied (Mathisen, 2014e):

$$\left\{ \frac{\partial \Pi_p^*}{\partial u} \right\} = 0 \Rightarrow (k + \alpha)u = m g + \alpha h \quad 3-26$$

The value for the contact condition, and thus the contact force for the penalty method which equals the interface spring force then becomes, respectively:

$$C(u) = u - h = \frac{m g - k h}{k + \alpha} \quad 3-27$$

$$\lambda = \alpha C(u) = \frac{\alpha}{k + \alpha} (m g - k h) \quad 3-28$$

In case of contact $mg > kh$ and a point mass will penetrate into the rigid support. This is physically equivalent to a compression of the interface spring with stiffness α . The amount of penetration depends upon the penalty parameter and the contact condition is only satisfied in the limit (Mathisen, 2014e):

$$\alpha \rightarrow \infty \Rightarrow C(u) = u - h \rightarrow 0 \text{ or } u \rightarrow h \quad 3-29$$

Since the penalty parameter has to be chosen, it is distinguished between two limiting cases; the constrained solution obtained for a very large penalty parameter and the unconstrained solution obtained for a very small penalty parameter. The constrained solution leads to a very large spring stiffness, and a small penetration into a rigid surface. The unconstrained solution leads to a very small spring stiffness, and a large penetration into a rigid surface. The unconstrained solution is only valid in the case of no contact (Mathisen, 2014e).

3.2 Plate Theory

According to plate theory, a plate is thin if the ratio between the thickness and length is less than 1/10; $t/L = 1/10$. The xy -plane ($z=0$) of a plate with thickness t is located in a distance $t/2$ from each lateral surface, and it is assumed that the midsurface acts as a neutral surface, i.e. at $z=0$: $\varepsilon_x = \varepsilon_y = \gamma_{xy} = 0$, and that the normal strains in the thickness directions are zero, $\varepsilon_z = \frac{\partial w}{\partial z} = 0$ (Cook et al., 2002).

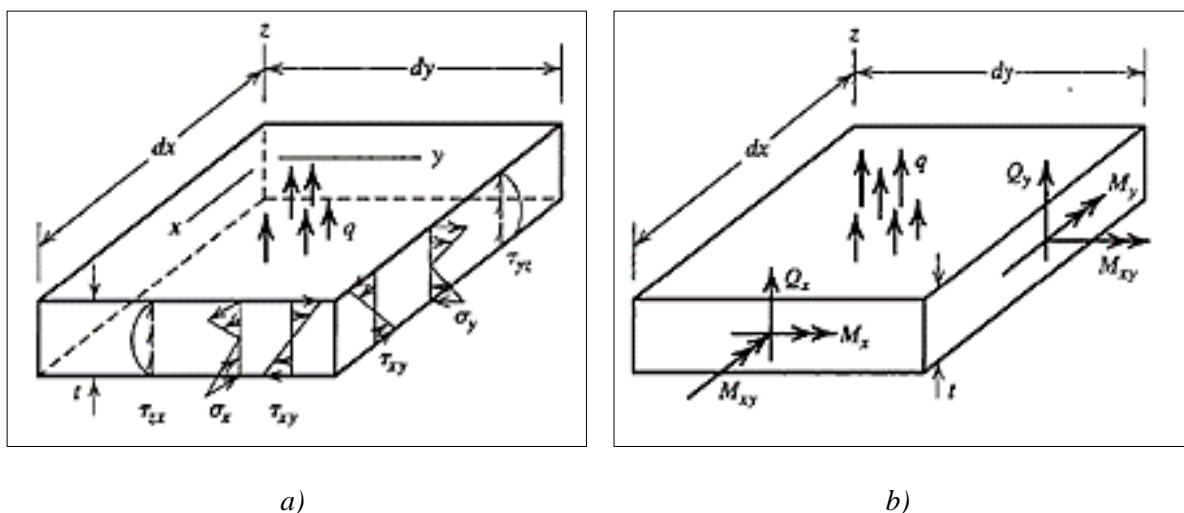


Figure 3-2: a) Stresses and distributed lateral force q on a differential element of a plate
b) Moment and transverse shear forces associated with stresses in a) (Cook et al., 2002)

Figure 3-2 shows the rates of change of the stress-resultants acting on a differential plate element. By this figure, the stress-resultants may be expressed in terms of displacements, for the moment and shear force in equation 3-30 and 3-31 respectively (Mathisen, 2014a):

$$M = \begin{bmatrix} M_x \\ M_y \\ M_{xy} \end{bmatrix} = -D\kappa \tag{3-30}$$

$$Q = \begin{bmatrix} Q_x \\ Q_y \end{bmatrix} = Gt_k\varepsilon_s \tag{3-31}$$

where κ is the curvature and D is the flexural rigidity and analogous to flexural stiffness EI of a beam in the moment equation. In the equation for the shear force, G is the shear modulus, ε_s is the shear strain and $t_s = kt$ is the effective stiffness for transverse shear deformation, where k accounts for the parabolic variation of transverse shear stress in the z -direction. For a homogenous plate, $k = 5/6$ (Mathisen, 2014a).

3.3 Shell Elements

A shell section can be derived from a plate section by forming the middle surface as a curved surface. The shell section supports external loads by the stress resultant acting as both bending (out-of-plane) and membrane (in-plane) stresses. The loading is carried primarily by membrane actions, so the bending stresses are low (Mathisen, 2014a). This is illustrated in Figure 3-3.

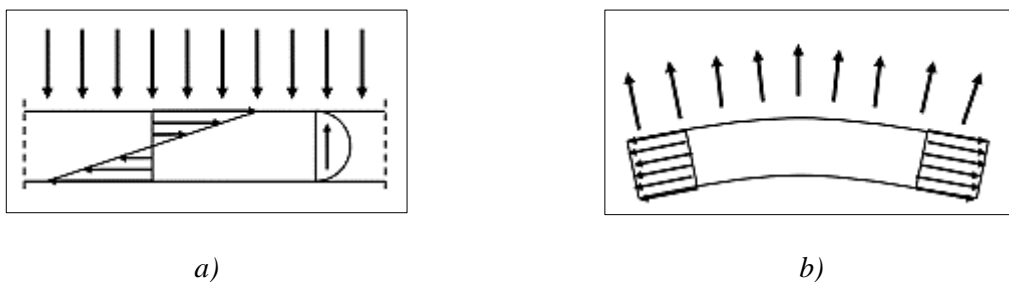


Figure 3-3: a) Load bearing by bending and b) membrane action (Mathisen, 2014a)

In Abaqus, there are three different types of shell elements; general purpose, thin and thick shell elements. The solutions provided for thin shell elements can be described by classical, Kirchhoff, shell theory while thick shell elements yield solutions for structures are best modeled by shear flexible, Mindlin, elements. Abaqus/Explicit only provides general purpose shell elements, which gives solutions for both thin and thick shell problems. The general-purpose shell elements used in this master thesis are S4R. These elements give robust and accurate

solutions in all loading conditions. The elements consider finite membrane strains as a default in Abaqus. They do not suffer from transverse shear locking and do not have any unconstrained hourglass modes. The thickness may change as a function of in-plane deformation. For explicit analysis, the thickness change is based on the “effective section Poisson ratio”, and is calculated using the equation: $\varepsilon_{33} = -\frac{\nu}{1-\nu} * (\varepsilon_{11} + \varepsilon_{22})$. The formulation of the S4R element can be found in the Abaqus 6.14 theory guide, section 3.6.5 (Dassault Systems, 2014).

3.4 Energy Balance

The law of conservation of energy states that, for an isolated system, the total energy over time stays constant. This implies that the time rate of change of kinetic energy and internal energy for a fixed body is equal to the sum of the rate of work done by the surface and body forces (Dassault Systems, 2014). The energy balance equation in Abaqus/Explicit can be written as (Simulia, 2014):

$$\begin{aligned} E_I + E_V + E_{FD} + E_{KE} + E_{IHE} - E_W - E_{PW} - E_{CW} - E_{MW} - E_{HF} & \quad 3-32 \\ = E_{total} = constant & \end{aligned}$$

where E_I is the internal energy, E_V is the dissipated viscous energy, E_{FD} is the dissipated frictional energy, E_{KE} is the kinetic energy, E_{IHE} is the internal heat energy, E_W is the work done by the externally applied loads, E_{PW} , E_{CW} and E_{MW} are the work done by contact penalties, constraint penalties and propelling added mass, and E_{HF} is the external heat energy through external fluxes. The sum, E_{total} , should be constant, generally with an error of less than 1% in numerical models .

For further information on energy balance, see the Abaqus Documentation, Getting started with Abaqus: Keyword Edition section 13.4 (Simulia, 2014) and section 1.5.5 in the Abaqus Theory Guide (Dassault Systems, 2014).

3.4.1 Energy Absorption

In large deformation processes of structures, many forms of irreversible energies exist. Some of these are plastic dissipation, viscous deformation energy and energy dissipated by friction or fracture. Energy absorption from plastic deformation is the most effective mechanism for absorbing energy in ductile materials (Lu and Yu, 2003).

When analysing the energy-absorption capacity of structures, the following energy method is frequently used. The general energy balance for an elastic-plastic structure is given by:

$$E_{in} = W^e + D \quad 3-33$$

Where E_{in} is the input energy, i.e. the external work applied, W^e denotes the elastic strain energy which is stored in the structure, and D the plastic energy dissipation. If the input energy is much larger than the elastic strain energy $E_{in} \gg W^e$, W^e may be neglected, and rigid-plastic models may be employed (Lu and Yu, 2003).

When analysing large deformations the object is regularly to find the limit load as a function of the deformation:

$$F = F(\Delta) \quad 3-34$$

A structure that experience large deformation under a load F leads to the energy balance shown in equation 3-35. Where the external work equals the area under the force-displacement curve and the dissipation D equals an integration of the incremental plastic dissipation during the deformation process. The final displacement is given by Δ_f .

$$E_{in} = \int_0^{\Delta_f} F(\Delta)d\Delta = D = \int_0^{\Delta_f} dD \quad 3-35$$

The kinetic energy of a indenter with a mass M and an intial velocity v_0 , have a kinetic energy

$$E_k = \frac{1}{2}Mv_0^2 \quad 3-36$$

The work-energy theorem states that the change in kinetic energy of an object is equal the net work done on the object (Lu and Yu, 2003):

$$W_{net} = \Delta E_k \quad 3-37$$

The change in kinetic energy of the indenter equals the input energy, giving the following energy balance:

$$\frac{1}{2}Mv_0^2 = \int_0^{\Delta_f} F(\Delta)d\Delta \quad 3-38$$

3.4.2 Energy Balance in Quasi-Static Analyses

For a test to be qualified as quasi-static the velocity should be very small and the inertia forces and the kinetic energy should be negligible (Abaqus Inc, 2005). The energy history should be as shown in Figure 3-4.

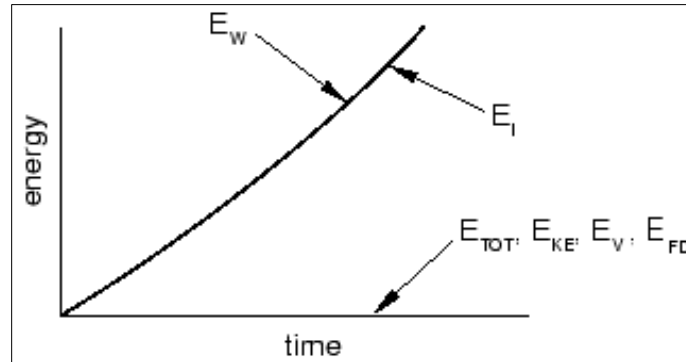


Figure 3-4: Energy history for quasi-static tensile test (Simulia, 2014)

In a quasi-static test, the work produced by the external forces should be nearly equal to the internal energy of the system. As mentioned, the kinetic energy should be negligible compared to the internal energy, typically 5-10% of the internal energy.

4 Experimental Set-up

For the experimental test, the dimensions of the welded aluminium plate and the rig had to be determined. The rig needed to be designed to fit both the aluminium plates used in this master thesis, and the steel plates used by fellow student Sindre Sølvernes in his master thesis. The size of the rig depends on the size of the aluminium plates and the steel plates, and limitations of the kicking machine used in the laboratory test, see section 4.1.1. Several different solutions for the welded plate and the rig was prepared and simulated in Abaqus/Explicit to find the optimal solution. First, a definition of impact loading and a description of machines and equipment which will be used in the laboratory experiment will be introduced.

4.1 Impact Load

A ship crashing into an aluminium structure characterizes as an impact loading since it is a dynamic effect on a stationary body hit by a short, forcible contact of another moving body (Dictionary of Construction, 2015). In the laboratory experiment, some of the aluminium plates will be subjected to a quasi-static load and some to dynamic loads with different velocities. Several shapes of indenters will be considered in the preliminary study. These are discussed in section 5.2.1, where some relevant results also are included. The shape that will be used in this introductory study to the laboratory experiment is a cylindrical indenter with diameter 50mm and length 300mm, shown in Figure 4-1. To try to re-enact a ship crashing into an aluminium construction in the best possible way, the impactor will have high mass and low velocity. The mass of the impactor is 1431 kg, and the initial velocity will be decided after the quasi-static component test has been conducted.

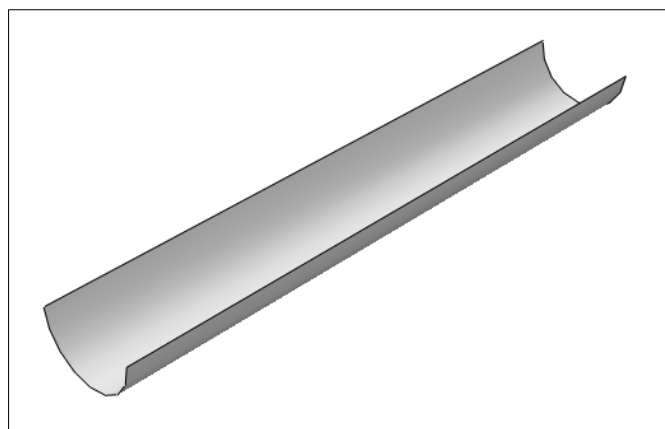


Figure 4-1: Cylindrical indenter shape in Abaqus

4 Experimental Set-up

4.1.1 The Kicking Machine

The impact testing of the aluminium plate will be performed by using the kicking machine at SIMLab, NTNU. The kicking machine accelerates a trolley up to the desired impact velocity. This accelerating force is produced by a hydraulic actuator which is connected to a rotating arm (Hanssen et al., 2003). The machine is shown in Figure 4-2, the rig will be mounted on the reaction wall, which is marked with a red circle, and the indenter will be installed on the trolley.

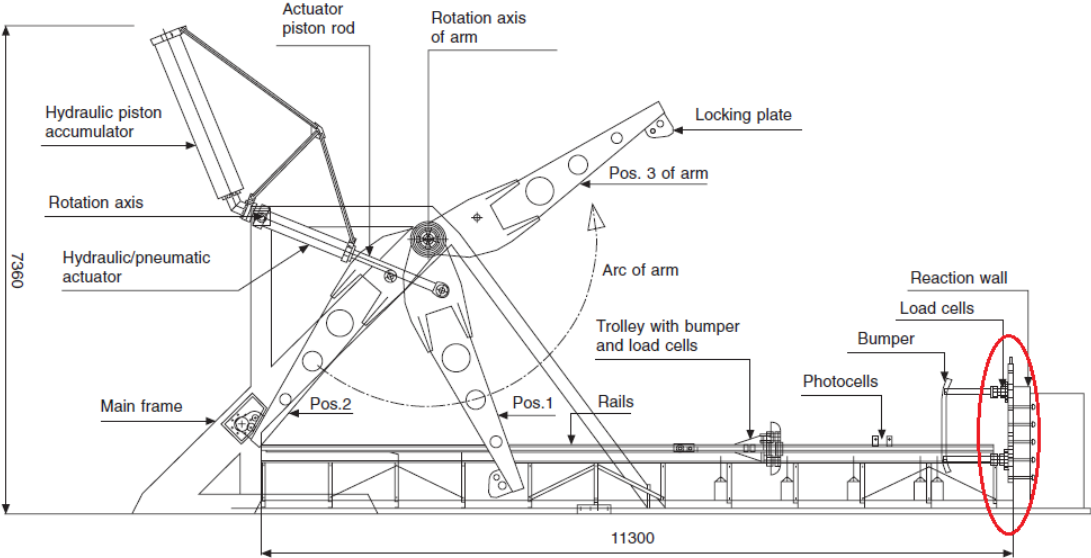


Figure 4-2: The Kicking Machine (Hanssen et al., 2003)

4.2 Support for Quasi-Static Test

For the quasi-static tests, the indenter will be installed at the tip (marked with a red circle) of a 1000 kN RDP-Howden-Ltd cylinder with a HBM load cell called U15/1MN shown in Figure 4-3. An extra support was needed to fit the rig into the testing machine. The support is shown in Figure 4-3, and capacity calculations will be presented in section 5.1.2. The rig with the plate will be placed on the support under the cylinder.



a)



b)

Figure 4-3: a) Quasi-static setup and b) support for quasi-static test

4.3 Introductory model

All the introductory revisions were simulated as nonlinear analyses in Abaqus/Explicit. The plate was implemented as a deformable part with shell elements and five integrations point through the thickness, and the rig and indenter as discrete rigid, see Figure 4-4. The plate was meshed with element size equal to the thickness (4mm) and the rig with element size two times the thickness (20 mm). For the indenter a mesh of 8 mm where used. To save unnecessary computational time, only one quarter of the rig, plate and indenter was modelled, with symmetry boundary conditions. The indenter will be given an initial velocity and hit the plate transversally to the stiffeners it is restricted from movements in all directions except in the loading direction. In revision 1, a surface to surface interaction with penalty contact was used and in the remaining, a general contact interaction was implemented for the whole model. The friction coefficient for contact between aluminum and steel was set to 0.61 (Engineers Handbook, 2006). In the experiments, teflon will be placed in between the plate and the rig (see Figure 4-7). This is done to ensure that the plate can move as frictionless as possible in the in-plane direction. Therefore, a frictionless contact condition was implemented in Abaqus in these surfaces in the introductory model. In this master thesis, a simplified constitutive material model with the von Mises yield criterion was used.

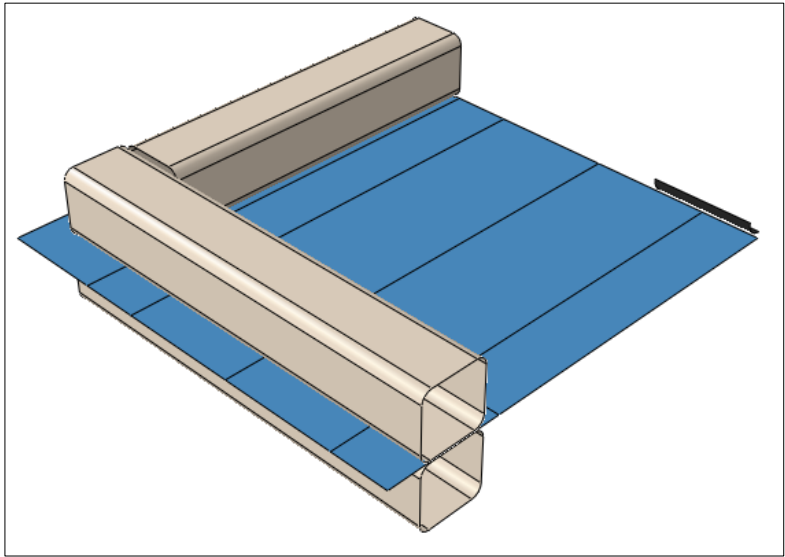


Figure 4-4: Abaqus model – Revision 1

4.3.1 Material

The material characteristics from the master thesis of Hildrum (2002) were used in the introductory model. Hildrum used aluminium alloy AA6082, temper T6, with the chemical composition given in Table 4-1 (Hildrum, 2002):

Table 4-1: Chemical composition of AA6082-T6 (Hildrum, 2002)

	Mg	Si	Mn	Fe	Cu	Cr	Zn	Ti	Al
Min (%)	0.4	0.6	0.4	-	-	-	-	-	Balance
Max (%)	1.4	1.6	1.0	0.5	0.1	0.1	0.2	0.1	

In all numerical simulations, Hildrum used a Young’s modulus of 70000 MPa and a Poisson’s ratio of 0.33. Hildrum established material parameters without damage, and including damage. The material parameters used in the preliminary model were the once not including damage, and are shown in Table 4-2. The Voce rule was used to fit a curve to the material parameters, by the method presented in section 2.4.3 (Hildrum, 2002).

Table 4-2: Hardening parameters (Hildrum, 2002)

Material	E [GPa]	σ_0 [MPa]	Q_{R1} [MPa]	C_{R1}	Q_{R2} [MPa]	C_{R2}
Base material	70.0	193	80.5	$3.21 \cdot 10^3$	68.9	20.3
Weld	70.0	134	69.0	27.7	130.0	5.8
HAZ1	70.0	110	45.9	$4.94 \cdot 10^3$	90.5	42.5
HAZ2	70.0	136	45.9	$4.94 \cdot 10^3$	90.5	42.5

In the simulations, when studying the equivalent plastic strain in the models, a limit value was implemented to study the deformations at fracture. From Chen et al. (2009) the average logarithmic strain at fracture for AA6082-T6 in uniaxial tension was found to be 0.707 in the direction of extrusion. In this introductory study, the equivalent plastic strain at fracture was set to be 0.7

4.4 Revisions of Plate and Rig

Multiple revisions of the aluminium plate and the supports were made in the process of finding the optimal solution for the plate and the rig. The extruded aluminium profile shown in Figure 4-5 was used in the first four revisions of the plate. The first three revisions are composed of three extruded aluminium profiles welded together with different solutions for the supports. In revision four, it was attempted to position the weld in the center of the plate.

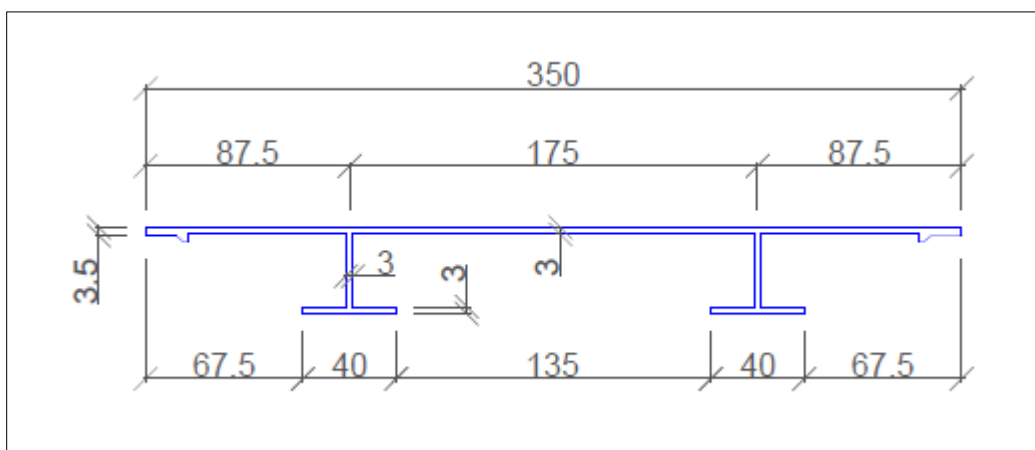


Figure 4-5: Extruded aluminium profile [mm]

4 Experimental Set-up

When the final drawings were sent to Sapa for manufacturing, they informed that they were not able to deliver the extruded aluminium profiles shown in Figure 4-5 in the agreed upon time. Therefore, Sapa suggested another extruded aluminium profile which would speed up the process of manufacturing. This meant that the original rig would have to be updated to fit the new profile. The new profile is shown in Figure 4-6 and revision 5 shows the final plate and rig.

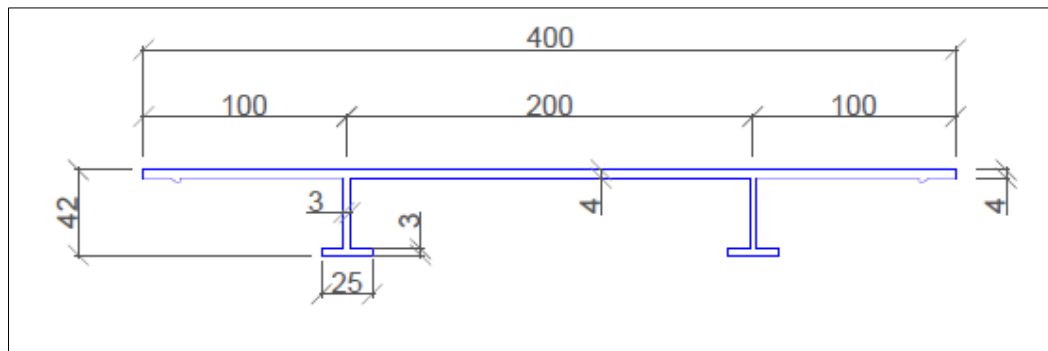


Figure 4-6: New extruded aluminium profile [mm]

All revisions of the rig are composed of four S355 steel RHS 100x100x10 profiles welded together on top of the plate and four on the bottom. The top and bottom parts of the rig are clamped together with bolts in different manners as will be described in the following, and are supported by eight RHS 100x100x10 with a length of 300mm, see Figure 4-9. The support legs will be mounted on the receiving wall, which gives an opening between the rig and the receiving wall. This is important, if the indenter goes through the plate it should not get in contact with the wall.

4.4.1 Revision 1

Revision 1 consists of three aluminium profiles welded together with one extruded 3.5 mm thick and 150 mm wide plate (marked in red) welded on the two sides that are parallel to the stiffeners length, as seen in Figure 4-7. In the longitudinal direction, the stiffeners are cut off to be able to have a smooth surface at the support area of the rig. The stiffeners are cut off at a distance of 25 mm from the rig to have room for deflection of the plate and potential rotation of the stiffeners. The distance between the RHS profiles is 1050 mm in both directions while the plate has a total length of 1350 mm in both directions.

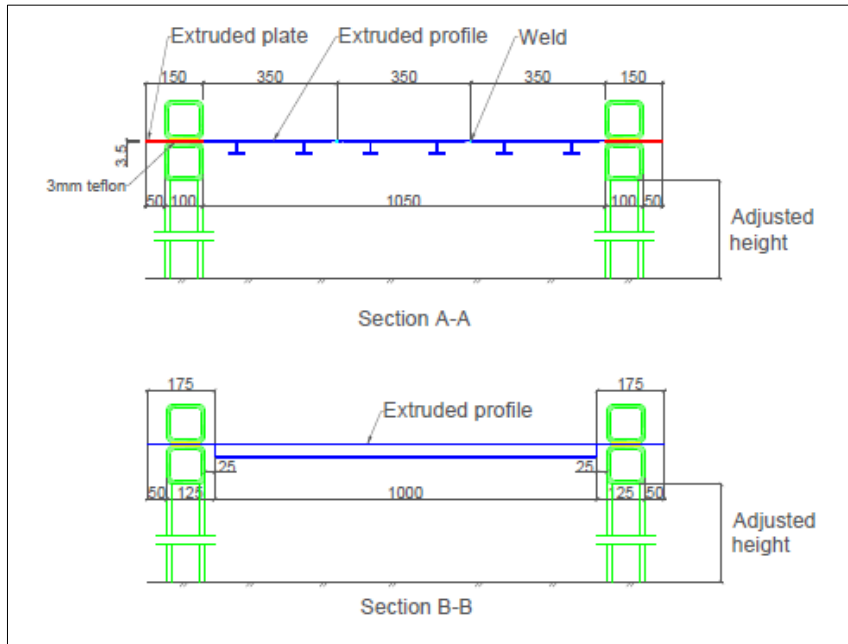


Figure 4-7: Revision 1 - Side view of plate and rig [mm]

The upper part of the rig will be clamped to the bottom part of the rig with eight bolts, in the corners and in the middle of the edges. To avoid unnecessary tension in the plate when deflected, cutouts are made for the bolts in the corners and in the middle of the ends in the plate. This is done so the plate can deform freely without any excessive tension. The plate with the cutouts is shown in Figure 4-8. Figure 4-9 shows the plate which consist of extruded aluminium profiles and plates in the steel rig. This figure also shows the placing of the bolts and the support legs.

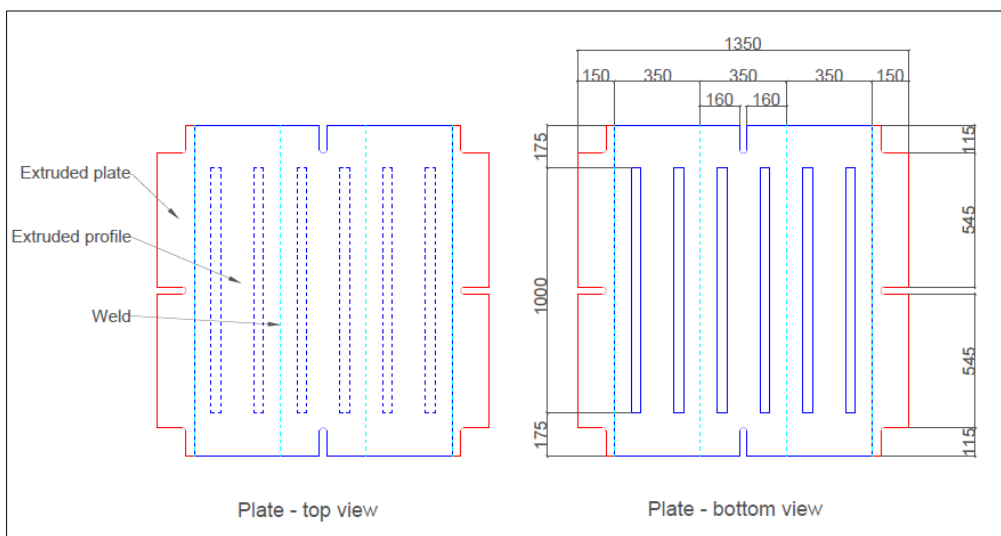


Figure 4-8: Revision 1- Aluminium profiles and plates with cutouts for bolts [mm]

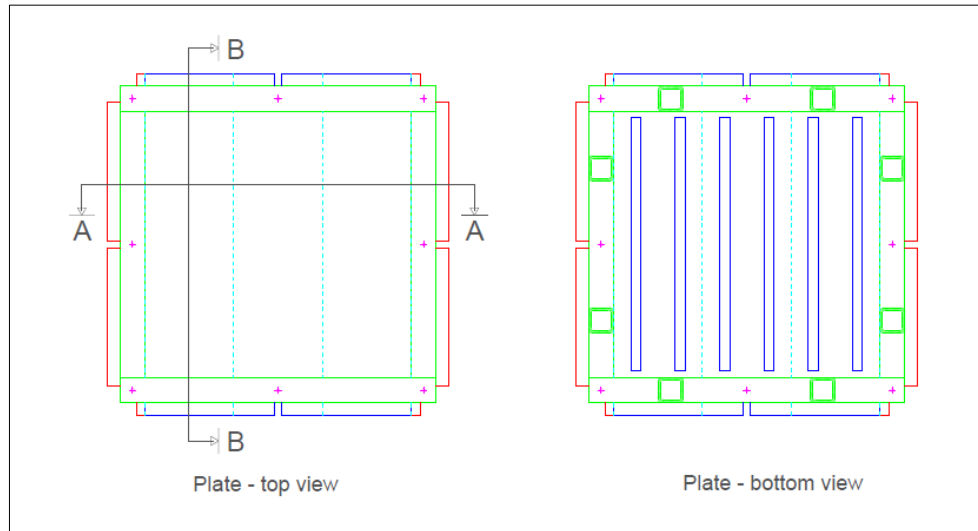


Figure 4-9: Revision 1 - Aluminium profiles and plates placed in the rig

The model was implemented in Abaqus/Explicit to check the displacement pattern and the stresses in plate. A surface to surface interaction was used between the plate and the rig, and between the plate and the indenter. The support legs was not modeled, because they would not have an effect when the rig is modeled as discrete rigid. To find the necessary initial velocity of the indenter which gives equivalent plastic strain of 0.7, a quasi-static analysis was run first. From this, the external energy was found, and thus the necessary velocity in the dynamic test, as described in section 3.4.1. In the quasi-static analysis, the mass was removed from the indenter and the velocity was set to be constant 0.5 m/s. When running quasi-static analyses in Abaqus, it is important that the kinetic energy is negligible compared to the internal energy and the external work should be equal to the internal energy, see section 3.4.2. For this revision, the necessary initial velocity in the dynamic simulation was calculated to be 3.469 m/s. The indenter hits the plate and bounces back .

The plot of the von Mises stresses from Abaqus/Explicit at maximum displacement is shown in Figure 4-10. The figure shows excessive stresses in the support area on the rig, where the stiffeners are cut off. The plate exhibited a maximum deflection of 111.39 mm and a maximum applied force of 165.4 kN.

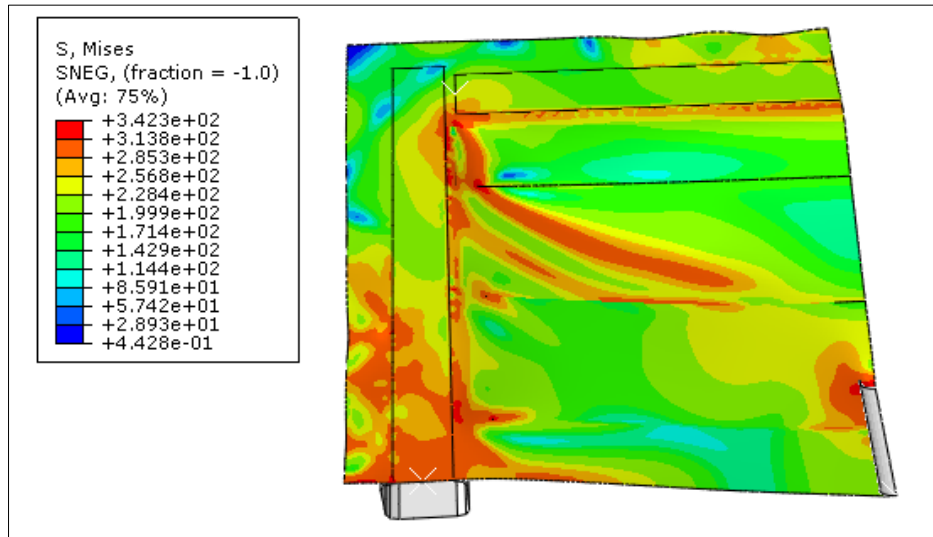


Figure 4-10: Revision 1- Von Mises stresses in the plate [MPa] (Top part of the rig is removed from results for better visibility)

4.4.2 Revision 2

In revision 2, an attempt was made to avoid the accumulation of stresses by the support area on the rig by letting the stiffeners be continuous. To make this possible, cutouts were made in the two RHS beam profiles in the transverse direction, as shown in Figure 4-11. In addition, after directions from Sapa, the extruded plate was replaced by an extruded profile cut to a necessary width of 150mm. This made it necessary to mill away the small “lip” on the edge of the profile shown in Figure 4-5, in all the places where it would be in contact with the rig.

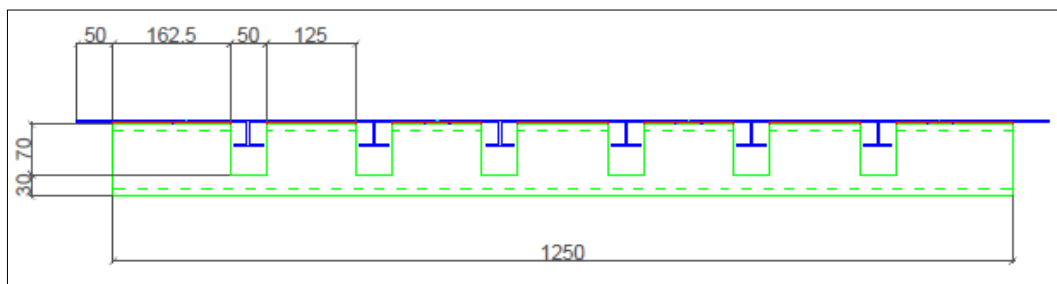


Figure 4-11: Revision 2- Cutouts in support [mm]

This model was also implemented in Abaqus/Explicit to check the displacement and tension pattern in the plate, and to be able to compare it to revision 1. Here, a general contact interaction was implemented to more easily include the interaction between the stiffeners and the cutouts. As was done in revision 1, the Abaqus/Explicit model was run as a quasi-static analysis first to find the necessary velocity to achieve an equivalent plastic strain of 0.7. This velocity was found to be 3.48 m/s for continuous stiffeners. As seen in Figure 4-12, there is noticeable local

4 Experimental Set-up

deformation of the stiffeners in the cutouts of the rig, and some rotation of the stiffeners. The plate exhibited a maximum deflection of 114.48 mm and a maximum applied force of 148.40 kN.

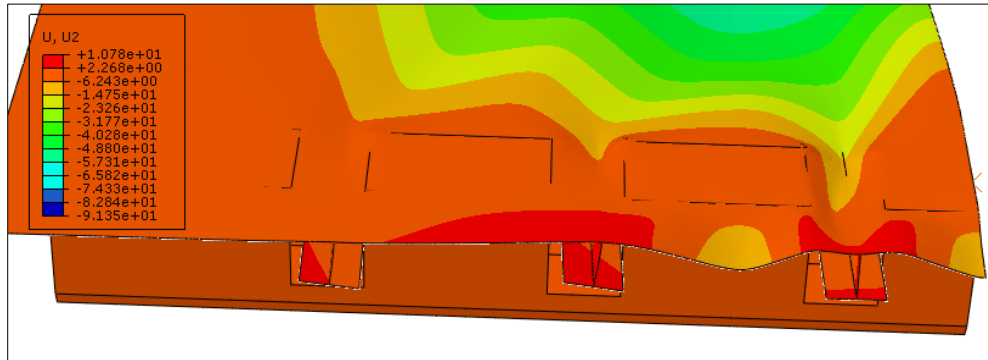


Figure 4-12: Revision 2 – Displacement in the vertical direction illustration the deformation in and around the stiffeners [mm]

4.4.3 Revision 3

The rotation and deformation in the stiffeners at and past the rig were attempted reduced by letting the plate only reach the end of the rig, and including L100x50x8 profiles under the plate. The L-profiles were placed under the plate in the rig on all sides. On the sides with cutouts, the L-profiles were cut to give a 10mm opening for the stiffeners. This solution also eliminated the need for cutouts for bolts by implementing a solution with welding pipes on the rig and leading bolts through the pipes to keep the upper and lower part of the rig together. This reduces the deflection and rotation around the cutouts, which was noticed in revision 2. The solution with the cutouts and the L-profile is shown in Figure 4-13. Only the part of the L-profiles that are placed under the plate was modelled.

It is clear from Figure 4-14 and Figure 4-15 that both the displacement around the cutouts and the rotation of the stiffeners are reduced for this solution. The quasi-static simulation gave a necessary velocity of 3.63 m/s at equivalent plastic strain of 0.7. At that point, the plate exhibited a deflection of 104.46 mm and an applied force of 189.44 kN.

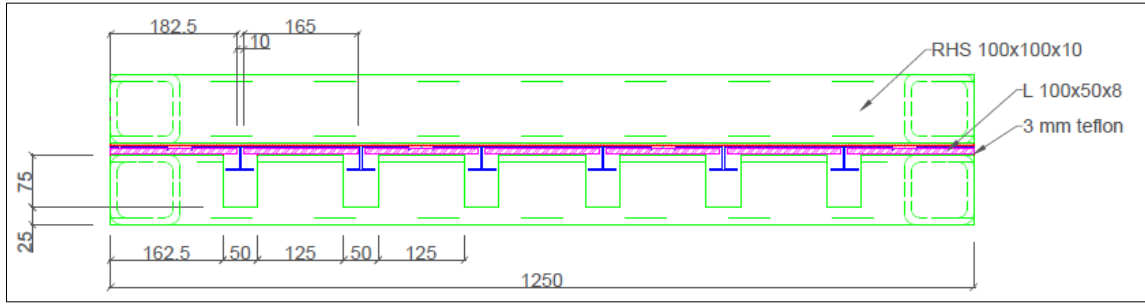


Figure 4-13: Revision 4 - Support, with L100x50x8

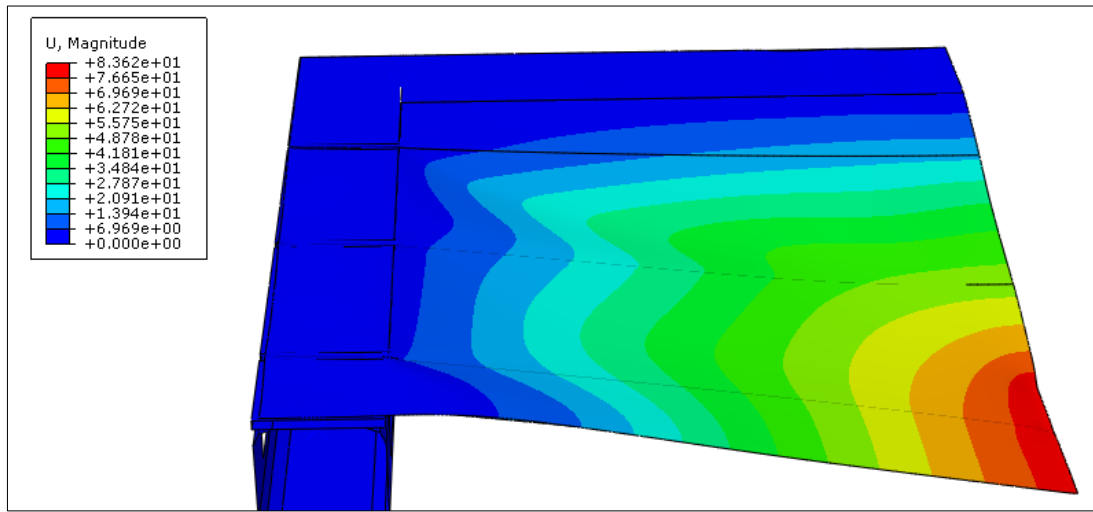


Figure 4-14: Revision 4 – Deformation in the plate

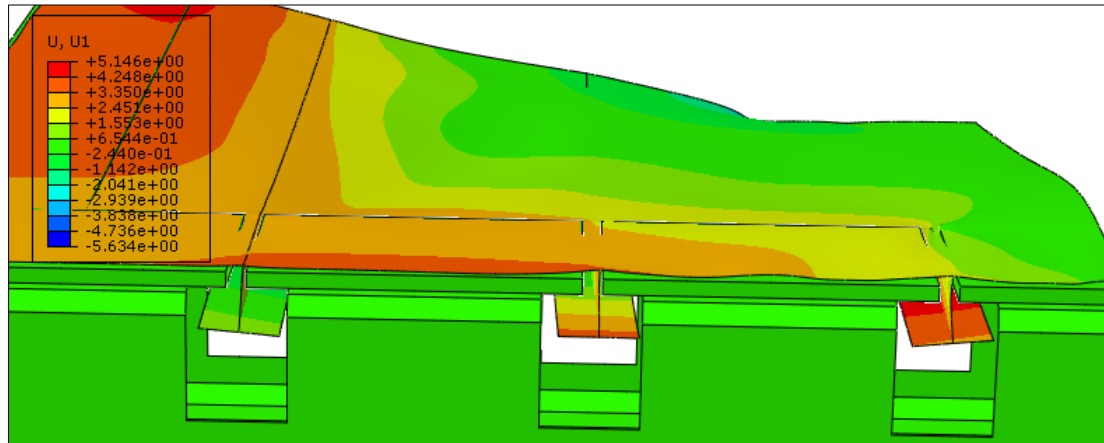


Figure 4-15: Revision 4 – Rotation of stiffeners

4 Experimental Set-up

4.4.4 Revision 4

An alternative solution to revision 3 is to place the aluminium profiles such that the weld is in the middle of the plate. Here, the characteristics of the welds shown in Table 4-2 was implemented for the friction stir welds (FSW) and the heat affected zones (HAZ). This solution was implemented in Abaqus/Explicit, but as expected, the plate showed a tendency to fail in the area of the FSW or the HAZ. Since this is expected to happen in every case, it is not interesting to consider this revision, but a plate where the indenter hits between two welds as in revision 3.

4.4.5 Revision 5

This revision was made after the new profile was provided by Sapa. The width of the plate needed to be changed so the stiffeners could have a sufficient distance to the support. Figure 4-16 and Figure 4-18 show the plate and rig with the new profile and Figure 4-17 shows the rig with the pipes welded on the sides and the eight support legs. In Figure 4-16 it is also shown where the small “lip” on the edge of the profile in Figure 4-6 had to be milled away over the support area of the rig.

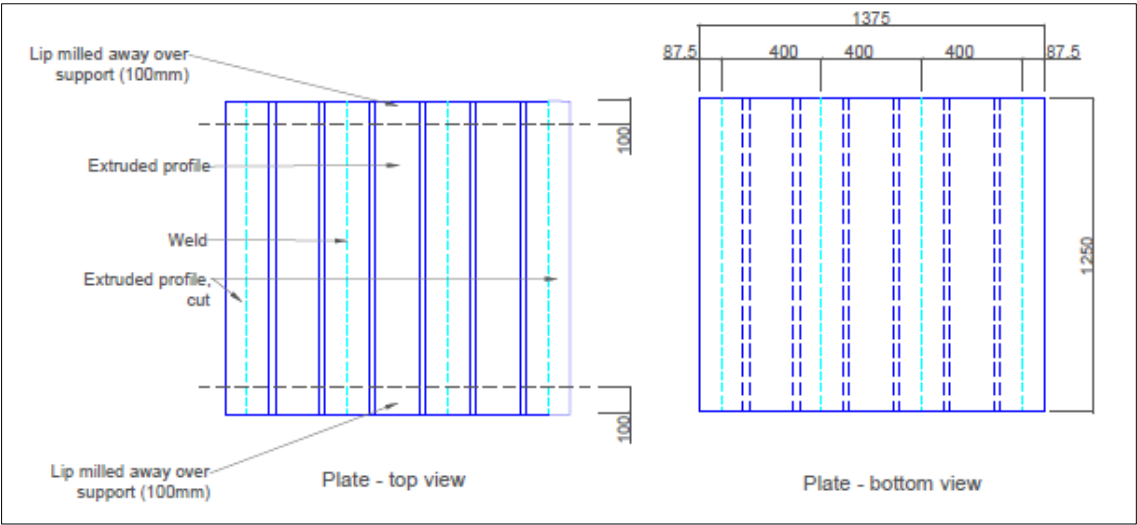


Figure 4-16: Revision 5 - Plate for new aluminium profile

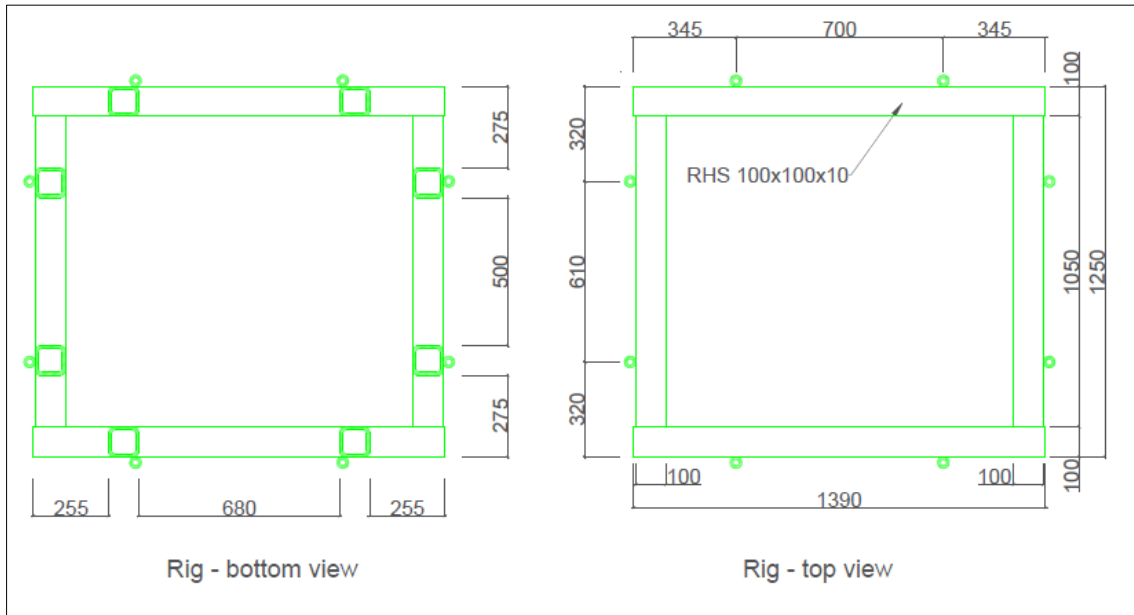


Figure 4-17: Revision 5 – Rig for new aluminium profile

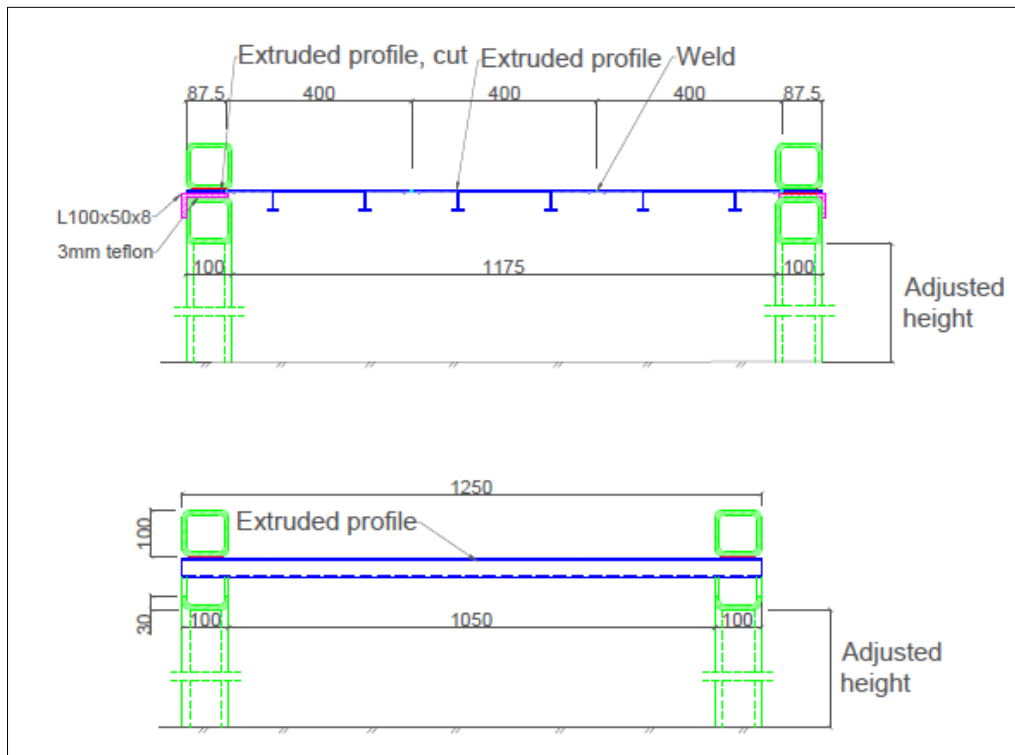
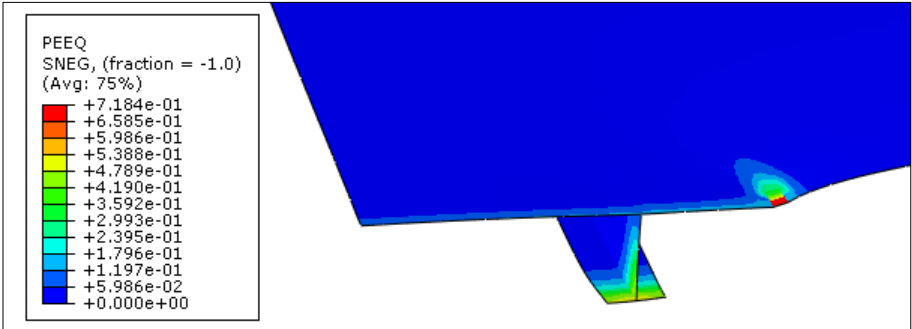


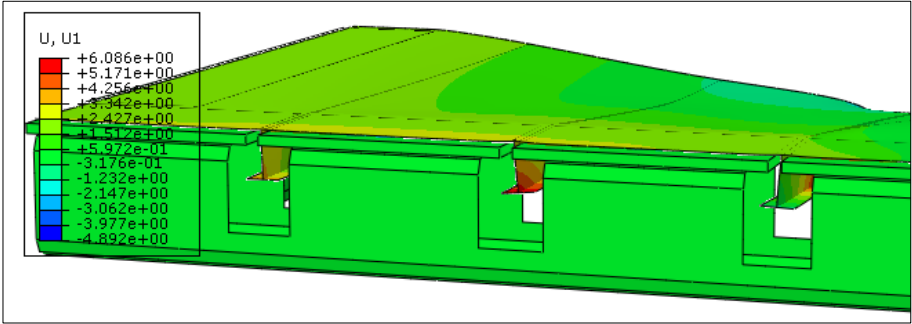
Figure 4-18: Revision 6 - Side view of plate and rig

4 Experimental Set-up

In the numerical model some changes were made to the contact formulations to account for some unrealistic displacement in the plate. The contact between the rig and the plate was excluded from the general contact and substituted by a surface-to-surface contact with penalty constraint method. Figure 4-19 shows revision 6 implemented in Abaqus CAE, run with a velocity of 3.31 m/s, that was found from a quasi-static simulation. This gave an equivalent plastic strain of 0.72 in the plate, a maximum force of 175.6 kN and maximum displacement of 87.1 mm. Figure 4-19 also shows the displacement in the horizontal direction which illustrates that there is only moderate rotation in stiffeners.



a)



b)

Figure 4-19: Revision 6 – a) Equivalent plastic strain in the impact area and b) Rotation of the stiffeners

5 Preliminary Analysis

In the preliminary analysis, analytical calculations were performed for the bolts and the quasi-static support to find their capacities. In addition, preliminary numerical nonlinear analyses and a parameter study has been conducted to investigate the effect of different parameters, and possibly improve the numerical model. This includes a study to find which indenter shapes that would be interesting to consider in the laboratory experiment, and to study the effect of some parameters (mesh and friction coefficients) in the simulations.

5.1 Analytical Calculations

Analytical calculations were performed to make sure the components that will be used in the component tests will sustain the loading that will be applied.

5.1.1 Nominal Capacity of Bolts

The bolts used in the connection between the upper and lower part of the rig are of class 12.9 and size M16. The nominal capacity for the bolts in tension and shear is calculated using the following equations, respectively (European Committee for Standardization (CEN), 2008):

$$F_{t,Rd} = \frac{k_2 * f_{ub} * A_s}{\gamma_{M2}} \quad 5-1$$

$$F_{v,Rd} = \frac{\alpha_v * f_{ub} * A_s}{\gamma_{M2}} \quad 5-2$$

Where k_2 is an empirical factor ($k_2=0.9$), α_v is assumed to be 0.6 for class 12.9, γ_{M2} is the material factor ($\gamma_{M2} = 1.25$) (European Committee for Standardization (CEN), 2008), f_{ub} is the ultimate stress (for bolts with class 12.9, $f_{ub}=1220$ MPa) and A_s is the tension area of the bolt (for M16 bolts, $A_s=157$ mm²) (Tingstad, 2015). This gives a nominal capacity of the bolts of:

$$F_{t,Rd} = 137.9 \text{ kN}$$

$$F_{v,Rd} = 91.94 \text{ kN}$$

For a combination of tension and shear, the following equation should be checked (European Committee for Standardization (CEN), 2009):

$$\frac{F_{v,Ed}}{F_{v,Rd}} + \frac{F_{t,Ed}}{1.4F_{t,Rd}} \leq 1.0 \quad 5-3$$

5.1.2 Capacity of Support for Quasi-Static Test

The capacity for the support that will be used in the quasi-static test (section 4.2) was simplified by assuming the section is in class 1, and thus it is possible to calculate the plastic moment capacity using the equation (European Committee for Standardization (CEN), 2008):

$$M_{pl,Rd} = \frac{W_{pl} * f_y}{\gamma_{M0}} \quad 5-4$$

For the complete calculation of the moment capacity, see appendix B.1. The plastic section modulus was found to be: $W_{pl} = 972515 \text{ mm}^3$, and thus the plastic moment capacity could be calculated:

$$M_{pl,Rd} = 328.8 \text{ kNm}$$

This moment capacity gives a maximum force applied to the rig:

$$F_{Rd} = 1400 \text{ kN}$$

5.2 Deformable Rig Model

After the final revision on the plate and the rig was determined (revision 5 in section 4.4.5), simulations were performed in Abaqus/Explicit, in order to decide how to approach the laboratory experiment and for improvements of the numerical model. First, the material implementation was changed from the introductory revision to a material card from SIMLab Metal Model provided by Postdoc David Morin, see appendix E.1. In addition a transverse shear stiffness was calculated and implemented, $K_{11} = K_{22} = \frac{5}{6}Gt = 89743 \text{ N/mm}$ and $K_{12} = 0$, see section 3.2. Some key values from the material card are presented in Table 5-1 where the material is described by the Voce rule with one term. Second, the RHS beam profiles and the L-profiles in the rig were remodeled as deformable shell parts, and the bolts were implemented as beam elements with circular profile to make the model more realistic. The indenter was kept as a discrete rigid part. An additional RHS beam profile was added under the RHS beam profiles with cutouts to strengthen the rig. The numerical deformable-rig model which consists of a quarter of the rig and plate and indenter is shown in Figure 5-1. In this model, unlike in the rigid model used in the introductory model, the support legs were implemented in the numerical model. The RHS beam profiles and the L-profiles were assumed to have the material properties of S355 steel, and the bolts to have the material properties of a 12.9 bolt. The material

characteristics for the steel and the bolts are shown in Table 5-2, and both materials were modeled as perfectly plastic.

Table 5-1 Key values from the material card , names in brackets correspond to names in material card (see appendix E.1)

Young's modulus (E) [GPa]	Poisson's ratio (PR)	σ_0 (SIGMA0) [MPa]	C_1 (THETAR1)	QR (QR1) [Mpa]	D_c (DCRIT)	W_c (BIGS0) [MPa]
70.0	0.3	310.2	1524.23	62.7	1.0	279.2

Table 5-2: Material characteristics of S355 steel (Larsen et al., 1993) and 12.9 steel bolt (Tingstad, 2015)

	Density [kg/m ³]	Young's modulus [MPa]	Poisson's ratio	Yield stress [MPa]
S355 Steel	7.8	210000	0.3	355
12.9 Steel bolt	7.8	210000	0.3	1080

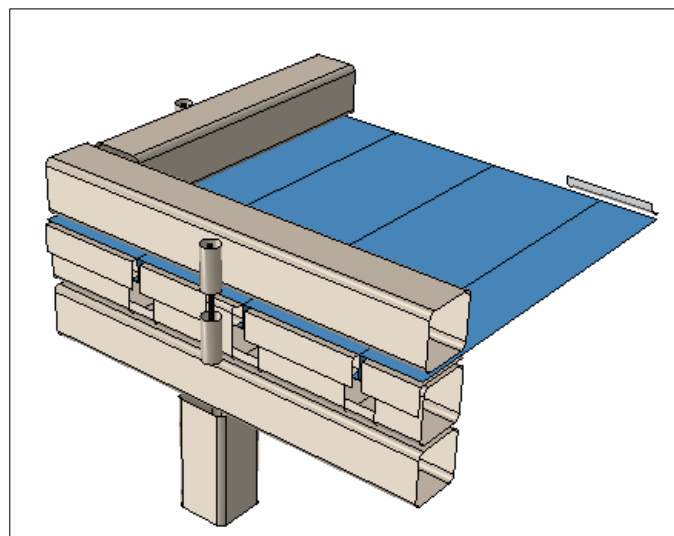


Figure 5-1: Abaqus model – one quarter of plate and rig

5 Preliminary Analysis

The Cockcroft-Latham parameter W_C and the critical damage factor D_c (section 2.6.2) is defined in the material card (Table 5-1). The damage factor is calculated in each of the five integrations point trough the thickness, and an element is removed when the damage factor is equal to one in all the integration points. If an integration point on one side reaches one, the next integration point trough the thickness will reach one soon after. The integration point with the highest damage factor is therefore a good indication on how close the simulation is to fracture. The accuracy of the exact time step where the element should be removed depends on the output frequency. It has therefore been decided to define fracture for the Cockcroft-Latham criterion, as the interval between the time step when one element is removed and the time step right before. The interval where fracture occurs is marked with a thicker line in the force-displacement curves.

In Figure 5-2 the force-displacement curves for a dynamic simulation of the rigid-rig model, used for Revision 5 (section 4.4.5), and the deformable-rig model are compared. Both are run with the material card. In the deformable-rig model, fracture is first initiated in the plate and then in the stiffeners while in the rigid-rig model fracture occurs in the same time-step for both the plate and the stiffeners. The maximum force is 11 % lower in the deformable-rig model compared to the rigid-rig model in a dynamic analysis with initial velocity 5m/s.

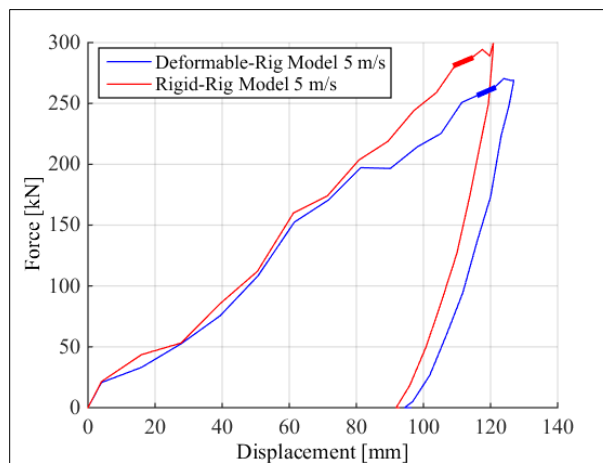


Figure 5-2: Dynamic simulation of rigid-rig model versus deformable-rig model

5.2.1 Quasi-Static Analysis

Since the laboratory experiment will include both dynamic and quasi-static tests, quasi-static nonlinear numerical analyses were performed in Abaqus/Explicit. In the quasi-static analysis, the mass was removed from the indenter and the velocity was set to be constant 0.5 m/s. The quasi-static analysis was used to determine the velocity of the indenter to initiate fracture. These calculations gave a velocity of 4.6 m/s, but to ensure fracture, the simulations were run with 5m/s. Figure 5-3 shows the force-displacement curve for the dynamic analysis versus the quasi-static analysis. This shows that there is not much difference between the dynamic and the quasi-static results.

When running quasi-static analyses in Abaqus, it is important that the kinetic energy is negligible compared to the internal energy. Figure 5-4 shows the energy balance for the quasi-static analysis. As mentioned in section 3.4.2, the external work should be equal to the internal energy and the kinetic energy should be negligible. In Figure 5-4 it is clear that the energy history for the simulated model is as desired for the quasi-static analysis.

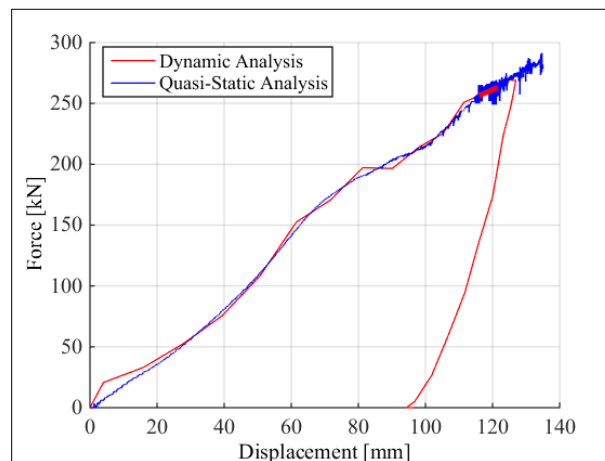


Figure 5-3: Dynamic versus quasi-static analysis for the deformable-rig model

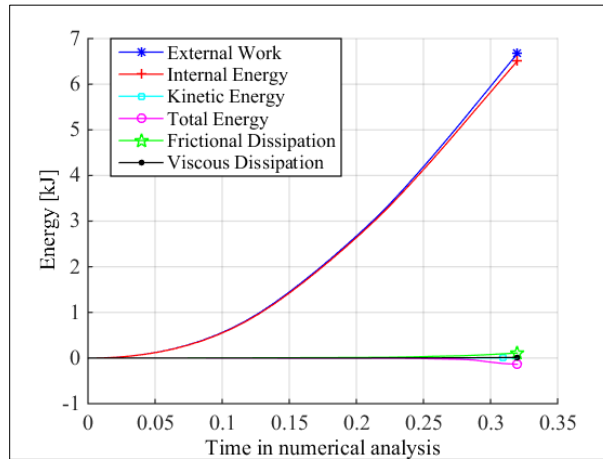


Figure 5-4: Energy history in quasi-static analysis for the deformable-rig model

5.2.2 Indenter Shapes

Two different indenters, one cylindrical and one spherical, were implemented in Abaqus/Explicit to investigate the impact on the structural behaviour of the aluminium plate. For the cylindrical indenter, the effects of the direction relative to the stiffeners was studied, if it should hit the plate longitudinal or transverse to the stiffeners. These simulations were used to determine which shapes are interesting to consider in the laboratory experiment.

5.2.2.1 Cylindrical Indenter

The indenter shape which was first used in the numerical analyses is shown in Figure 5-5. This is the same indenter shape which was used in the introductory model.

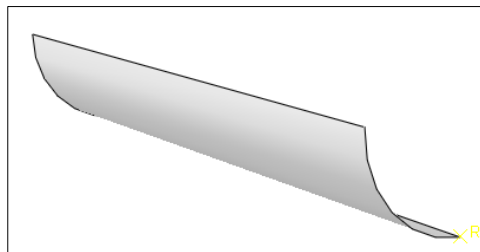


Figure 5-5: Indenter 1, quarter of the cylindrical indenter

After some numerical analyses were run with fracture, a trend with a localized deformation at the sharp edge of the cylindrical indenter was noticed. It was therefore attempted to implement a cylindrical indenter with rounded edges to avoid this localization of the fracture. The quarter of the indenter shape is shown below in Figure 5-6.

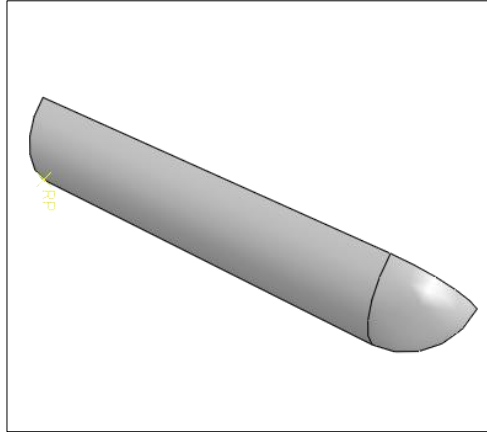
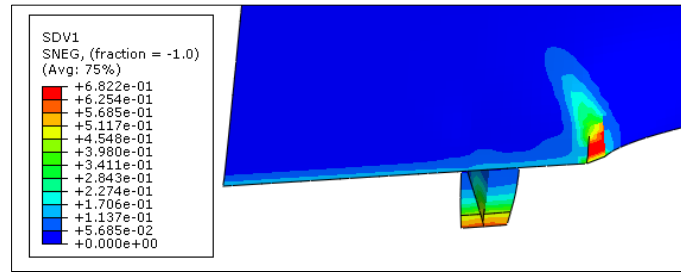
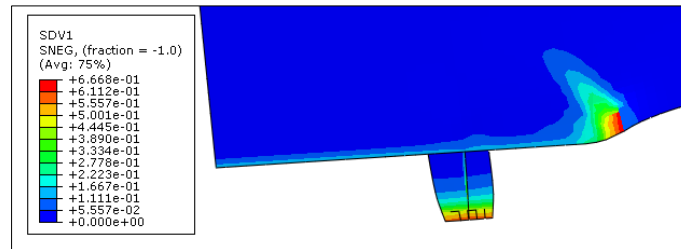


Figure 5-6: Indenter 2, quarter of the cylindrical indenter with rounded edges

In Figure 5-7 the equivalent plastic strain just before fracture (PEEQ in Abaqus) is shown for indenter 1 and indenter 2, respectively. For both indenter shapes, fracture occurs first in the plate and shortly after in the stiffeners. From the figure, it can be seen that there are higher strains around the edge of the indenter for the indenter with the sharp edges (a) than the indenter with rounded edges (b). For the cylindrical indenter with sharp edges, the PEEQ right before fracture is 0.68, and for the cylindrical indenter with rounded edges, the PEEQ right before fracture is 0.67. This is very close to the PEEQ used to define fracture in the introductory model. On the background of this, it was decided to proceed with indenter 2.



a)



b)

Figure 5-7: a) Equivalent plastic strain with indenter 1 and b) indenter 2.

The cylindrical indenter with rounded edges (indenter 2) was analysed in two directions, longitudinal and transversal to the stiffeners. The simulations were first run with 5 m/s, but this did not result in fracture when the indenter was placed longitudinal to the stiffeners. Therefore, a quasi-static analysis was run, and a velocity of 5.5 m/s was found to be necessary to ensure fracture. With the indenter longitudinal to the stiffeners fracture will occur in the plate, and the stiffeners are almost unaffected, while when the indenter is placed transverse to the stiffeners, the fracture occurs in the stiffeners right after it occurs in the plate. In Figure 5-8 the force-displacement of the two directions are compared, and it shows a higher force at fracture for the longitudinally placed indenter than the transversally placed indenter. On background of these observations, it was decided to do tests in both directions to be able to investigate the different fracture modes and why the plate requires a higher force in the longitudinal than the transverse direction.

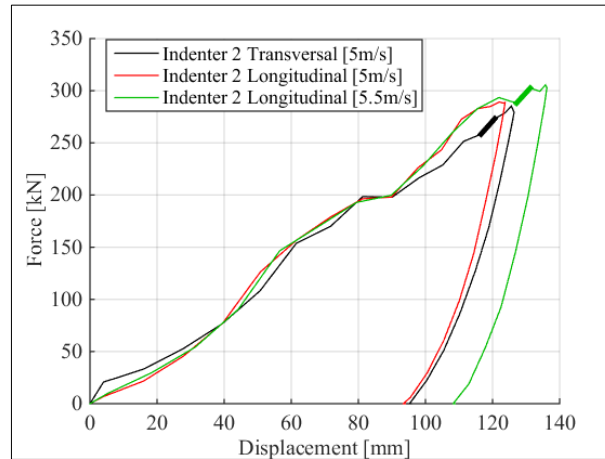


Figure 5-8: Indenter 2 in transversal and longitudinal direction

5.2.2.2 Spherical Indenter

A third indenter was explored, a sphere with diameter 100 mm. A quarter of indenter 3 was implemented in Abaqus/Explicit shown in Figure 5-9. Figure 5-10 shows the equivalent plastic strain right before fracture for the spherical indenter (indenter 3), and it is clear from this that the indenter provoked a localized deformation around the impact area, with no effect on the stiffeners. Figure 5-10 also shows how indenter 3 with the same velocity (5m/s) as indenter 2 went right through the plate. A part of the plate was ripped off where the displacement is measured, therefore the curve was cut off at fracture (marked with a red star) in the force-displacement curve, see Figure 5-11.

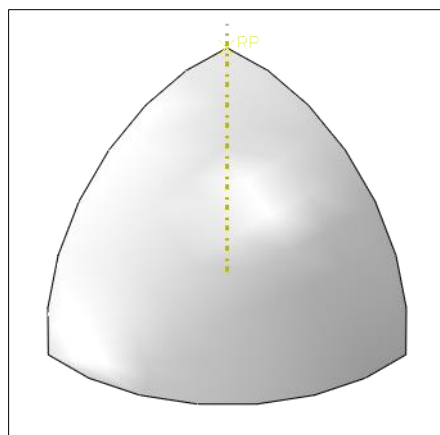


Figure 5-9: Indenter 3 - 100mm

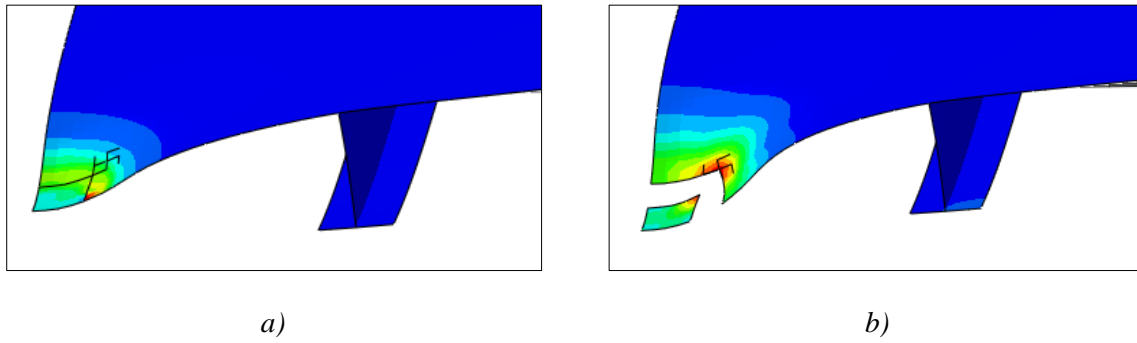


Figure 5-10: Equivalent plastic strain indenter 3 – spherical indenter 100 mm. Last frame before fracture (a) and after fracture (b)

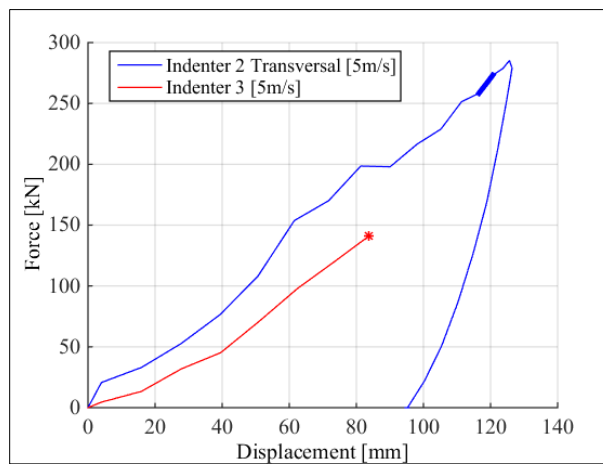


Figure 5-11: Cylindrical indenter with rounded edges (indenter 2) and Spherical indenter (indenter 3)

From these simulations, it was decided that it would be most interesting to use the cylindrical indenter with rounded edges in the laboratory experiments, not the spherical indenter. This is also supported by Liu et al. (2015) statement that the critical deflection and energy increase with the indenter width due to a decreased stress concentration with a wider contact area and thus a delayed crack initiation, see section 1.3 (Liu et al., 2015).

5.2.3 Mesh size on plate

The effect of the mesh size on the plate has been investigated. Simulations were run with indenter 2 transversal to the stiffeners with mesh size equal to the thickness, 1.5, 2, 3 and 5 times the thickness on the entire plate. From the plots in Figure 5-12, it is clear that the mesh size on the plate has a large impact on the results, fracture only occurs for the mesh size equal to the thickness. The force-displacement plots are very similar at the same velocity, but the damage factor is significantly lower for larger meshes. This implies that a larger mesh needs a higher velocity, and thus a higher applied force to initiate fracture. It is therefore reasonable to

assume that a mesh size equal to the thickness is the best choice. Table 5-3 shows the computational time for each mesh size.

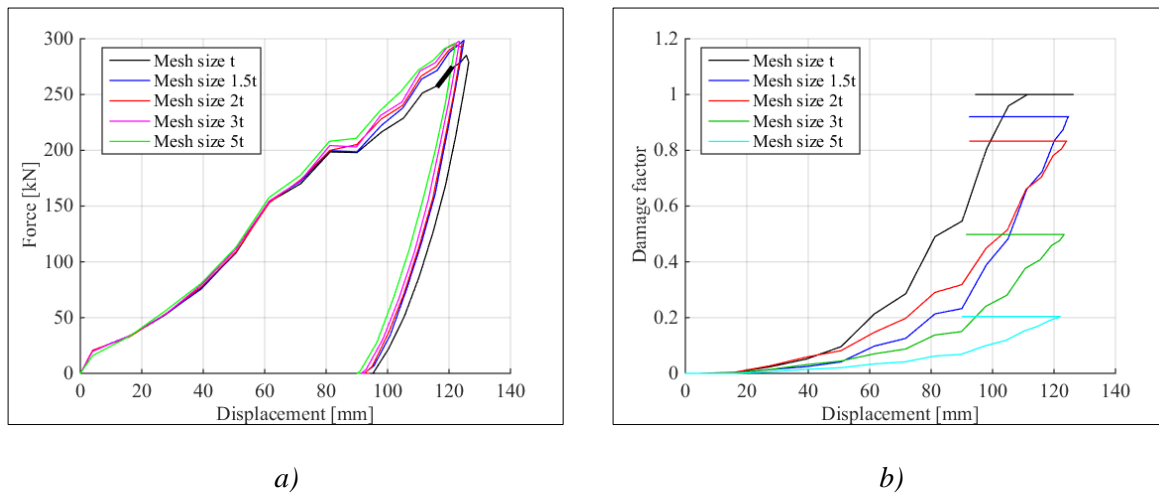


Figure 5-12: Effect of mesh size on plate on a) force-displacement and on b) damage factor

Table 5-3: Computational time for different mesh sizes

Mesh on plate	Computational time
Equal to thickness	3h 54 min
1.5 times the thickness	1h 10 min
2 times the thickness	40 min
3 times the thickness	13 min
5 times the thickness	6 min

There is a noticeable difference between the different mesh sizes, so it is desirable to look at the effect of dividing the plate into different regions with different meshes. To investigate the possibility of reducing the computational time, the mesh size was increased in parts of the plate. Mesh size equal to the thickness was kept in the impact area, and mesh size 5 times the thickness around the supports, this gave a computational time of 1h 12 min. The analysis did not initiate fracture in the stiffener, and gave a lower displacement than the analysis with mesh size equal to the thickness over the whole plate. Based on this, it was decided to continue to use a mesh size equal to the thickness on the entire plate.

5.2.4 Friction Coefficient between Support and Plate

The introductory analyses were run with a frictionless contact formulation between the plate and the support area on the rig. This is not realistic, and thus a parameter study with different friction coefficients was conducted. Force-displacement curves for the deformable-rig model with the different friction coefficient are displayed in Figure 5-13. The friction coefficient between teflon and aluminium was found to be approximately 0.18 (Blau, 1992) so friction coefficients around this value was checked.

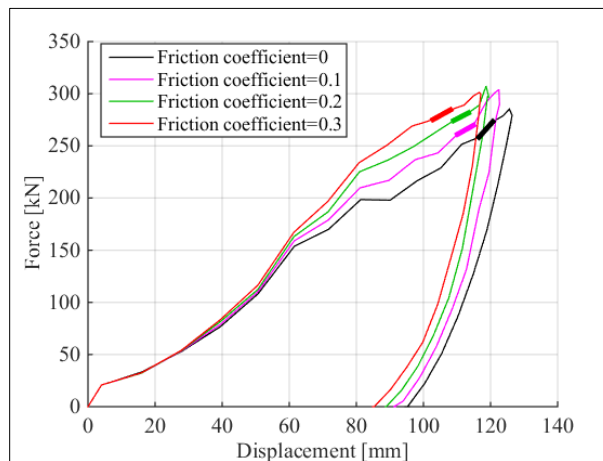


Figure 5-13: Effect of friction coefficient between teflon and plate

From the plot shown it is clear that the friction factor has a large impact on the maximum force, and when the fracture occurs. A higher friction factor between the teflon and the plate will fail at a higher force, but a lower displacement.

5.2.5 Friction Coefficient between Indenter and Plate

As mentioned in section 4.1 the friction coefficient between steel and aluminium was found to be 0.61. In the laboratory experiment, a spray will be used to lower the friction between the indenter and the plate (see section 7.1.1), so a parameter study was conducted to study the effect of the friction coefficient between the indenter and the plate, see Figure 5-14.

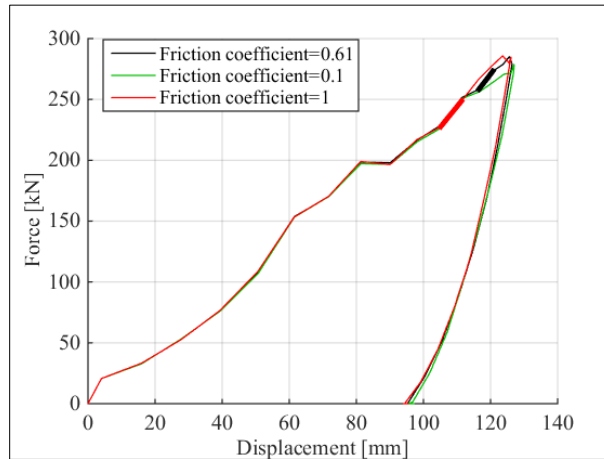


Figure 5-14: Effect of friction coefficient between indenter and plate

As seen from the plot shown above, the friction coefficient between the indenter and the plate has little to no effect on the force-displacement plot of the plate. It does, however, have an effect on whether or not fracture is initiated. With friction coefficient 0.1 fracture does not occur, and with friction coefficient 1, fracture occurs earlier than with friction coefficient 0.61.

5.2.6 Control of Forces in Rig

The deformations in the deformable-rig were checked. In the simulation in the previous sections, only negligible elastic deformations of the rig were detected due to the impact load. When controlling the forces in the bolt, it is important that the forces do not exceed the nominal capacity calculated in section 5.1.1. The forces in the bolts were taken from the simulation with indenter 2 transversal to the stiffeners, then compared with the capacities found in section 5.1.1 :

$$F_{t,Ed} = 99.97 \text{ kN}$$

$$F_{v,Ed} = 0.39 \text{ kN}$$

Since the tension force is much higher than the shear force in the bolt, the shear force is neglected. The tension force is compared to the capacity in tension:

$$F_{t,Rd} = 137.9 \text{ kN} > F_{t,Ed} = 99.97 \text{ kN}$$

The applied tension force in the bolt is lower than the capacity, therefore the bolts are assumed to work well for the experimental test with the indenter placed transversally to the stiffeners.

In the quasi-static test, both the bolt and the quasi-static support had to be checked. The tension force in the bolt is approximately the same as for the dynamic test, $F_{t,Ed} = 101.04 \text{ kN}$, which is lower than the capacity. The shear force is very low, $F_{v,Ed} = 0.53 \text{ kN}$, so it is neglected here as well. The maximum force applied to the rig by indenter 2 transversal to the stiffeners, is $F_{max,Ed} = 285.31 \text{ kN}$, which is much lower than the capacity for the maximum applied force, $F_{Rd} = 1400 \text{ kN}$.

5.3 Revision of Preliminary Model

There was done some small revisions to the preliminary model after performing the parameter study. After the study on the indenter shapes, it was decided to use the cylindrical indenter with rounded edges (indenter 2). The study on mesh size on the plate showed that the initial model with mesh size equal to the thickness should be used to get the most accurate solution for the Cockcroft-Latham fracture criterion. The friction coefficient between the plate and the support (teflon) was decided to change from frictionless to a friction of 0.2, since the frictionless assumption is very unlikely to be achieved in real life.

The friction coefficient between the indenter and the plate was decided to be keep at 0.61. The parameter study showed that the friction between the indenter and the plate had an impact on whether or not fracture occurred in the plate, since fracture occurred earlier for a higher friction coefficient and not at all for a lower one. Due to uncertainties, the friction coefficient between the indenter and the plate was decided to keep at 0.61.

6 Tensile Tests

This section looks into the tensile tests that were conducted to investigate the material properties of aluminium alloy, AA6082-T6. Tensile tests were performed in three different directions in relation to the extrusion direction, and in the stiffeners and over the weld. The chemical composition and the material properties displayed in Table 6-1 and Table 6-2, respectively, were provided by Sapa. The technical data sheet provided by Sapa is shown in appendix C.1. The yield stress differs considerably from the one used in the preliminary model (Table 5-1), and will most likely affect the simulations when implemented.

Table 6-1: Chemical composition according to EN-573-3:1994

	<i>Si</i>	<i>Fe</i>	<i>Cu</i>	<i>Mn</i>	<i>Mg</i>	<i>Cr</i>	<i>Zn</i>	<i>Ti</i>	<i>Others</i>
<i>Min [%]</i>	0.70			0.40	0.60				0.05
<i>Max [%]</i>	1.30	0.50	0.10	1.00	1.20	0.25	0.20	0.10	0.15

Table 6-2: Material properties according to EN 755-2:2008

$\sigma_{0.2}$ [MPa]	σ_u [MPa]	Vickers Typical Value
250	290	111

6.1 Uniaxial Tensile test

The tension tests were run in an Instron hydraulic machine with capacity 250 kN, which was connected to a computer, see Figure 6-1 a). The computer logs the force and the displacement of the crosshead ten times per second (10 Hz) during the test. An extensometer which logs the tensile extension of the specimen (at 10 Hz) was attached to the specimens during the test, see Figure 6-1 b). In addition to this, a camera took one picture per second which is intended for use in digital image correlation (DIC). For this purpose, the specimens were painted white and given a black speckle pattern.



a)



b)

Figure 6-1: a) uniaxial tensile test setup in Instron hydraulic machine and b) specimen with extensometer

6.1.1 Test geometry

Two different types of tensile specimens were used in the uniaxial tensile test, U110 and U200, the geometry of both is shown in Figure 6-2. To account for any inaccuracies in geometry, each specimen was measured using a micrometer. The red lines on the test specimens in Figure 6-2 show where the thickness and width was measured. This way the accurate cross sectional area was found and used to calculate the stress-strain relationship. The accurate measurements for all the tensile specimens are shown in appendix D.1.

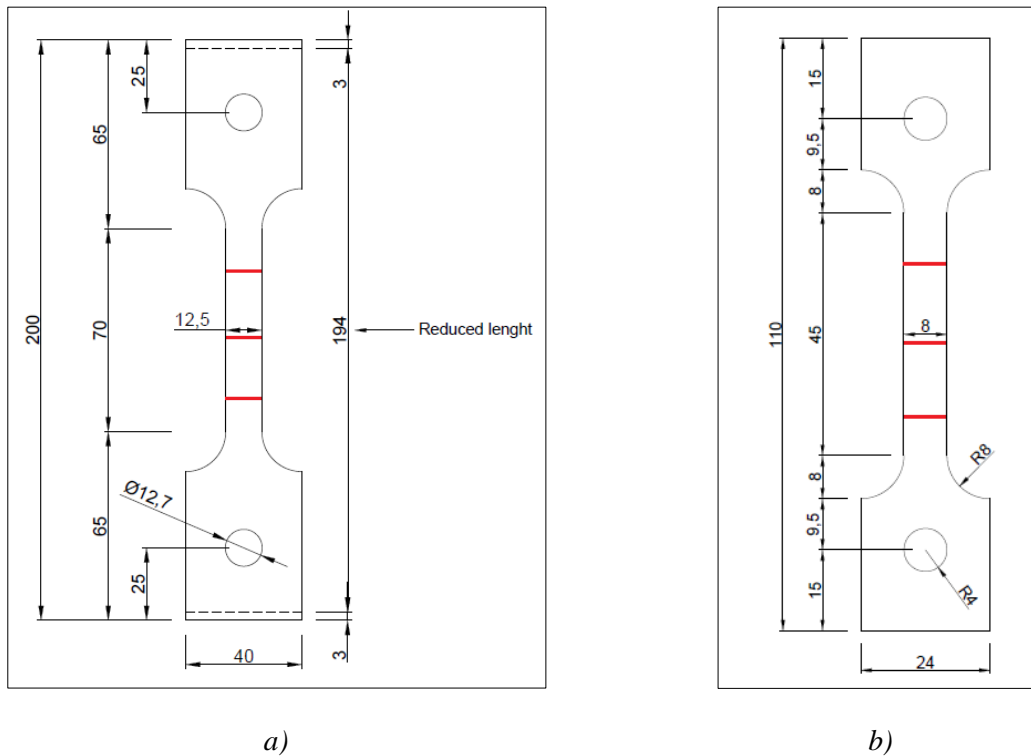


Figure 6-2: Tensile test specimens. a) UT200 and b) UT110

Tests were performed in three directions to determine any anisotropy in the base material (top flange of the profiles); 0° , 45° and 90° relative to the extrusion direction. In addition, tests were performed on the material in the stiffeners. The specimens were cut out from the web, since the flanges are very slim. Three tests were run in each direction and in the stiffeners with a loading rate of 1.35 mm/min . To investigate the effect of the friction stir weld (FSW), three tests were performed on the friction stir weld with a loading rate of 2.1 mm/min . Figure 6-3 shows where the specimens were cut out from the plate, UT110 in the base material and in the web, and UT200 over the weld. UT200 needed a reduced length to fit between the stiffeners. The gauge length, L_0 , is important in the calculations to find the stress-strain relationship and is defined as the uniform part of the specimen, see Figure 6-2. When an extensometer is used, the length of the extensometer is used as L_0 , here 35 mm for UT110 and 57.5 mm for UT200.

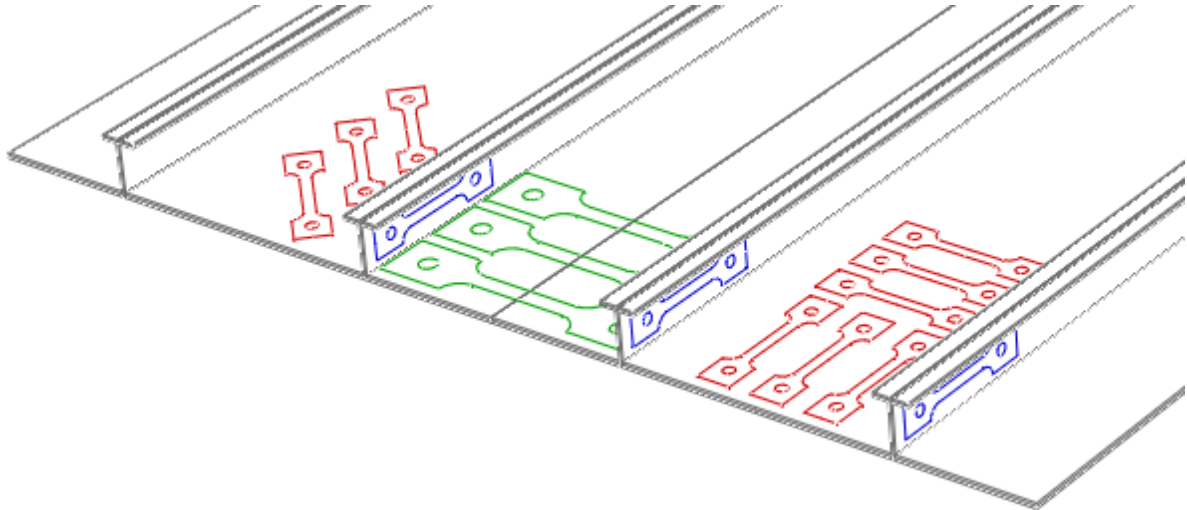
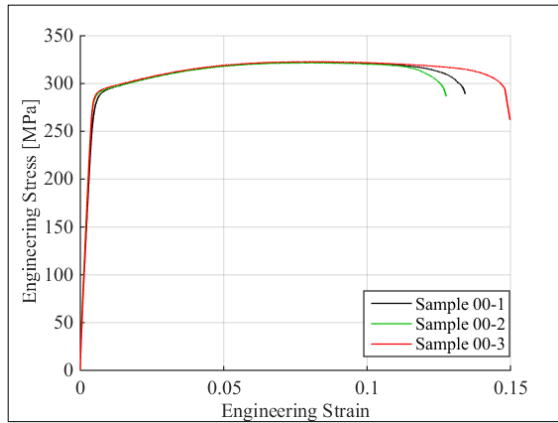


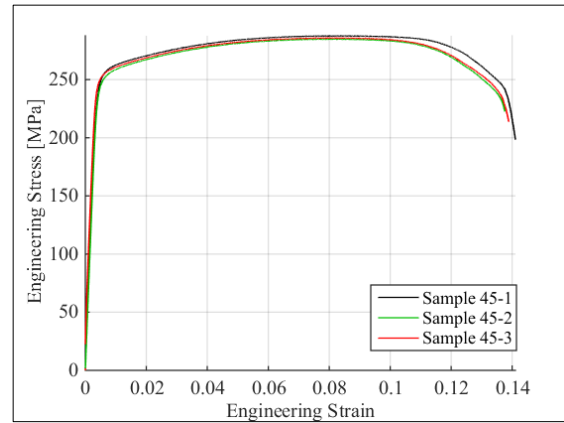
Figure 6-3: Test specimens on the plate. Base material in three directions (red UT110), stiffener material (blue UT110) and FSW (green UT200)

6.2 Experimental Results

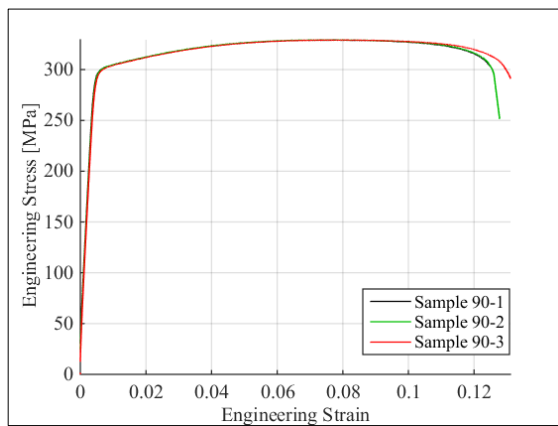
The tensile tests were performed in three different directions in the top flange, and in the web of the stiffeners and over the weld, with three specimens for each area. To extract the force and displacement from the tests, both an extensometer and DIC was used. Figure 6-4 shows the engineering stress-strain curves for all the specimens in each direction, for the web in the stiffeners (WEB) and the friction stir weld (FSW). All the stress-strain curves shown here were found using the measurements from the extensometer.



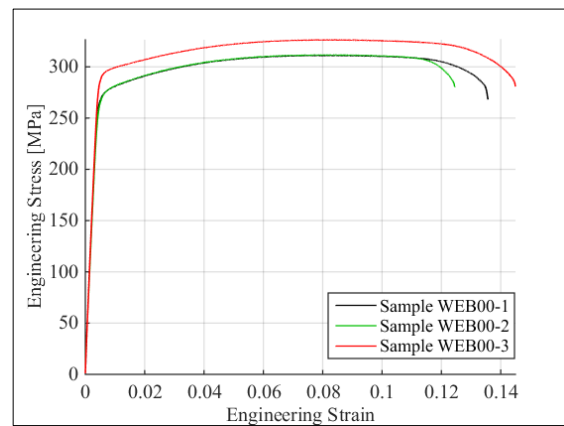
a)



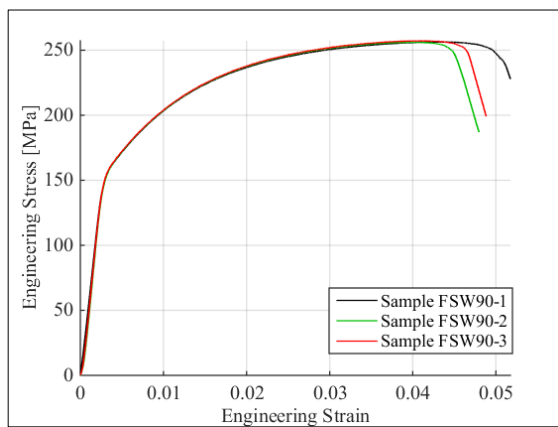
b)



c)



d)



e)

Figure 6-4: Engineering stress-strain curves for specimens in all directions, for WEB and for FSW. a) in 0°, b) in 45°, c) in 90°, d) in the web of the stiffener and d) FSW in 90°

6 Tensile Tests

In the base material and the stiffeners, a low degree of hardening was noticed. This is as expected for this aluminium alloy with temper T6, AA6082-T6. There is a noticeable deviation of the sample WEB00-3 compared to the other samples in the web of the stiffener. This deviation could be explained by that the material samples were extracted from different stiffeners. One representative specimen was chosen in each direction and Figure 6-5 shows the true and engineering stress-strain curves for the representative specimens.

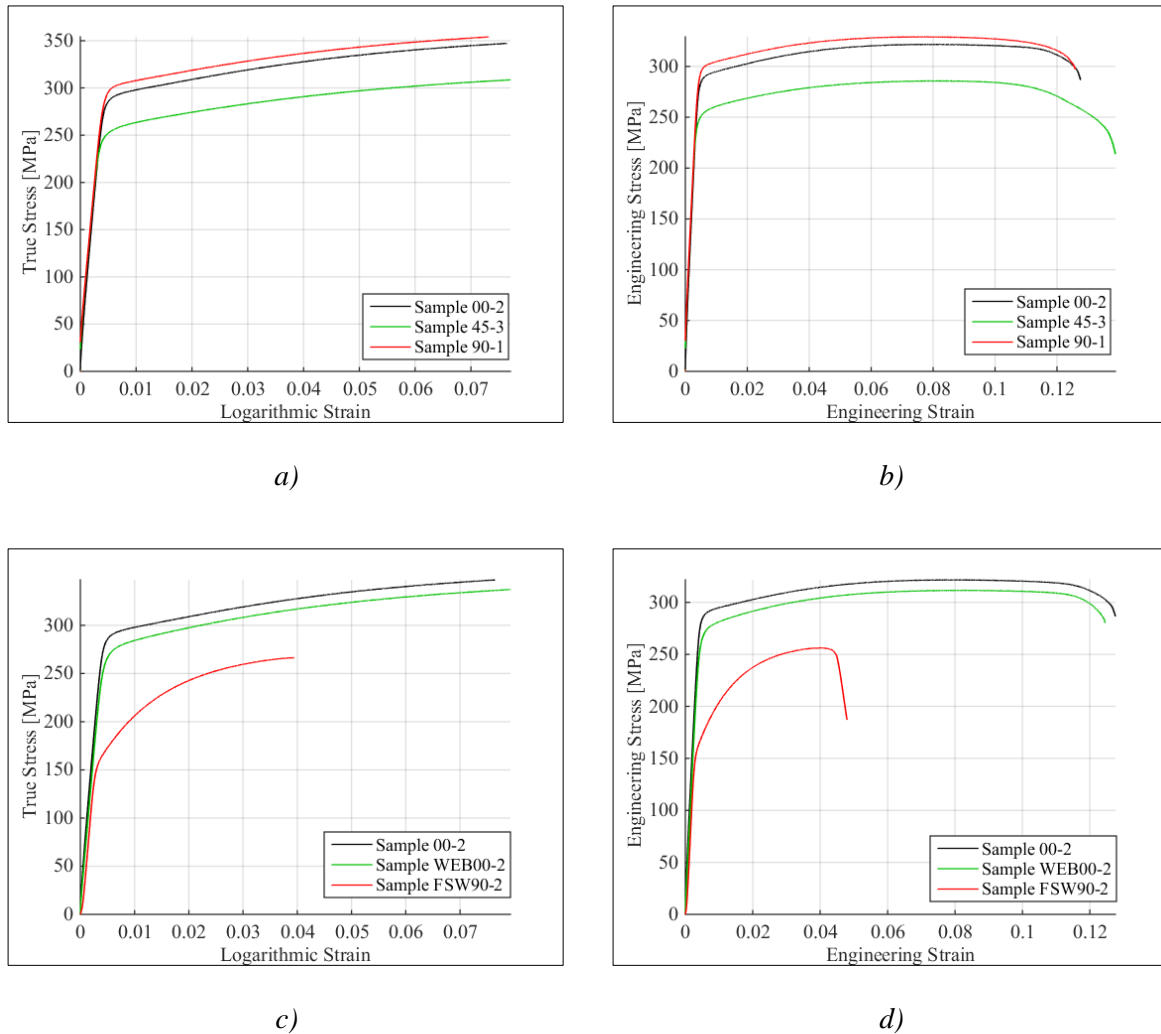


Figure 6-5: Engineering and true stress-strain curves for representative samples. a) and b) True and engineering stress-strain curve for representative samples in base material, c) and d) true and engineering stress-strain curve for representative sample in web of stiffener and FSW compared to base material,

From Figure 6-5 a) and b) it is clear that Young's modulus is approximately equal in all the directions relative to the extrusion direction. The yield stress differed in all directions, with 90% for the 45° direction and 107% for the 90° direction relative to the yield stress in the extrusion direction. From the engineering stress-strain curves in Figure 6-5, the specimens in

the 45° direction seem to be more ductile than the 0° and the 90° direction. The data from the DIC measurements were used to study the strains in the specimens as they reached necking. Figure 6-6 shows the principal strains in the representative specimens in the elastic area, before necking and after necking. From these DIC principal strain field maps, it is also clear that the 45° direction specimen is more ductile than the 0° and the 90° direction, as it has more developed necking before fracture.

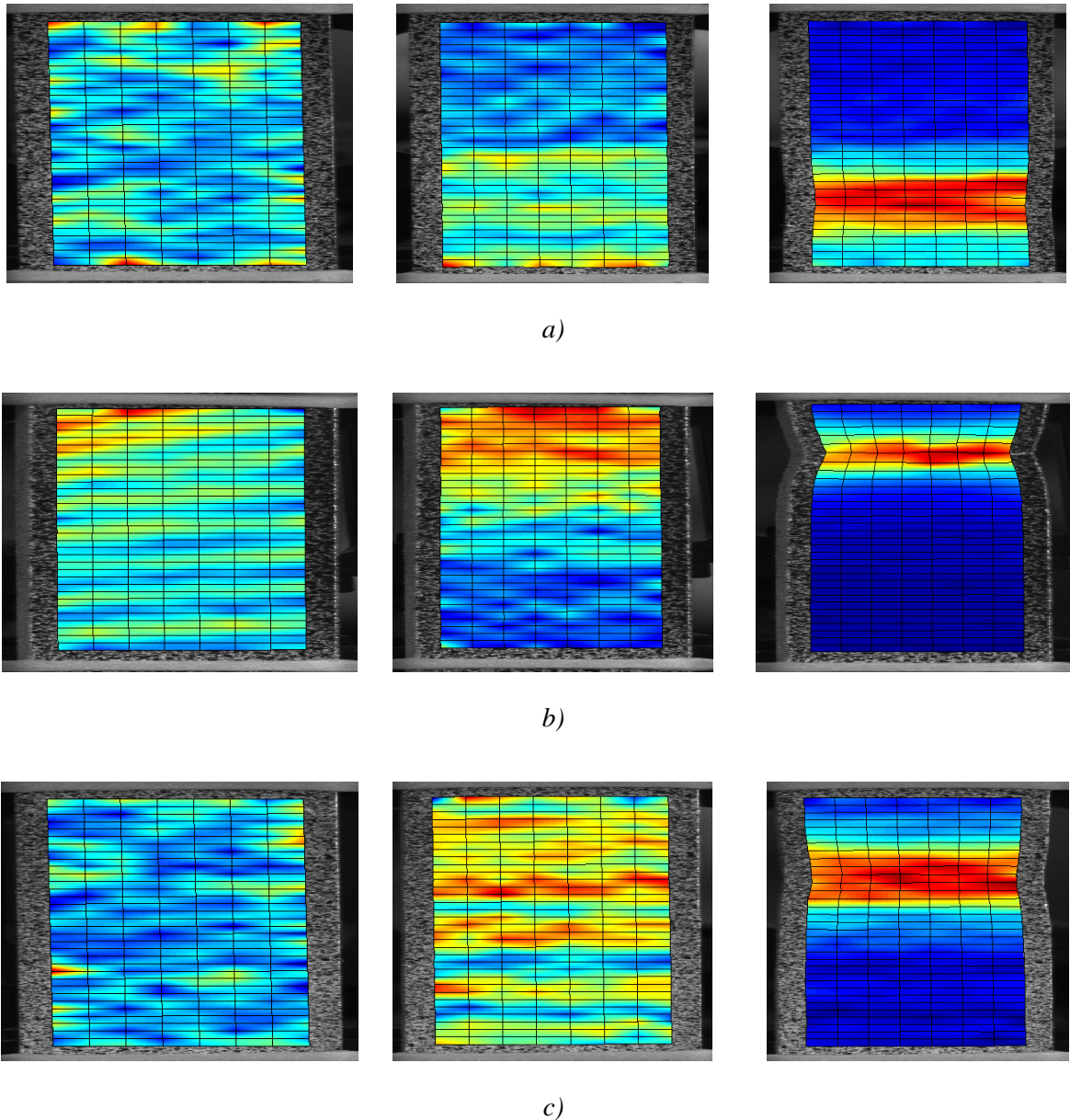


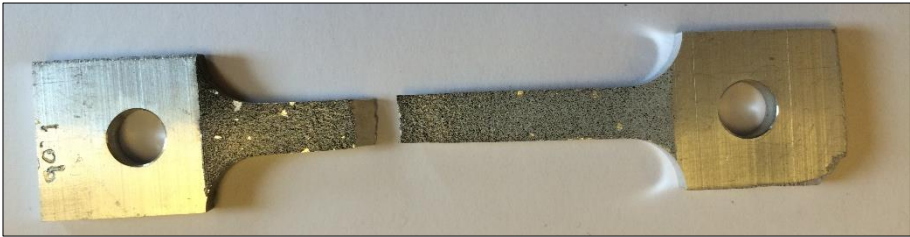
Figure 6-6: Principal strain field maps in all directions of base material a) 0° , b) 45° and c) 90°



a)



b)



c)

Figure 6-7: Fracture in representative samples a) 0°, b) 45° and c) 90°

Figure 6-7 shows the fracture in the representative samples from the tensile test. When studying the fracture surface, it is noticed that direction 0° and 90° has a clear shear fracture surface, while the 45° resembles more a cup and cone fracture surface (see section 2.6.1.1). This is also an indication that the 45° sample is more ductile than the other two samples.

6.2.1 Flow stress ratio and R-ratio

The specific plastic work W_p and the flow stress ratio r_α (2.1.1) has been computed for representative tests in each direction, shown in Figure 6-8a) and b), respectively. The average values of the flow stress ratio for the representative test is given in Table 6-3. From this, it is clear that the material is slightly more anisotropic in the 45° direction than expected from the results of Chen et al. (2009) (Table 2-1) and Wang (2006) (Table 2-2).

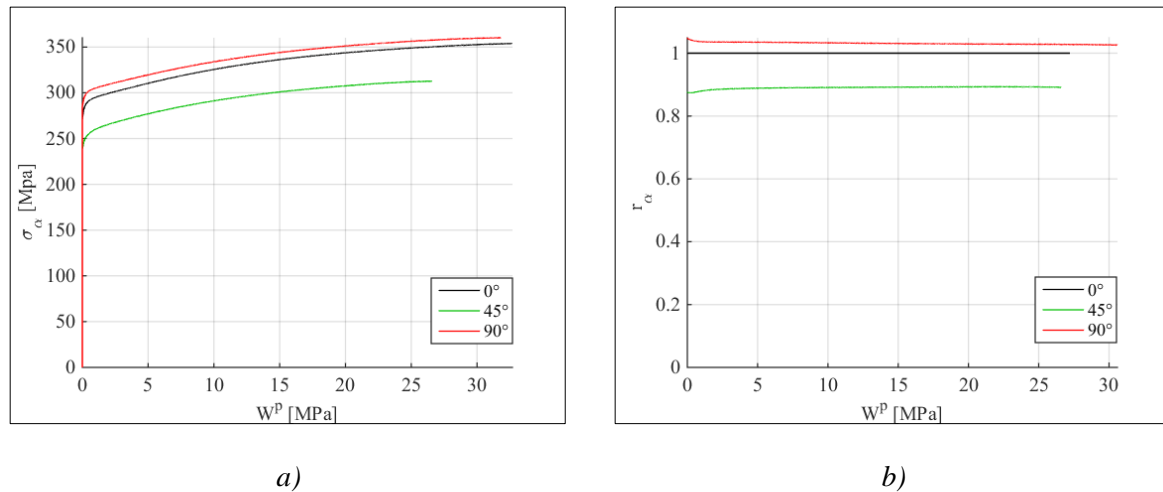


Figure 6-8: Representative results for a) the specific plastic work and b) the flow stress ratio

Table 6-3: Flow stress ratio for representative test

r_0	r_{45}	r_{90}
1.0	0.8896	1.0319

DIC was used to calculate the R-ratio in the three directions. Vector elongation in the length and width direction was used to calculate ϵ_w^p and ϵ_t^p , which resulted in the R-values shown in Figure 6-9. As mentioned in section 2.1.1.1, the material is said to exhibit isotropic flow properties when $R_\alpha = 1$. This implies that the base material is not isotropic, see Table 6-4.

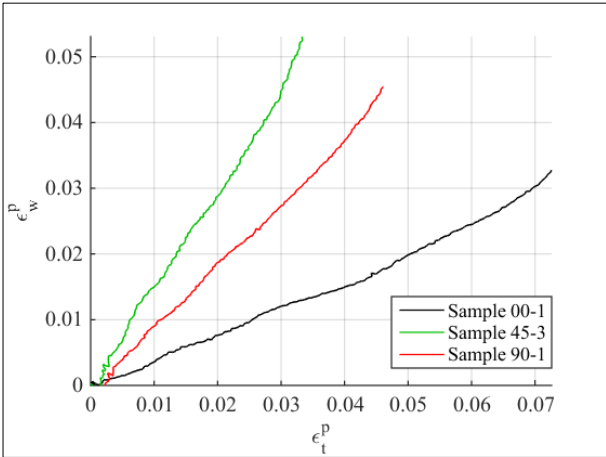


Figure 6-9: R-ratio for material samples in all direction

Table 6-4: R-ratio for material samples

Direction	0°	45°	90°
R_α	0.4185	1.5362	0.9815

The R-ratio was also calculated for the material sample taken from the web in the stiffener. There, the R-ratio was calculated to be $R_{WEB02} = 0.4736$, which is in the same range of anisotropy as the base material in the extrusion direction.

6.3 Identification of Material Parameters

The representative material sample in the extrusion direction gave the material parameters shown in Table 6-5. This shows that the material in the representative samples of the base material in the top flange, and the stiffener material has a lower Young’s Modulus, higher yield stress and higher ultimate stress than the expected values provided by Sapa (Table 6-2). There is also a noticeable difference for the parameters in the stiffeners and the FSW as they exhibit lower Young’s modulus, yield stress and ultimate stress than the base material in the top flange.

Table 6-5: Material parameters for representative samples of the base material (00-2), the web of the stiffeners (WEB00-2) and of the FSW (FSW90-2).

	Young's Modulus	Yield stress	Ultimate stress
	E [MPa]	σ_0 [MPa]	σ_u [MPa]
Base material	66000	271.50	347.32
Stiffener material	63000	238.70	311.69
FSW	60000	150.00	256.19

6.3.1 Numerical Modeling of Tensile Test

The UT110 tensile test specimens were implemented as one solid part into Abaqus/Implicit, with the bolt, which is used to apply the force, as a discrete rigid part. To save computational time, only one eighth of the UT110 was modelled with symmetry axes in all directions, see Figure 6-10.

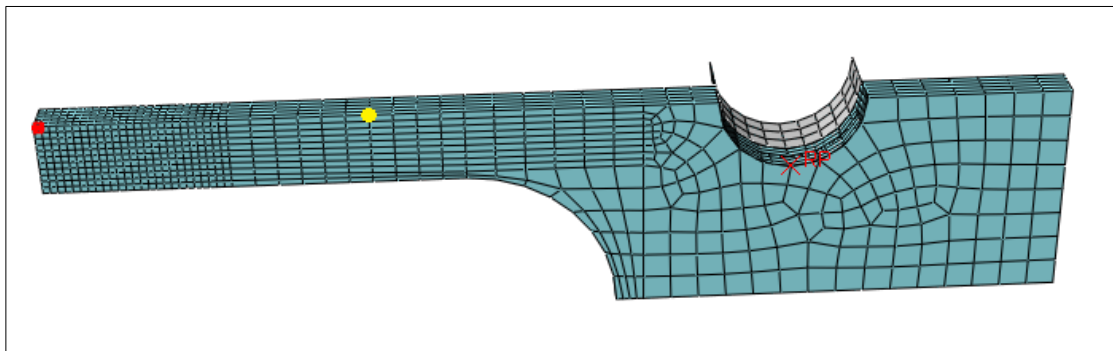


Figure 6-10: Abaqus/Implicit model of UT110 tensile specimen

The model was meshed with five elements in the thickness and smaller elements around the middle of the specimen, as the fracture is intended to occur there. The engineering strain was found by measuring the displacement of a node (marked yellow) with corresponding placement to the extensometer in the tensile test and dividing this by half the length of the extensometer. To calculate the engineering stress, the applied force in the reference point of the discrete rigid bolt (red RP marked in Figure 6-10) was measured and divided by an eighth of the cross-sectional area. The engineering stress-strain curve from the simulation was then compared to the curve from the experiment to find the corresponding strain at fracture. The equivalent plastic strain

and the maximum principal stress was taken from the most exposed element, the element that is located in the middle of the cross-section, marked with red in Figure 6-10 on the far left.

The following section, on modelling of the FSW material test, was made with direct assistance from Postdoc. David Morin at SIMLab, NTNU. The UT200 tensile test specimen that was used in the material test of the FSW was implemented in Abaqus/Implicit as a shell element model. To save computational time, only one quarter of the UT200 was modelled with two symmetry planes (Figure 6-11).

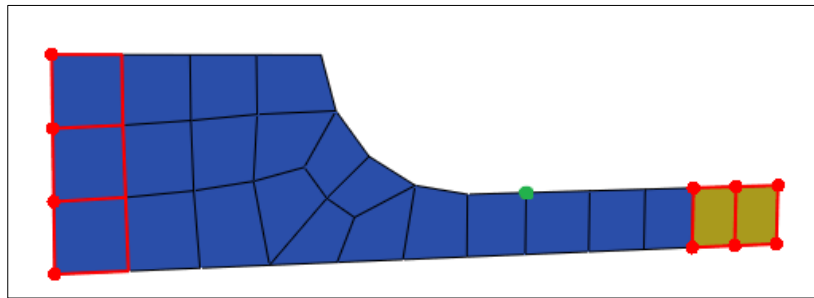


Figure 6-11: Abaqus/Implicit shell model of UT200 tensile specimen

The FSW is represented by a zone of 20 mm (yellow area in Figure 6-11), which is slightly larger than the dimension of the FSW on the specimen, but it is assumed that the HAZ extends beyond the visible weld (section 2.2). The mesh size is equal to half the width of the specimen, 6.25 mm. The engineering strain was found in the same way as for UT110, by the displacement in the node marked green in Figure 6-11. To calculate the engineering stress, the applied force in the red nodes on the left side was summed and divided by a quarter of the cross-sectional area. The equivalent plastic strain and the maximum principal stress was taken from the most exposed element, the element located in the far right of Figure 6-11.

6.3.2 Base Material

To be able to implement the material into the Abaqus/Explicit model of the plate, several material factors had to be identified. First, a curve-fitting tool in Matlab was used to fit the power law and the Voce rule to the plastic region of the true stress-strain curve for the representative samples 00-2 and WEB00-2, by the theory in section 2.4.3. To fit the power law curve, the formulation given in equations 2-52 and 2-53 were used. This formulation of the power law was decided to use for the Cockcroft-Latham fracture criterion as well to reduce the amount of parameters used. The parameters from Voce rule was optimized by comparing the engineering stress-strain curve from the experiment and the analysis in Abaqus/Implicit and changing the parameters, the direct calibrated curve versus the optimized curve is shown in

Figure 6-13. The test specimens for the stiffeners was cut out from the web, but it is assumed that they represent the material in the entire stiffener.

Table 6-6: Power law parameters for sample 00-2 and WEB00-2

	σ_0 [MPa]	K [MPa]	n
Base material	271.5	439.7	0.09129
Stiffener material	238.7	421.6	0.08584

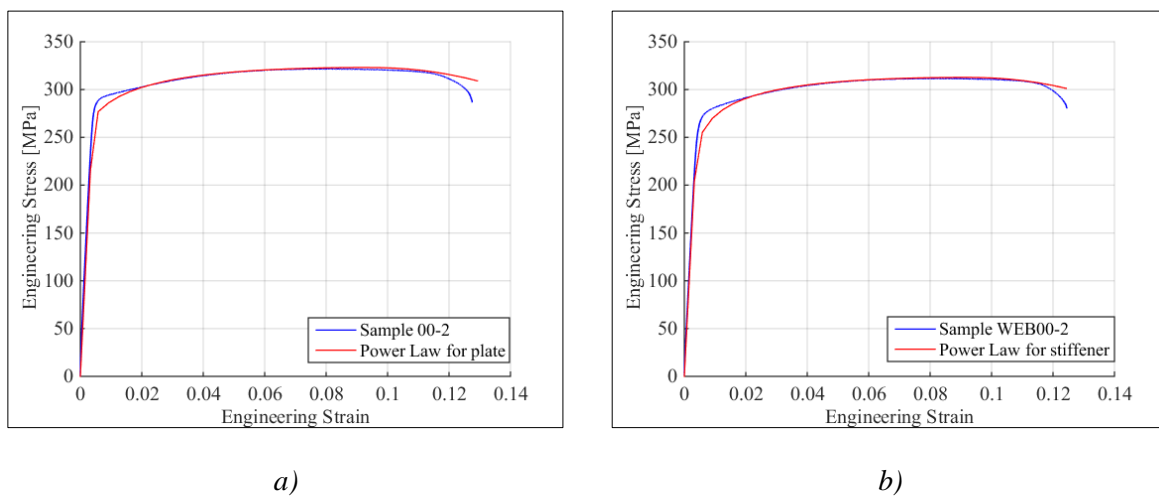


Figure 6-12: The power law versus the engineering stress strain curve for a) the base material and b) the stiffener material

Table 6-7: Voce rule parameters for sample 00-2 and WEB00-2

	σ_0 [MPa]	Q_{R1} [MPa]	C_{R1}	Q_{R2} [MPa]	C_{R2}
Base material					
Direct calibration	271.5	17.78	2058	77.69	19.43
Optimized values	271.5	17.78	2058	90.00	15.00
Stiffener material					
Direct calibration	238.7	36.65	1727	76.25	22.52
Optimized values	238.7	36.65	1727	86.00	17.00

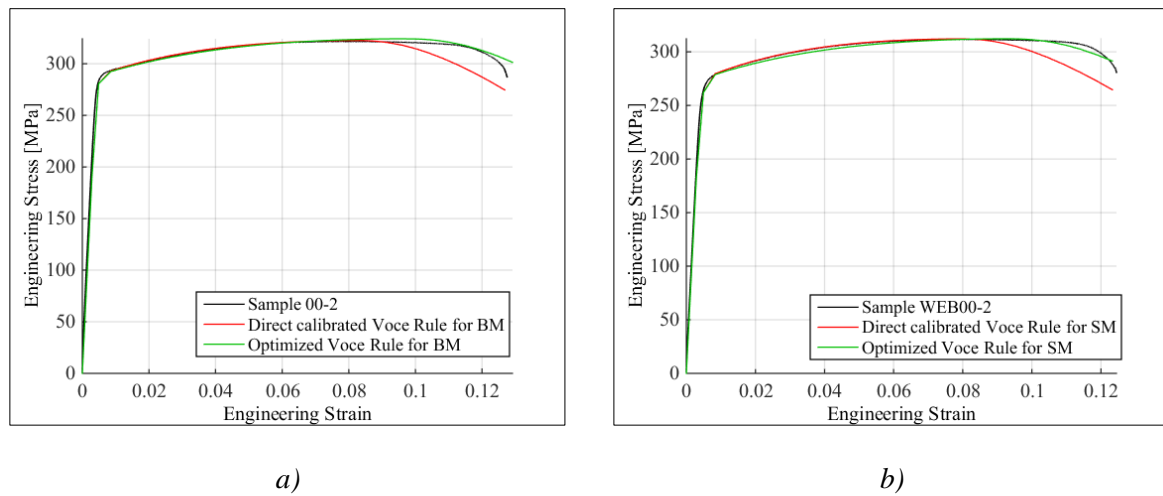


Figure 6-13: Direct calibration versus optimized Voce rule for a) base material (BM) and b) for stiffener material (SM)

The power law and Voce rule parameters will be used when implementing the Cockcroft-Latham fracture criterion into Abaqus/Explicit. To find the Cockcroft-Latham parameter, W_c , the plastic work under the equivalent plastic strain and the maximum principal stress curve for the most exposed element was calculated. The Cockcroft-Latham parameter for the power law and Voce rule is shown in Table 6-8. The power law parameters will also be used when implementing the BWH instability criterion into Abaqus/Explicit.

Table 6-8: Cockcroft-Latham parameter for power law and Voce rule

	power law, W_c [MPa]	Voce rule, W_c [MPa]
Base material	117.6938	107.12
Stiffener material	101.3674	94.95

6.3.3 Friction Stir Welds

The following section was produced with direct assistance from Postdoc. David Morin at SIMLab, NTNU. The material parameter for the friction stir welds were found in the same manner as for the base material. The direct calibrated power law parameters in Table 6-9 are in compliance with equation 2-52 and 2-53. Figure 6-14 shows the difference in the engineering stress-strain curve for the direct calibrated power law and the optimized power law.

Table 6-9: power law parameters for sample FSW00-2

	σ_0	K	n	W_c
Direct calibration	150	300	0.10	-
Optimized values	150	420	0.18	34.49

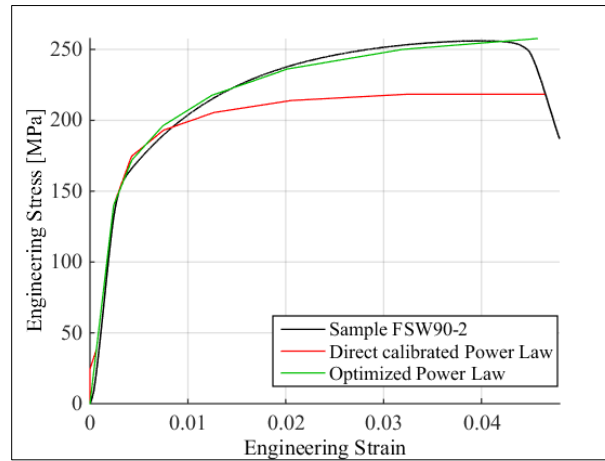


Figure 6-14: Direct calibrated power law compared to the optimized power law

6.4 Discussion and Revision of Preliminary Model

The preliminary model was revised after performing the material tests by making material cards for the Cockcroft-Latham fracture criterion with both the power law and Voce rule, and the BWH instability criterion with the power law. A Poisson ratio of 0.33 was used in all material cards. These material cards will be implemented in Abaqus/Explicit and the model will be run with the SIMLab Metal Model. The material cards are shown in appendix E.2-E.4.

In the material tests, a more ductile behaviour was detected in the 45° direction than the 0° and 90° direction. A similar behaviour was found for the alloy AA7075-T651 in Fourmeau et al.'s (2013) study on anisotropic failure modes of high-strength aluminium under various stress states. In the article they detected that for this alloy, the 45° exhibits larger strains than the 0° and 90° directions, and for larger strains the fracture mode changed from shear fracture in 0° and 90° to cup and cone fracture in 45° (Fourmeau et al., 2013).

6 Tensile Tests

The material in the web of the stiffeners were also tested. The material was taken from different stiffeners and showed both higher and lower yield and ultimate strength than the base material in the top flange, see Figure 6-15. Since there is an uncertainty of the material properties in the web of the stiffeners, it was decided to consider the most conservative option, i.e. the weakest stiffener (WEB00-2).

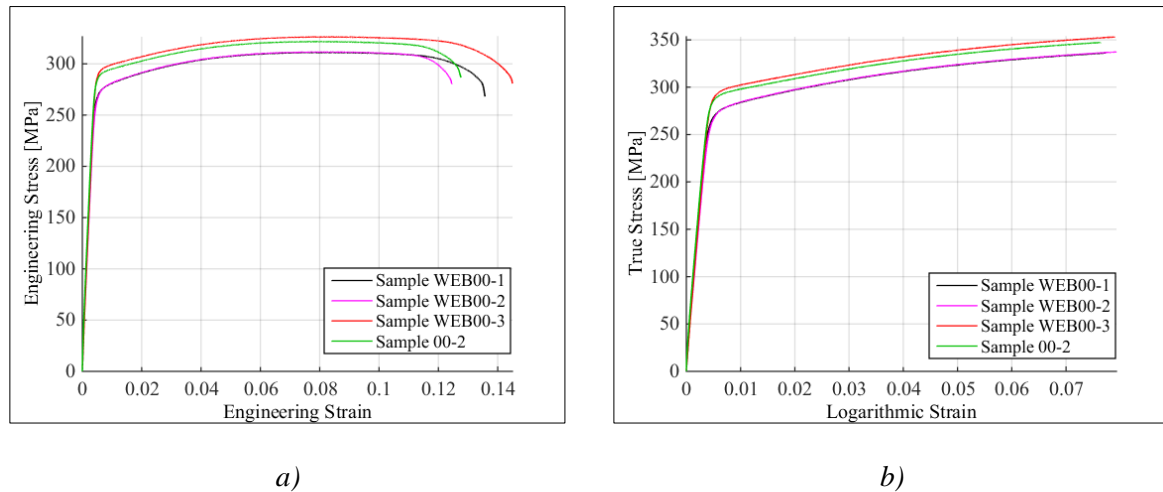


Figure 6-15: Stiffener material compared with base material. a) Engineering stress-strain curves and b) true stress-strain curves

There may be several reasons for the differences in material properties between the material in the top flange and in the stiffeners. The degree of recrystallization might be different for the top flange and the stiffener, so the top flange will most likely have a coarser structure than the stiffeners and it is more likely to have a more fibrous structure. The degree of cooling in the top flange and the stiffener is also different, as the cooling in the stiffener is worse than the top flange, since it is difficult to achieve direct cooling water spray on the web.

Since the flange of the stiffener is very slim the material tests were only taken from the web, and it was assumed that the flange exhibited the same material properties as the web of the stiffener. In Hildrum's (2002) Dr. Ing. thesis, she performed material tests both in the web and in the flange of the stiffeners and found lower values for $\sigma_{0.2}$ and σ_u in the flange than in the web (Hildrum, 2002). Since Hildrum tested the same aluminium alloy with the same temper as in this master thesis, it is reason to believe that the assumption that the flange exhibits the same material properties as the web is inaccurate and can affect the accuracy of the numerical simulations. In section 8.1 the difference in numerical results of using the same material for the whole plate and a separate material in the stiffeners will be discussed.

In the numerical simulation of the tensile test specimen UT200 over the weld, there was no plastic strain in the base material, see Figure 6-16. This indicates that the power law which was optimized for the FSW is independent of the base material. When running numerical analyses of the plate it is important to check that the plastic strain is not higher than approximately $\varepsilon^p = 0.04$, since the power law is not approximate after necking (Figure 6-14)

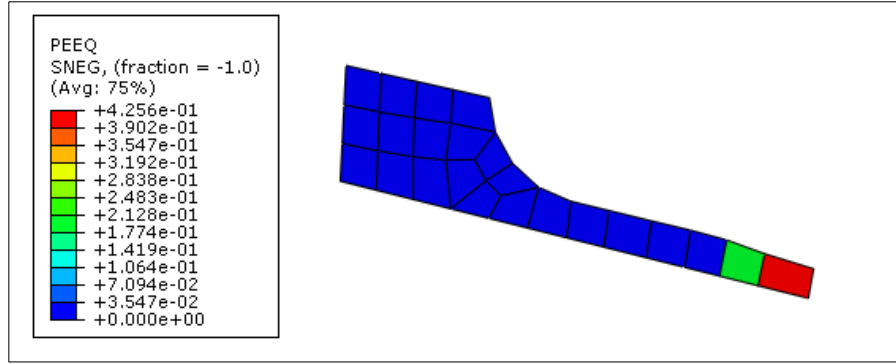


Figure 6-16: Equivalent plastic strain (PEEQ) in the numerical simulation of the UT200 specimen over the weld.

A stronger anisotropy than expected was detected for the aluminium alloy AA6082-T6. The yield stresses differed in all the directions relative to the extrusion direction. With a R-ratio of $R_0 = 0.4185$ in the extrusion direction and flow stress ratios varying from $r_{45} = 0.8896$ to $r_{90} = 1.0319$. This gives reason to believe that an isotropic assumption with a von Mises yield criterion will give numerical results which deviates from the experimental results. It could therefore be interesting to look at the Hershey yield criterion, which resembles an anisotropic yield criterion. The Hershey criterion gives a yield surface which lies in-between the Tresca and von Mises yield surfaces (described in section 2.4.2.1), and is given by equation 6-1. The curvature of the yield surface is determined by $m \geq 1$, and since aluminium is a face-centered cubic (see section 2.1), $m = 8$ (Hopperstad and Børvik, 2013). In section 8.1, the Hershey criterion will be implemented with the Cockcroft-Latham fracture criterion in Abaqus/Explicit and compared to the von Mises yield criterion with the same fracture criterion.

$$f(\sigma_1, \sigma_2, \sigma_3) = \left(\frac{1}{2} (|\sigma_1 - \sigma_2|^m + |\sigma_2 - \sigma_3|^m + |\sigma_3 - \sigma_1|^m) \right)^{\frac{1}{m}} - \sigma_Y = 0 \quad 6-1$$

7 Component Tests

Sapa delivered eight aluminium plates of alloy AA6082 and temper T6. A stiffener and a friction stir weld are displayed in Figure 7-1. In the component test, two different types of tests were performed: Quasi-static and dynamic. In both tests, the indenter which was chosen in section 5.2.2 have been used, the real indenter and the simulated indenter are displayed in Figure 7-2. In this section, the results from both tests will be presented. Out of the eight plates, it was decided to do four quasi-static tests and four dynamic tests, with the indenter in both directions.

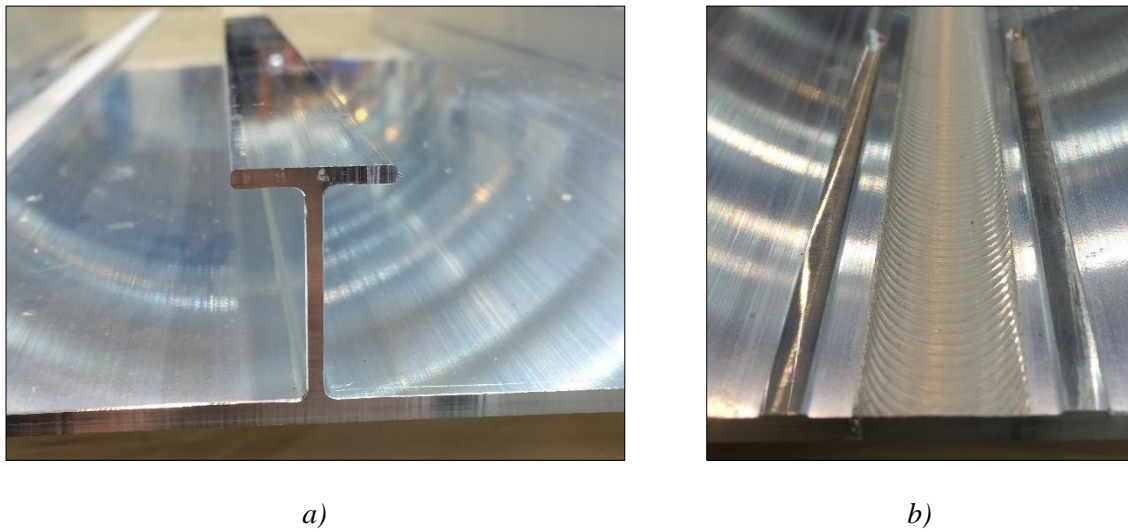


Figure 7-1: Plates delivered by Sapa . a) stiffener and b) friction stir weld where the “lips” are milled away.

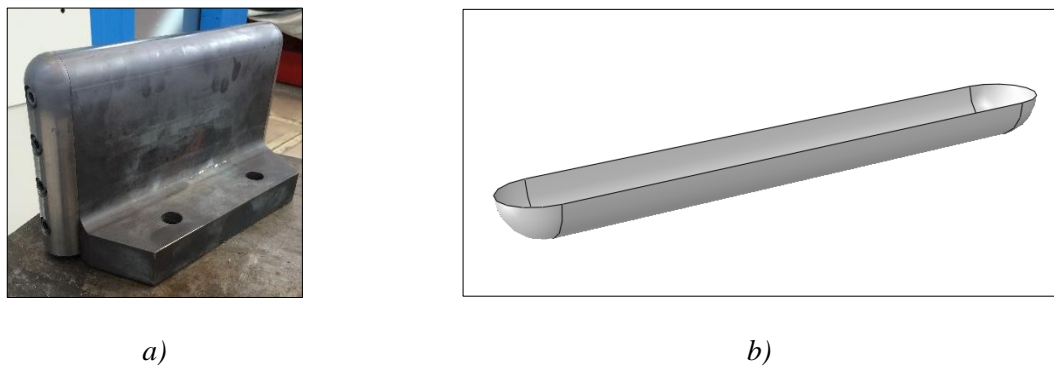


Figure 7-2: Cylindrical indenter with rounded edges. a) indenter shape in experiments and b) indenter shape in Abaqus

7.1 Quasi-Static Test

In the quasi-static test, the rig that has been designed was placed on the support shown in section 4.2. The geometry of both the plate and the rig is shown in section 4.4.5. The whole set-up is shown in Figure 7-3, with the quasi-static support, the rig with the plate, and the machine and indenter. The force was applied gradually, with a velocity of 10 mm/min, and was stopped right after fracture occurred in the plate. To record the deformation of the plate relative to the rig, a laser was attached to the side of the rig. The laser measures the relative distance up to the slender plank which is visible in Figure 7-3. Two cameras which took one picture per second were placed under the rig. The setup of the plate in rig is shown in Figure 7-4. The plate is placed in the bottom part of the rig before the L-profiles are placed under the plate, and teflon plates over and under the aluminium plate. The last step is to place the top part of the rig and fasten the bolts. After encouragement by postdoctoral Gaute Gruben, the indenter was sprayed with UNIMOLY C 220 spray to lower the friction between the indenter and the plate.



Figure 7-3: Set-up for quasi-static test



Figure 7-4: Setup of the plate in the rig

7.1.1 Experimental Results

Two tests were performed with the transversally placed indenter. Here, one laser was used to measure the displacement of the plate. A small angle was detected in the indenter during last test. Therefore, it was decided to place one more laser on the opposite side of the rig for the remaining tests. The force-displacement plots logged for the transversally placed indenter are shown in Figure 7-5, where QSTE1 and QSTE2 (Quasi-Static Transversal Experiment) are the two specimens in the transversal test. There is good correlation between the two specimens for the transversally placed indenter.

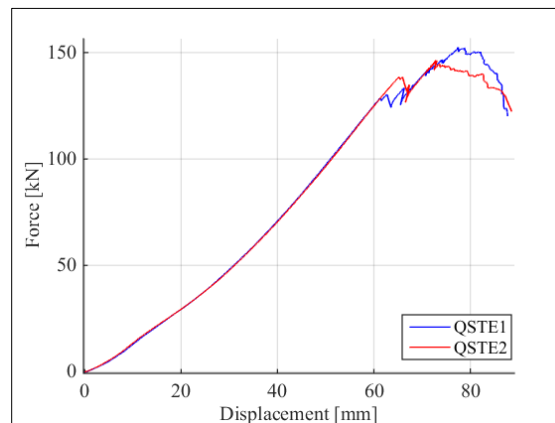


Figure 7-5: Experimental results for the quasi-static test of transversally placed indenter

Fracture occurred first in the flanges of the stiffeners in both QSTE1 and QSTE2, at approximately the same displacement. Shortly after, fracture occurred in the web of the stiffeners and then in the top flange. Unfortunately, the cameras were only able to capture under one end of the indenter, and in both cases fracture first occurred where the cameras were not pointing. Photos of the fracture in QSTE1 and QSTE2 are displayed in Figure 7-6. In QSTE1 (a) fracture only occurred at the ends of the indenter in the plate, while in QSTE2 (b), which was run longer than QSTE1, fracture developed under the whole length of the indenter. In both

plates the fracture propagated away from the welds towards the stiffener. The material in the weld is significantly weaker than the base material, see section 6.2.1, but it is reason to believe that the “lips” makes the area outside the welds stronger so the fracture does not spread towards the welds. In both tests, a plastic deformation of the FSW was noticed.

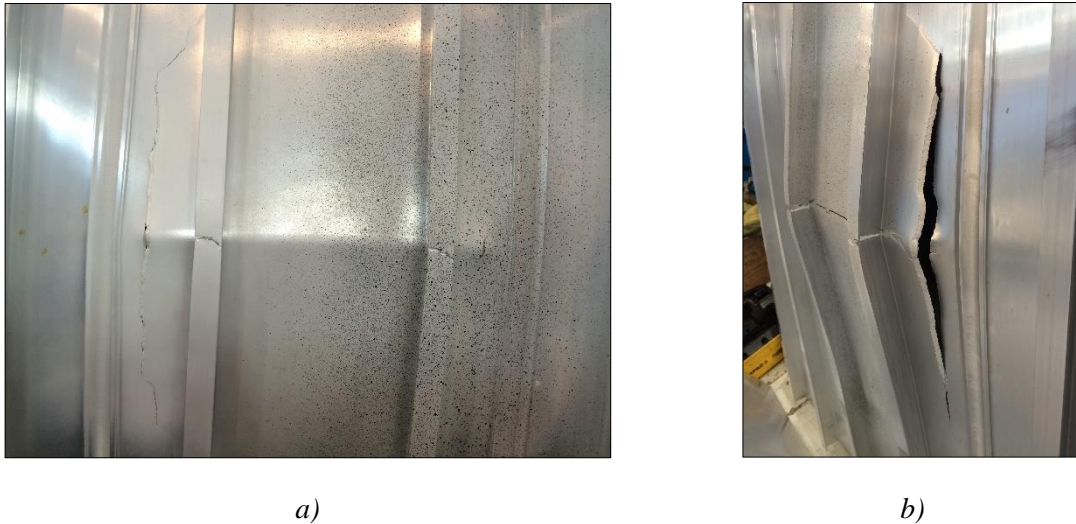


Figure 7-6: Fracture in a) QSTE1 and b) QSTE2.

The flanges in the stiffeners experienced a tensile fracture due to beam bending (Figure 7-6 b) with a visible necking area (Figure 7-7 a). In addition, a “cup and cone” effect appeared in the stiffeners, see Figure 7-7d) (section 2.6.1.1). Due to membrane stresses, shear fracture with inclined fracture planes occurred in the plates, shown in Figure 7-7b) and Figure 7-7c). This may be explained by a through thickness shear instability before fracture. As mentioned, the indenter was somewhat tilted, which lead to fracture initiating on one end of the indenter first. In both experiments, a tendency of local necking was detected around the fracture path, but this was difficult to capture by a camera.

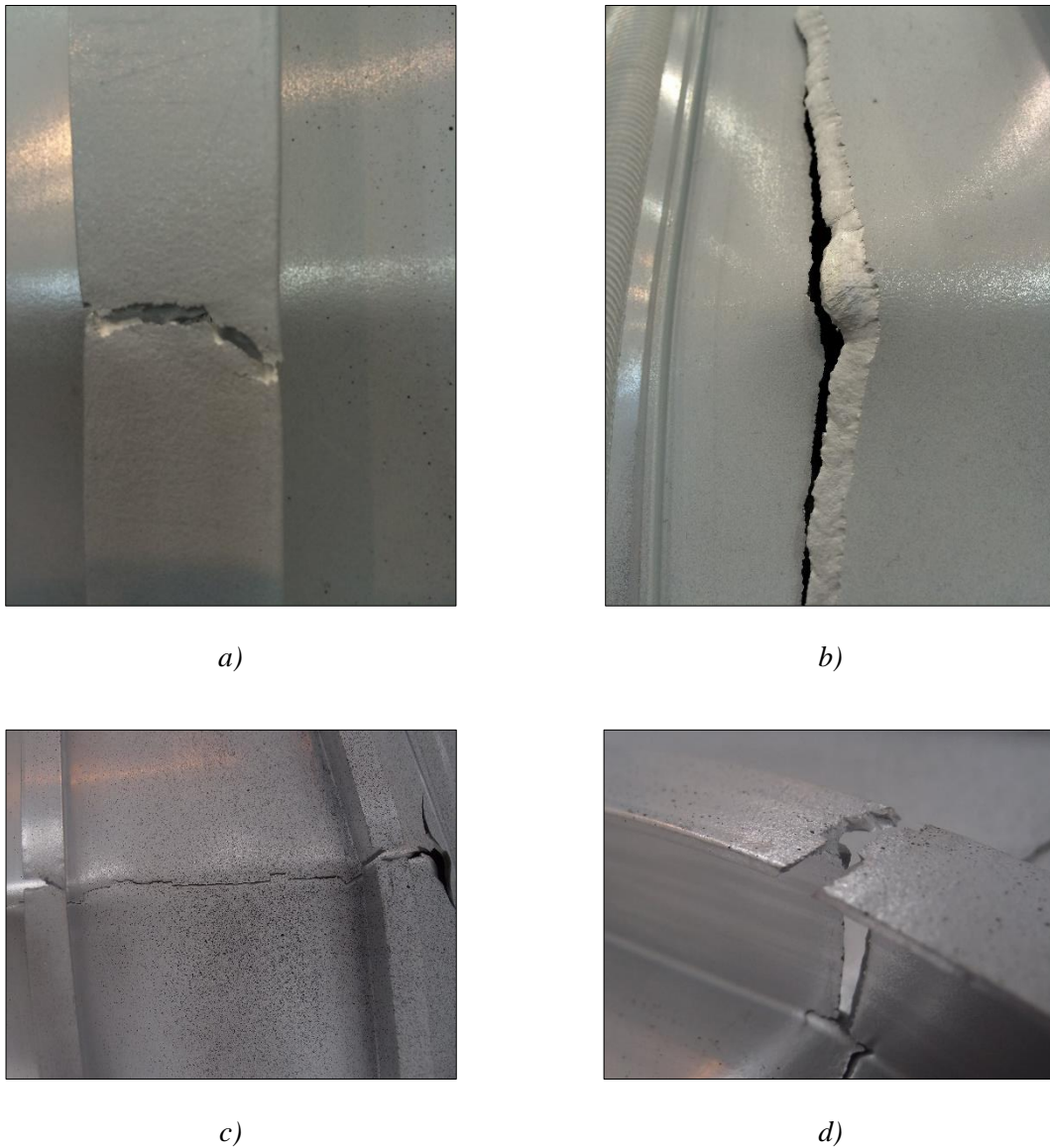


Figure 7-7 a)-d): Fracture in plate with transversally placed indenter. a) QSTE1: Fracture in stiffeners. b) QSTE1: Fracture in plate c) QSTE2: Fracture in plate d) QSTE2: Fracture in stiffener.

For the longitudinal placed indenter, two lasers were used to measure the displacement of the plate to remove a possible effect an angle of the indenter would have. Figure 7-8 shows the force-displacement plots for the two test specimens with a longitudinal placed indenter, QSLE1 and QSLE2 (Quasi-Static Longitudinal Experiment), where the displacement is an average of the displacements logged by the two lasers. There is good correlation between the two tests for the longitudinal placed indenter.

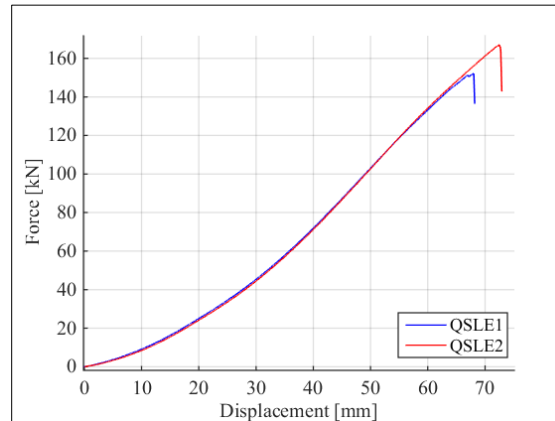


Figure 7-8: Experimental results for quasi-static test of longitudinal placed indenter

Fracture occurred as a ductile fracture due to membrane forces in the plate for both specimens. The force is slightly higher in QSLE2 than in QSLE1, this could be because the set-up process might give different boundary conditions for each experiment. The fracture in the two plates are shown in Figure 7-9. Figure 7-9 a) shows the bottom view of QSLE1 and b) shows the top view of QSLE2. From the photo of QSLE1 (a) it is clear that the stiffeners were almost unaffected by the impact, only a modest twisting of the stiffeners away from the impact is visible. The two photos in Figure 7-10 were taken with one second apart by one of the cameras during the test. In the left photo (a), only a small crack is visible, and in the right photo (b) full fracture have occurred under the whole length of the indenter. Figure 7-11 shows a close up of the fracture of both test specimens. As for the QSLE2, shown in Figure 7-7 c), the plate in the QSLE2 experienced shear fracture with inclined fracture planes (Figure 7-11 a). The right photo (b) shows how the fracture develops with multiple shear planes.

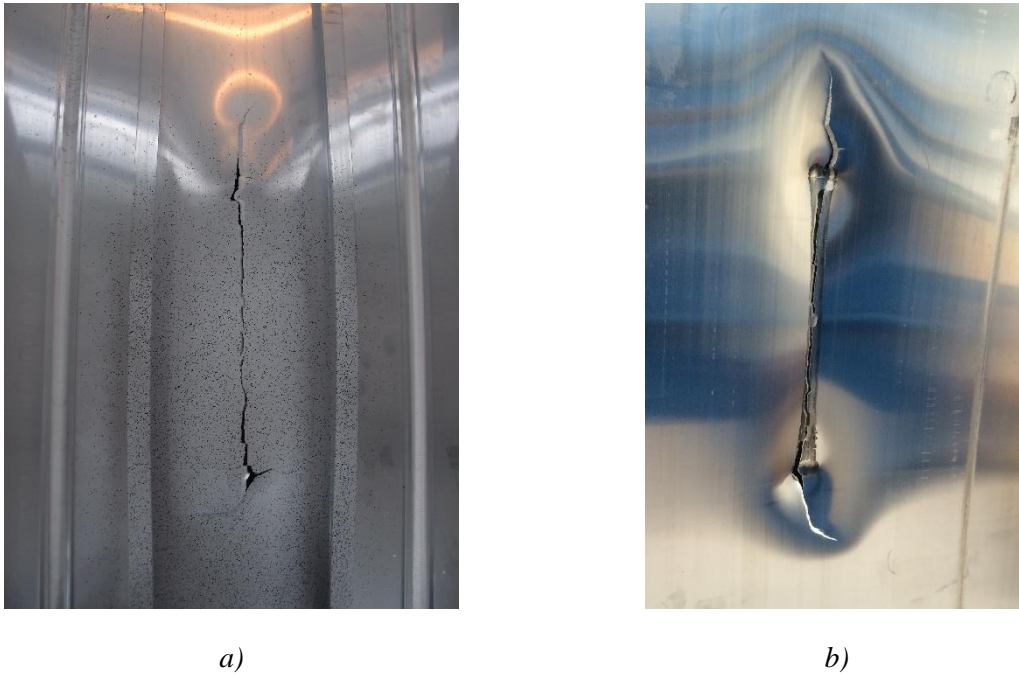


Figure 7-9: a) Fracture in QSLE1 from behind and b) top view of fracture on QSLE2

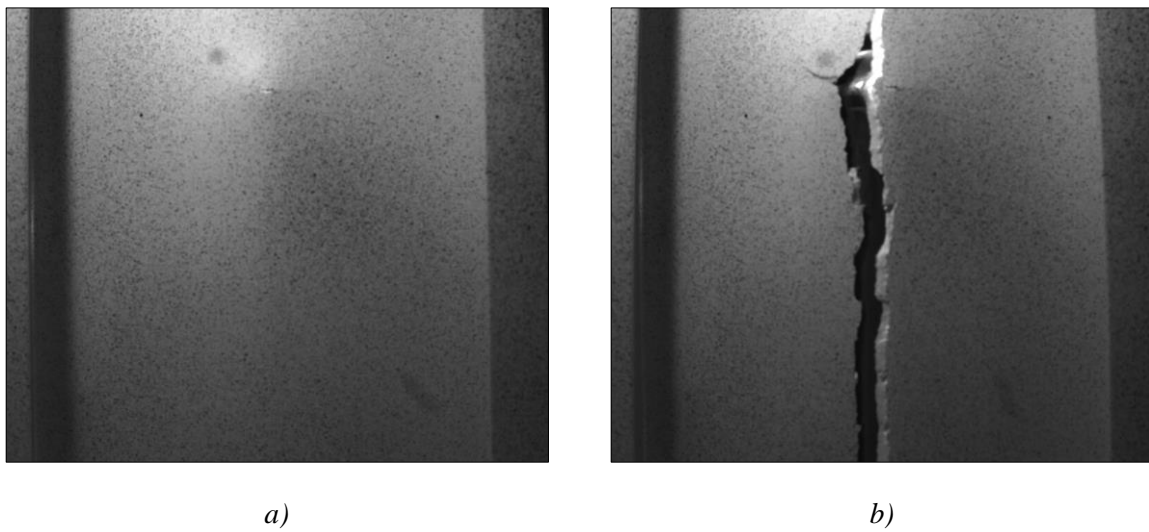


Figure 7-10: Fracture in QSLE2. a) right before fracture and b) right after fracture

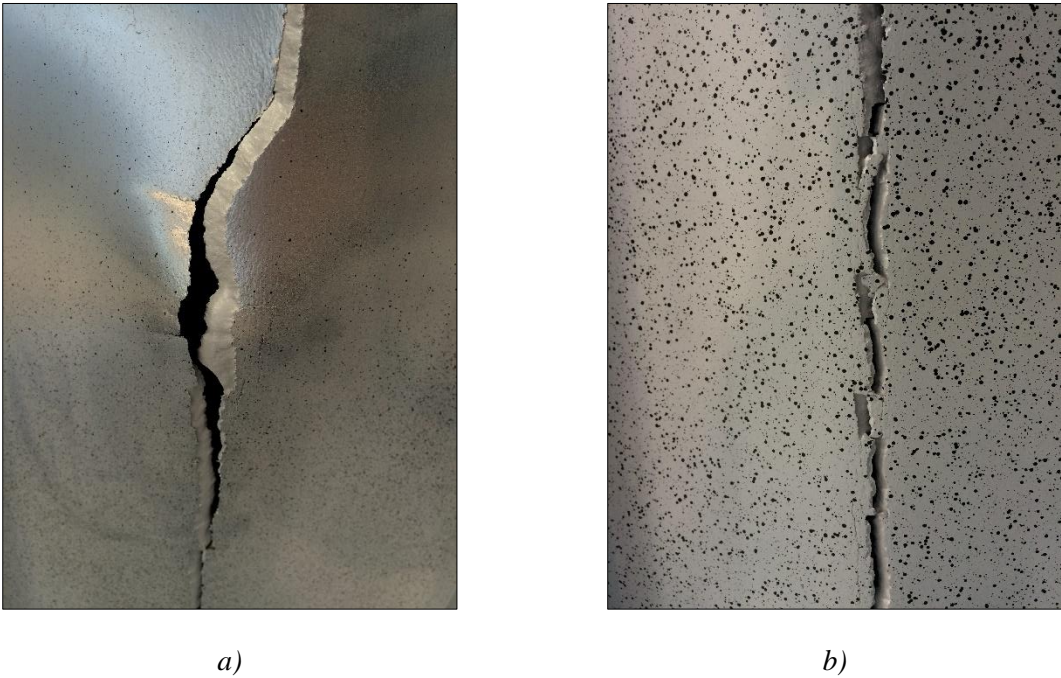


Figure 7-11: Fracture in a) QSLE2 and b) QSLE1

7.2 Energy Calculations

The external work, i.e. the work done by the applied force, is equal to the area under the force-displacement curve, as described in 3.4.1. This work is used to find the kinetic energy ($E_k = \frac{1}{2}mv^2$) needed in the dynamic test to initiate fracture. The impactor in the dynamic tests consist of the indenter and the trolley and has a total weight of 1431 kg. The external work is set equal to the kinetic energy, and thus the necessary velocity of the impactor in the Kicking machine (section 4.1.1) can be found:

Table 7-1: Experimental results – external work and velocity in kicking machine

	External work [J]	Velocity in kicking machine [m/s]
QSTE1	3474.4	2.25
QSTE2	3742.7	2.34
QSLE1	4934.0	2.68
QSLE2	5298.1	2.79

7.3 Dynamic Test

The dynamic tests were performed in the kicking machine (section 4.1.1) at the Structural Impact Laboratory at NTNU, see Figure 7-12 a). The step-by-step setup of the plate and rig in the kicking machine is shown in Figure 7-13. The plates were first placed in the bottom part of the rig (Figure 7-13a) before the L-profiles are placed under the plate (Figure 7-13b), and teflon plates over and under the aluminium plate (Figure 7-13c). Then, the upper part of the rig was placed on top and fastened to the bottom part with bolts (Figure 7-13d). All the different layers are visible in Figure 7-13 e), and Figure 7-13 f) shows the bottom view of the plate in the rig. The whole rig was lifted and placed in the kicking machine (Figure 7-13g), where it is bolted and welded to the receiving wall (Figure 7-13h). The force, displacement and velocity was measured by the load cells in the moving trolley. Two high speed cameras were installed to capture the impact of the indenter on the plate. From these videos, the velocity and the displacement of the indenter was calculated, and used to control the measurements by the load cell. In addition, a small GoPro camera was installed to capture the impact on the plate from behind. Three aluminum RHS profiles were placed on the receiving wall to absorb the remaining energy if the indenter passed through the plate, see Figure 7-12 b). The indenter was mounted on the trolley, displayed in Figure 7-14, and was first adjusted to hit the plate transversally to the stiffeners, and then turned to hit the plate longitudinally to the stiffeners.



a)



b)

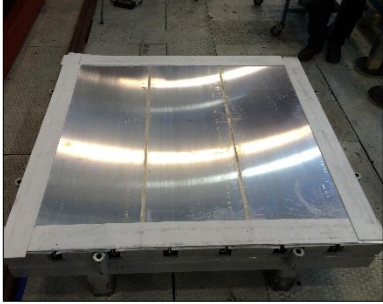
Figure 7-12: a) The kicking machine and the receiving wall and b) the receiving wall



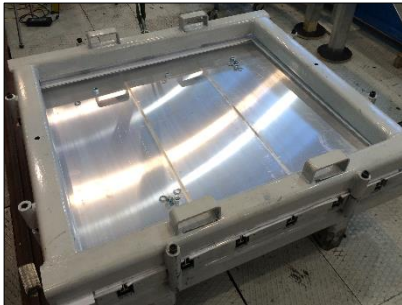
a)



b)



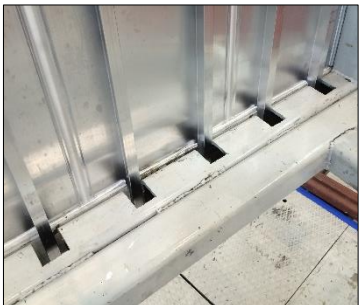
c)



d)



e)



f)



g)



h)

Figure 7-13: Step-by-step illustration of mounting the plate and rig in the kicking machine.



Figure 7-14: Indenter mounted in the transversal direction on the trolley.

7.3.1 Experimental Results

Two tests were performed for each direction of the indenter, starting with the indenter transversal to the stiffeners. The velocities in the experiment was decided on the basis of the energy calculations in section 7.2, but the input velocity in the kicking machine was inaccurate since the velocity of the impactor was at a low range. Figure 7-15 a) shows the force-displacement plots for the first two experiments, DTE1 and DTE2 (Dynamic Transversal Experiment). Figure 7-16 shows pictures from the first experiment DTE1, first with maximum displacement (a) and then the deformed plate after impact (b). This illustrated that there was a lot of elastic energy in the plate. In DTE1 the initial velocity was 2.43 m/s, which resulted in tensile fracture in the stiffeners and a tiny crack on the bottom side of the plate (Figure 7-16 c), and as in the quasi-static test, there was visible necking in the stiffeners. It is clear from Figure 7-15 and Figure 7-16 that there was lot of energy that was not absorbed in the plate, which resulted in a residual velocity of 1.61m/s (Figure 7-15 b). To get fracture in the plate, the initial velocity would have to be much higher than in DTE1, but then the rig and the trolley could have been damaged. Therefore, the initial velocity was only increased to 2.61 m/s, which resulted in approximately the same fracture as in DTE1, except that the crack in the plate was a bit larger and more necking in the stiffeners was detected for DTE2 (Figure 7-16 d).

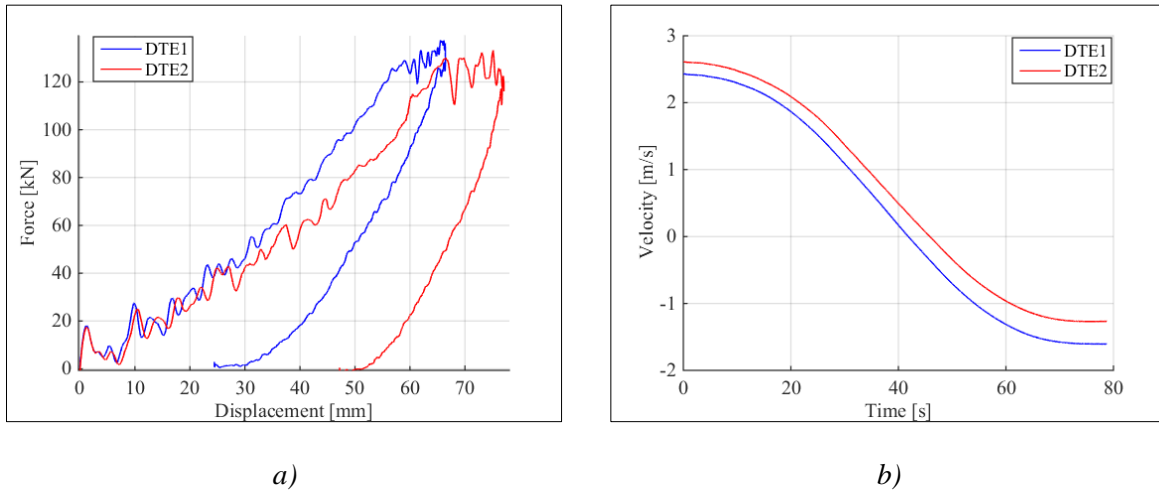


Figure 7-15: Experimental results for DTE1 and DTE2. a) Force-displacement curve and b) velocity-time

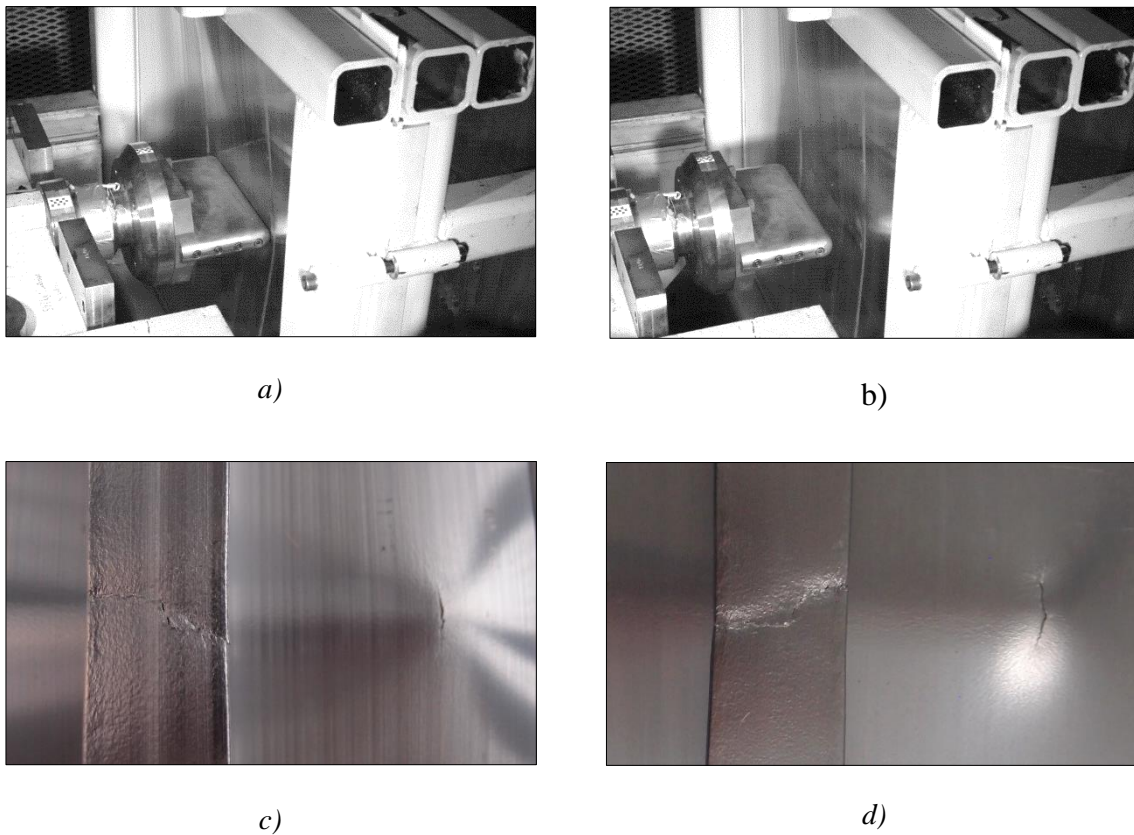


Figure 7-16: a) Maximum displacement in DTE1, b) and deformed plate after impact. Necking in the stiffeners and crack in the plate of c) DTE1 and d) DTE2

For the experiments with the indenter turned longitudinally to the stiffeners, the calculations in section 7.2 gave a velocity in the range 2.47-2.67 m/s. With the desire to obtain fracture, it was decided to use a higher velocity in the first experiment. The force-displacement curves and velocity-time curves for DLE1 and DLE2 are displayed in Figure 7-17. It is clear from a) that

there was good correlation between the experiments in regards of maximum force and displacement at fracture. In both experiments fracture occurred due to membrane stresses in the plate. In DLE1 (Dynamic Longitudinal Experiment) the initial velocity was 3.48m/s. Figure 7-18 shows maximum displacement in the plate before fracture (a) and during fracture (b) for DLE1. The indenter went through the plate, so the bolts on the indenter struck the plate, and the indenter got stuck on the way back (Figure 7-19 a). Figure 7-19 b) shows shear fracture in the plate with multiple shear planes. In the next experiment, the initial velocity was reduced to 3.06 m/s, and the indenter still went through the plate, but this time it bounced back. The bottom view of fracture for DLE2 is shown in Figure 7-19 c), where it is clear that the stiffeners was almost unaffected and as in the quasi-static analysis they only developed a modest twist from the impact. Shear fracture was developed as displayed in Figure 7-19 d), this picture also shows a development of petals at the end of the indenter.

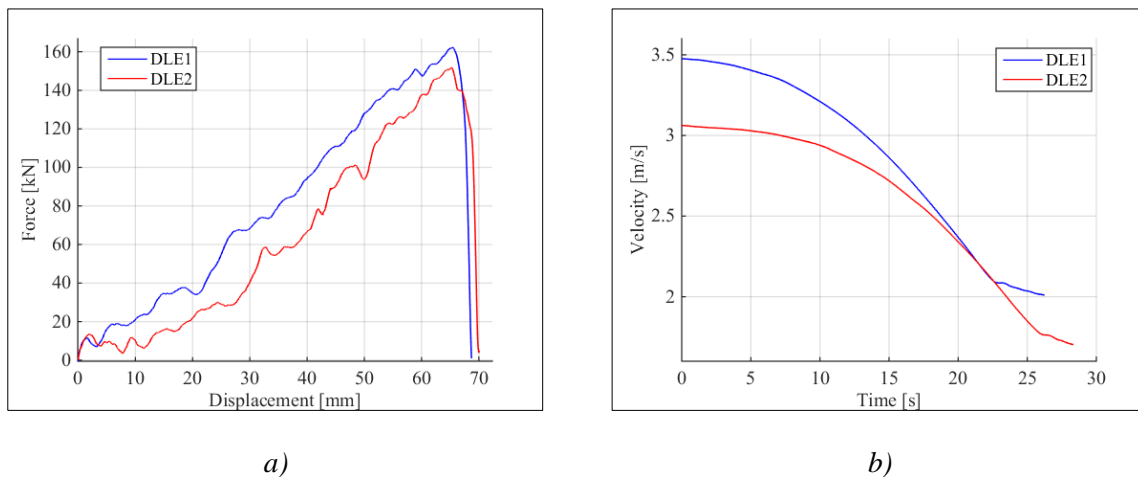


Figure 7-17: Experimental results for DTE1 and DTE2. a) Force-displacement curve and b) velocity-time curve.

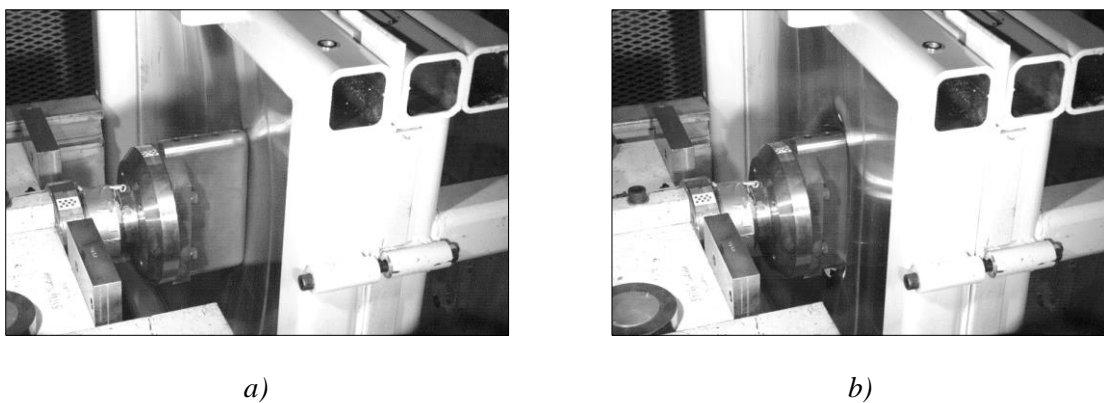
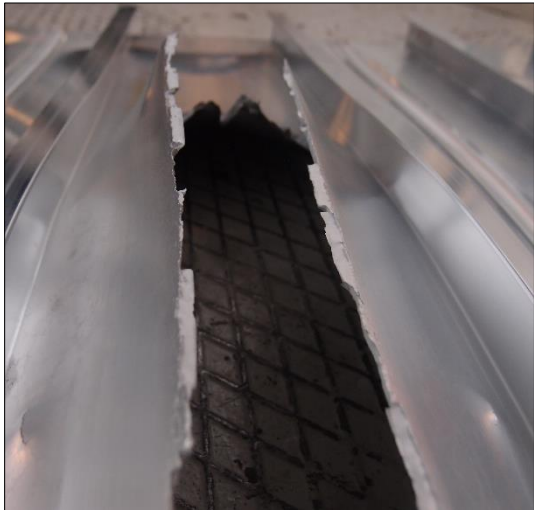


Figure 7-18: Fracture in DLE1. a) Picture right before fracture, and b) during fracture.



a)



b)



c)



d)

Figure 7-19: Fractures in plates from dynamic tests. a) Indenter stuck in plate after fracture in DLE1. b) Shear fracture in DLE1. c) Total fracture from behind and d) shear fracture in DLE2, showing petals at the end of the indenter..

7.4 Discussion

In this section the experimental results from the quasi-static and the dynamic tests are discussed separately and compared. In both the quasi-static and the dynamic tests, in both directions of the indenter, a plastic deformation of the FSW was noticed. This makes the implementation of the material properties of a separate material card for the FSW interesting to consider.

7.4.1 Quasi-static

In the test results from the component tests, a higher force was detected for the longitudinally placed indenter than for the transversally placed indenter. Figure 7-20 shows a plot where the results from the two directions are compared, and it is clear that a higher force is needed to initiate fracture in the longitudinal than the transversal direction. Before any tests or analysis were performed, this was not expected since the transverse indenter is supported by the stiffener while the longitudinal indenter mainly is supported by the top flange. One explanation to this unexpected behaviour is that the plate is not square, so for the transversally placed indenter the distance to the edge of the plate is longer than for the longitudinally placed indenter.

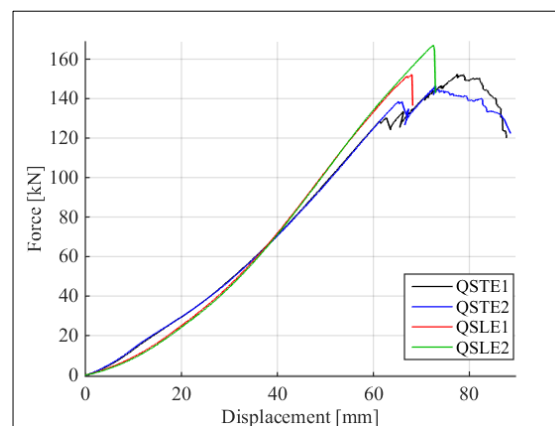


Figure 7-20: Quasi-static experiment – transversal versus longitudinally placed indenter

7.4.2 Dynamic

Figure 7-21 shows the force-displacement plots for the results from the quasi-static tests compared with the dynamic tests for the transverse indenter and the longitudinal indenter. Both directions of the indenter shows good correlation between the quasi-static tests and the dynamic tests. For both the transversal and the longitudinal indenter, the results from the two dynamic tests have a noticeable difference in slope, displacement and force. One explanation is that for both directions of the indenter, the velocity differed in the two tests that were performed, which could have an effect on the force-displacement plots. When the plate was placed in the rig and

7 Component Tests

the rig was mounted in the kicking machine, many factors could have an influence and in the end affect the final force-displacement plot of the test. This includes difference in boundary conditions and difference in friction for the different dynamic tests. In addition, a difference in inertia forces between the different tests is a possible explanation, as the aluminium plate is impacted by a moving body.

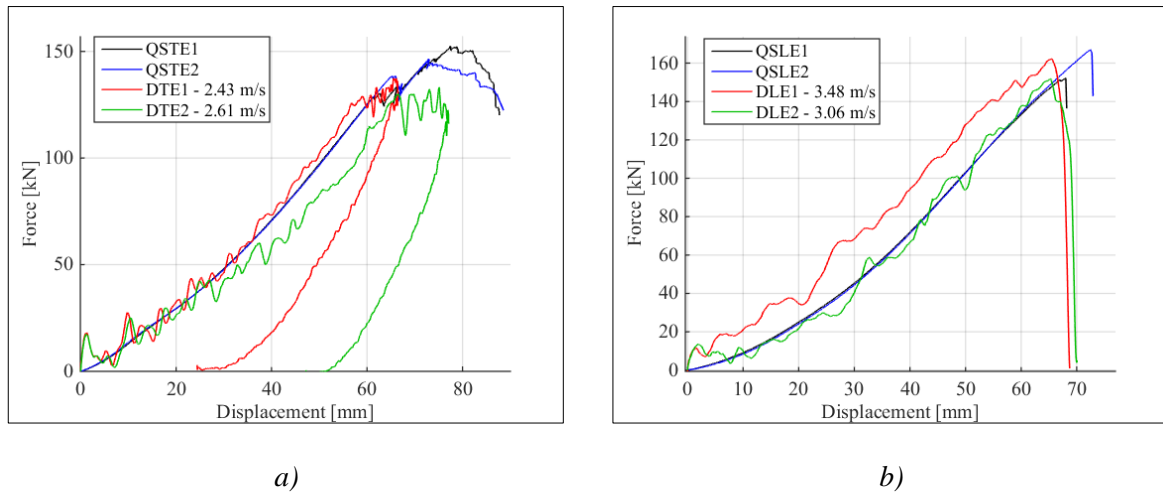


Figure 7-21: Quasi-static versus dynamic experimental results with a) transversal indenter and b) longitudinal indenter

For the transversally indenter, in the dynamic tests, fracture only occurred in the stiffeners, while in the quasi-static tests, the fracture first occurred in the stiffeners and then in the top flange. The dynamic tests seem to reach its maximum load and deflection as fracture occurred in the stiffener in the quasi-static tests. For the longitudinal indenter, the fracture occurred in the plate for both tests, and fracture seem to occur at the same maximum load and deflection for both the quasi-static and the dynamic tests. This implies that a quasi-static test could be sufficient validation for this type of experiment, in both transverse and longitudinal direction, since the correlation is sufficiently good.

8 Numerical Simulations and Discussion

To investigate the validity of the numerical model, it is compared to the experimental results. The numerical model with the deformable rig described in section 5.2 was used with the parameters and material cards described in sections 5.3 and 6.4, respectively. The material cards for the base material and the stiffeners were implemented in the simulations, while the material card for the FSW was implemented in selected analyses to investigate the effect it would have on the results. To compare the numerical analyses with the experiment, the two dynamic tests with the lowest initial velocity, DTE1 (2.43 m/s) and DLE2 (3.06 m/s), were used. Their velocities were implemented in the simulations in the transverse and longitudinal directions, respectively. For the quasi-static tests, the tests which initiated fracture at the lowest force, QSTE1 and QSLE1 were used to validate the numerical model. Two different criteria to initiate fracture were implemented in the numerical model; the Cockcroft-Latham fracture criterion and the Bressan-Williams Hill instability criterion. Both were checked with different mesh sizes to be able to discuss their use in large-scale analyses for aluminium structures. Since fracture is defined by when an element is removed in the numerical model, it could be difficult to compare the failure modes in the analysis and the experiment.

8.1 Cockcroft-Latham Fracture Criterion

The Cockcroft-Latham fracture criterion was combined with both the power law and the Voce rule before both were implemented into Abaqus/Explicit, then compared to each other and to the experimental results. The force-displacement plots and a plot showing the damage factor versus displacement with the power law versus the Voce rule are shown in Figure 8-1 and Figure 8-2. Fracture did not occur in the dynamic simulations with the indenter transversal to the stiffeners for either of the two isotropic hardening rules, but both gave good correlation to the slope of the force-displacement curve from the experiment. For the transverse indenter, the damage factor is taken from the most exposed element in the flange of the stiffener, since this is where fracture occurred in the dynamic experiments. The force-displacement curves are almost identical, but the damage factor versus displacement plot shows the difference between the power law and Voce rule more clearly. The dashed line in the damage factor-displacement plot shows the approximate displacement where fracture was initiated in the experiment, so it would be desirable to have a damage factor close to unity at that displacement. The Voce rule reaches a higher damage factor than the power law in the stiffeners, and is therefore a better fit to simulate the experiments for the transversal indenter.

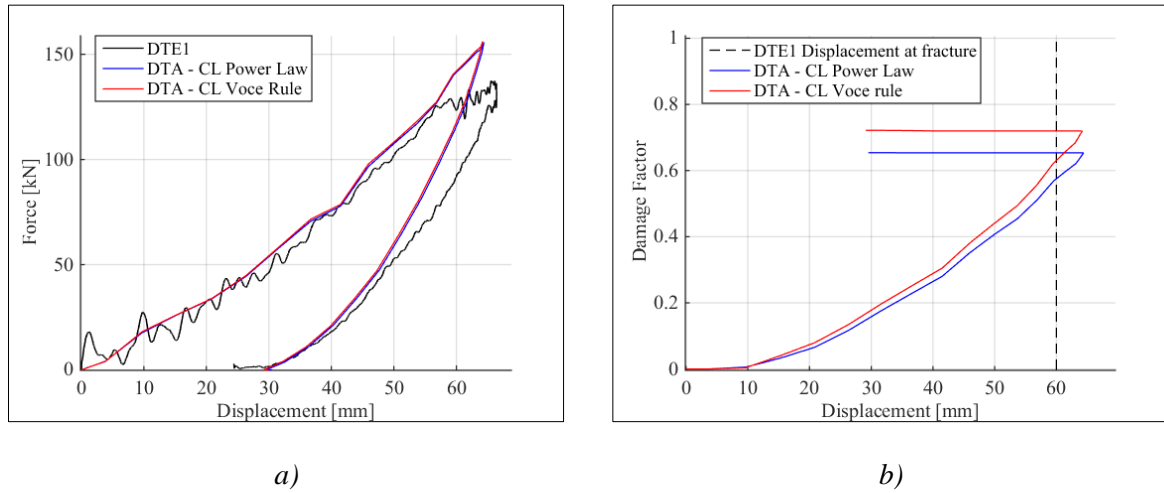


Figure 8-1: The Cockcroft-Latham criterion with power law and Voce rule for dynamic simulations with transverse indenter. a) Force-displacement curve and b) damage factor versus displacement.

For the indenter longitudinal to the stiffeners, fracture occurred for both hardening rules. It is clear from the force-displacement plot (Figure 8-2 a) that fracture is better captured by the Voce rule than by the power law. In the damage factor-displacement plot (Figure 8-2 b) both the damage factor in the integration point at the top and at the bottom in the most exposed element in the top flange are shown, where the bottom one is a dashed line. Here, it is clear that when one integration point gain a damage factor equal to one, the integration point on the other side of the top flange changes slope and goes rapidly towards one. The black dashed line illustrates approximately at which displacement fracture occurs in the experiment. It may be preferable if an element was removed in the simulations before all the integration points through the thickness reaches a damage factored equal to one, since this gives a more conservative result. It is clear that the initiation of fracture is better captured by the Voce rule than by the power law for both directions of the indenter. Due to this finding, only the Voce rule will be perused in the following section.

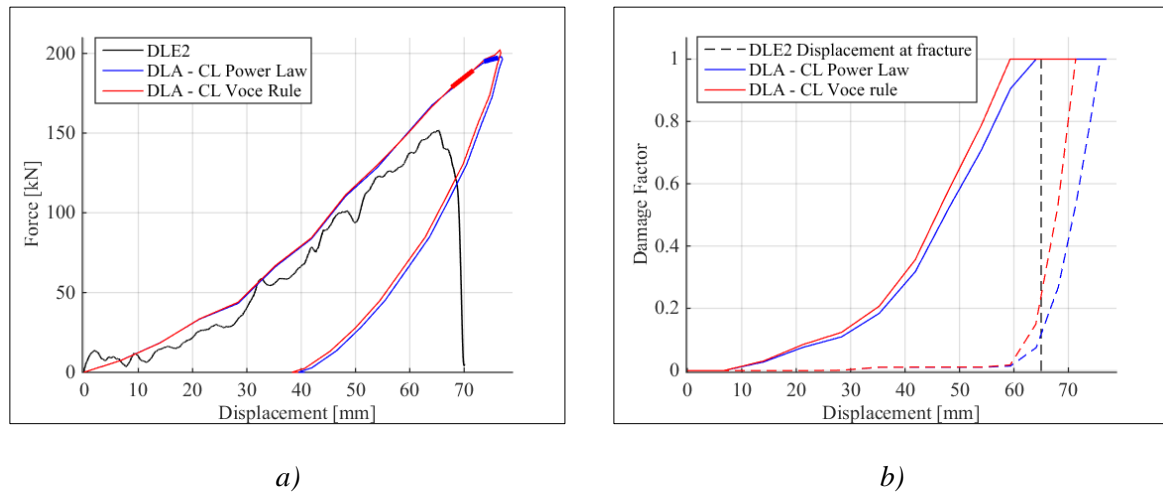


Figure 8-2: The Cockcroft-Latham criterion with power law and Voce rule for dynamic simulations with the longitudinal indenter. a) Force-displacement curve and b) damage factor versus displacement.

In Figure 8-3 the force-displacement curve for the quasi-static simulations with the Voce rule is compared to the quasi-static experiment, with the indenter in the transversal (QSTE1) and longitudinal (QSLE1) direction. In both directions of the indenter, the stiffness is relatively well captured in the simulations even though it is a bit too high compared to the experiments. The maximum force and displacement are higher than the experiments in both directions of the indenter. This can have many explanations; as was discovered in section 6.2.1, the material is strongly anisotropic with an R-ratio in the extrusion direction of, $R=0.42$. When applying a von Mises yield criterion, the material is assumed to be isotropic which can affect the results strongly. Another explanation is that the material tests for the stiffeners were taken from the web of the stiffener, while it is the flanges that fail first. In addition, the simulations are usually stiffer than real life, since the numerical model is divided into stiff elements, and in real life, the material contains impurities that are not included in the numerical model. The energy balance in relation to section 3.4.2 was controlled for both directions of the indenter, and the plots are placed in the appendix F.1.

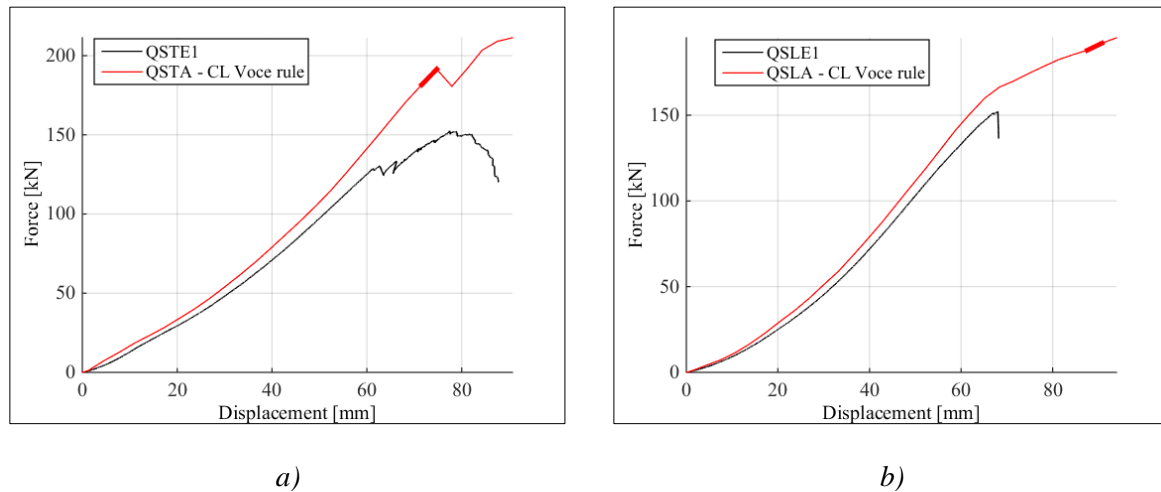


Figure 8-3: Quasi-static experiment versus quasi-static analysis for a) transverse indenter and b) longitudinal indenter

8.1.1 Various Detailed Models

In section 6.2, a large spread in the material properties of the stiffeners were discovered. The material tests from the stiffeners showed both higher and lower yield, and ultimate stress than the base material. To evaluate this difference, some simulations were run with the base material on the entire plate. Figure 8-4 a) shows the force-displacement curve of the quasi-static experiment, compared to the quasi-static analysis with the Voce rule and Cockcroft-Latham fracture criterion for the indenter placed transversally. It shows that implementing a separate material card for the stiffeners gives fracture earlier than when the material card for the base material is implemented for the entire plate. In addition, the damage factor-displacement plot (Figure 8-4 b) illustrates the evolution of the damage factor in the most exposed element in the stiffener flange, versus the approximate displacement where fracture occurred in the experiment. With the stiffener material included in the simulations, the damage factor is somewhat higher. The same types of tests were run with a dynamic simulation. In these simulations, fracture did not occur in the top flange or in the stiffeners. The force-displacement is therefore practically equal (Figure 8-5 a) while the damage factor versus displacement (Figure 8-4 b) shows that a simulation where the stiffener material is included is closer to when fracture occurred in the stiffeners in the experiment.

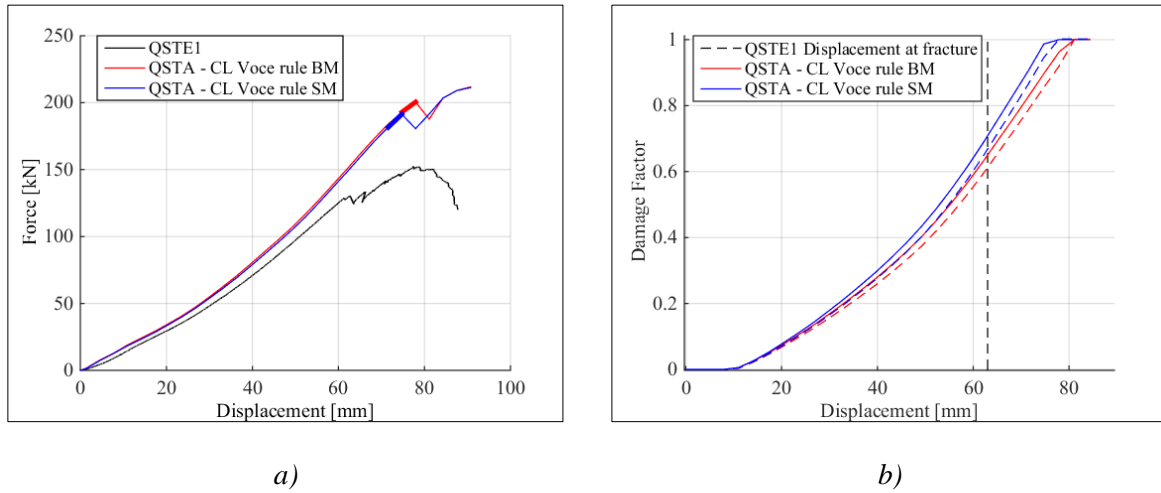


Figure 8-4: Quasi-static experiment with transversal indenter (QSTE1) versus quasi-static analysis with base material on the whole plate (QSTA Voce rule BM) and with included material in the stiffeners (QSTA Voce rule SM). a) Force-displacement plot and b) damage-displacement plot.

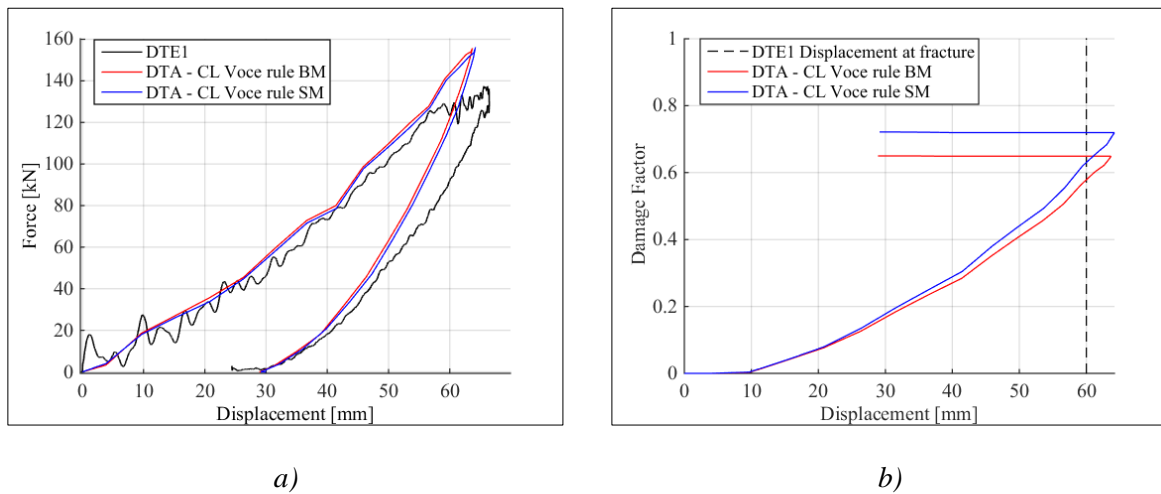


Figure 8-5: Dynamic experiment with transversal indenter (DTE1) versus dynamic analysis with only base material (DTA Voce rule BM) and with stiffener material included (DTA Voce rule SM). a) Force-displacement plot and b) damage-displacement plot.

As mentioned in section 6.4, it would be interesting to implement a yield criterion which resembles an anisotropic yield criterion. Therefore, the Hershey yield criterion was implemented in the numerical model in Abaqus/Explicit to investigate the difference compared to the von Mises yield criterion. The Hershey yield criterion gave very little to no difference in force-displacement and in damage factor. This indicates a stronger anisotropy than what the Hershey criterion manages to capture with the Cockcroft-Latham fracture criterion. The force-displacement plots and the damage-displacement plots for the Hershey criterion compared to the von Mises yield criterion and the experiment is shown in appendix F.1.

In section 6.2, the experimental results from the friction stir weld tensile test showed that the FSW is much weaker than the base material. A separate material card for the FSW was therefore implemented in the numerical model to study the effect it will have on the results. Figure 8-6 a) and b) shows the force-displacement plots for the dynamic analyses and the difference between a plate without FSW and a plate with FSW, for the transverse and longitudinal direction, respectively. In both plots it can be seen that for the simulation including the FSW, the force is slightly lower and the displacement slightly higher. This indicates that by including the FSW, the ductility of the plate increases slightly. A similar tendency is seen in the quasi-static analyses, see Figure 8-7 for both the transversal and the longitudinal indenter. In the transversal direction, fracture first occurred in the stiffener in both quasi-static analyses, and then in the top flange. In the analysis with FSW the fracture in the plate propagated along the FSW. Since the FSW had an effect on the results, it will be included in the future simulations for the Cockcroft-Latham fracture criterion.

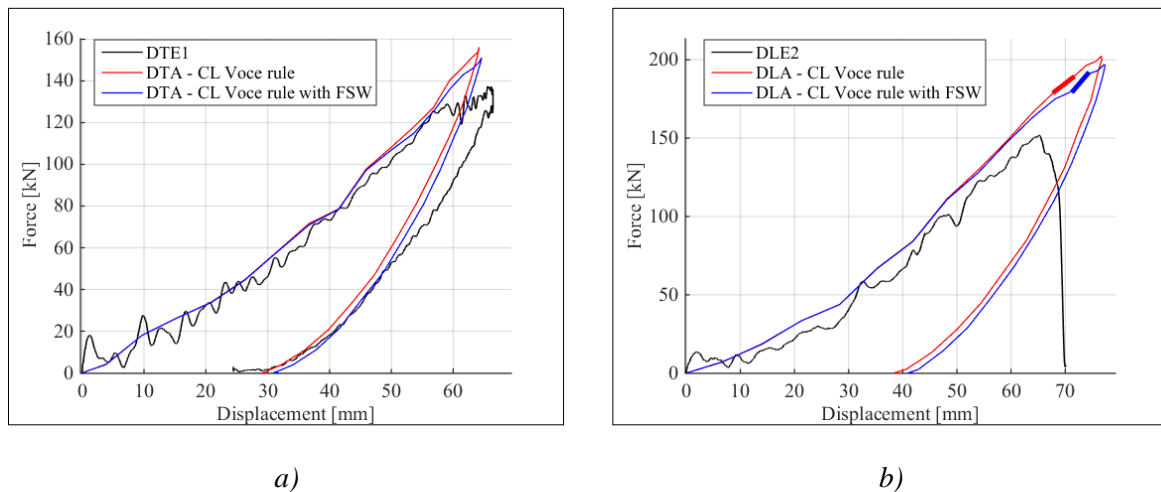


Figure 8-6: Dynamic analysis, force-displacement plot of plate without FSW compared to plate with FSW for: a) Transverse indenter and b) Longitudinal indenter

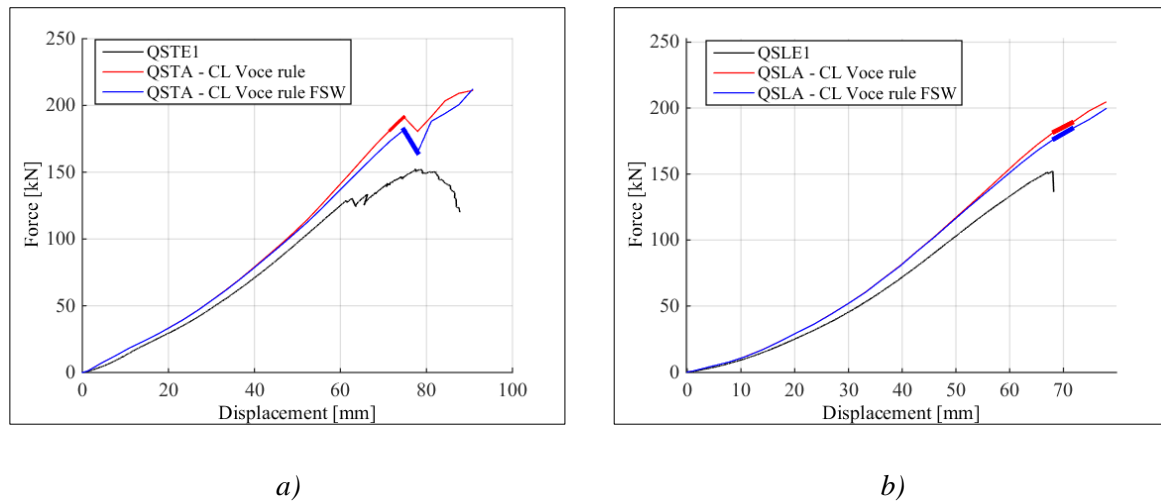


Figure 8-7: Quasi-static analysis, force-displacement plot of plate without FSW compared to plate with FSW for: a) Transverse indenter and b) Longitudinal indenter.

As mentioned in section 6.4, the plastic strain for the FSW in the numerical analysis should not be higher than approximately $\varepsilon^p = 0.04$, since the power law does not describe the material behaviour approximately after necking. This was verified in the numerical models by checking the maximum in-plane principal strain of the most exposed element in the weld. For the transverse indenter, this value is: $\varepsilon_t^p = 0.047$ and in the longitudinal indenter: $\varepsilon_l^p = 0.018$. This shows that for the transverse direction the power law fitting is not sufficient, since the plastic strain is larger than the strain at diffuse necking in the uniaxial tensile test.

The plates were produced with small “lips”, next to the friction stir welds. Figure 8-8 shows the plate including the FSW and the “lips”. The “lips” were implemented in Abaqus as solid elements to investigate their effect on the simulations. In Figure 8-9, the simulations with, and without, the “lips” are compared to the experimental test, here including the FSW, to see if the strains are decreased by the “lips”. The plots show that there was no effect from including the “lips” in the simulations, and the strains in the FSW were not decreased either. Due to these observations, it was decided to not proceed with simulations that include the “lips”. In addition, since the “lips” are very small, if running a simulation with a large mesh size, the mesh may be distorted by the small solid elements.

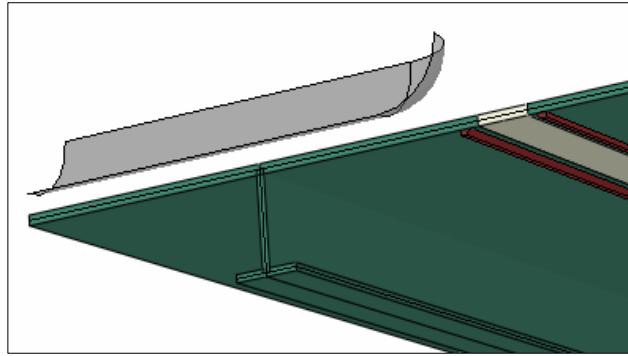


Figure 8-8: Numerical model with FSW and "lips".

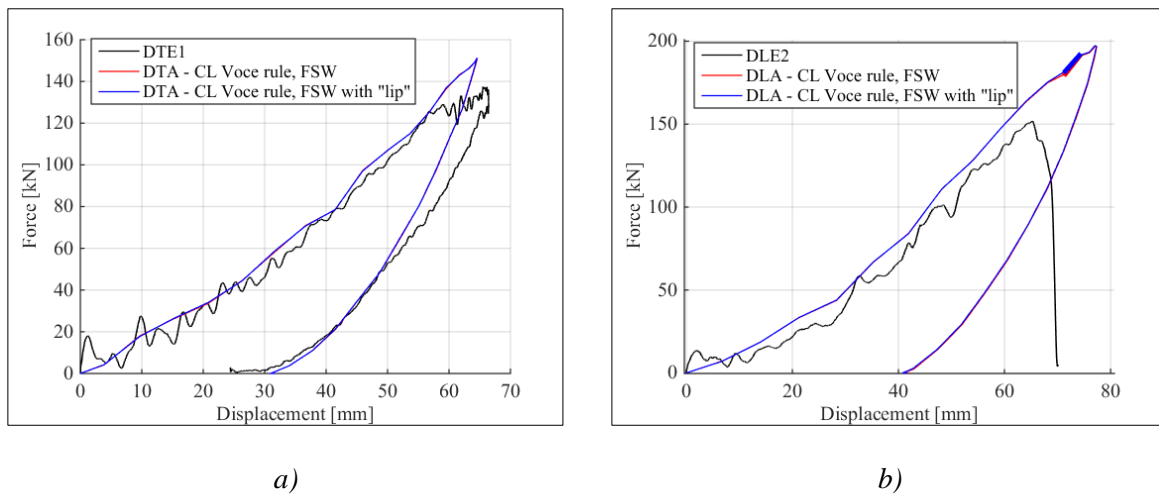


Figure 8-9: Force-displacement plot of plate without "lip" compared to plate with "lip" for: a) Transverse indenter and b) Longitudinal indenter.

When doing the material tests, it was discovered that the thickness of both the plate and the stiffeners were not accurate. Therefore, an average of the measured thicknesses for the t and the stiffeners were implemented, see appendix D.1 for all the measurements. The average of the thickness in the top flange was calculated to be $t_{tf} = 4.23\text{mm}$, which is 5.75% higher than the thickness first implemented for the top flange. The average of the stiffener thickness was calculated to be $t_{stiffener} = 2.85\text{mm}$, which is 5.0% lower than first implemented. Figure 8-10 shows force-displacement plots where the assumed thickness is compared to the average of the measured thickness for both directions of the indenter.

The damage factor showed to be approximately equal for both directions of the indenter. As the force increases and the displacement decreases for both the transverse and longitudinal direction, it indicates that the thickness of the top flange has more influence on the force and displacement than the thickness of the stiffener. Since the thickness of both the top flange and the stiffeners varies a lot, and for simplification of simulations, it was decided to proceed with the assumed thicknesses of, $t_{plate} = 4.0mm$ and $t_{stiffener} = 3.0mm$.

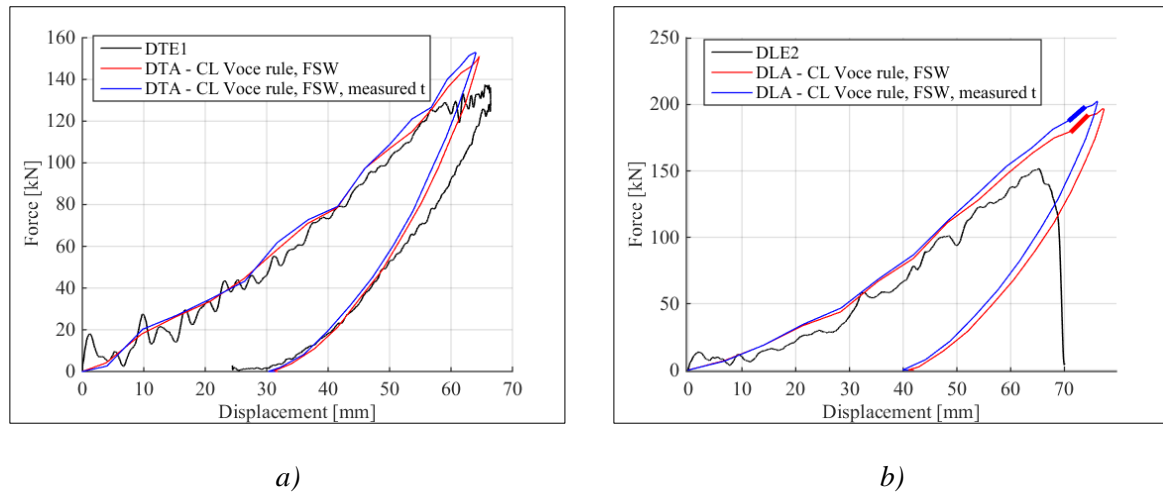


Figure 8-10: Force-displacement plot of plate with assumed thickness and average of measured thickness for: a) Transverse indenter and b) Longitudinal indenter

8.1.2 Selected Model

Due to the observations in the previous section, it was concluded that the model with separate material card for the stiffeners and FSW without including the “lips” and the measured thicknesses, is acceptable, though somewhat simplified. In the numerical simulations, as in the experiments, there was a visible necking of the stiffeners for the transverse indenter while for the longitudinal indenter, the twisting of the stiffeners was not detected in Abaqus. In Figure 8-11, the necking of the stiffener in the experiment is compared to the numerical analysis, where the equivalent plastic strain (PEEQ) is illustrated. This shows a similarity between the necking in the experiment and the analysis, and in addition, the analysis shows an accumulation of strains where the crack is visible in the experiment. In Figure 8-11 b) the PEEQ reaches a value of 0.22, while for the longitudinal indenter the PEEQ reached a value of 0.26 right before fracture. This is significantly lower than the value used for PEEQ at fracture in the introductory model. The low value of PEEQ could be a result of artificial aging, which gives decreased ductility, see section 2.1.1.

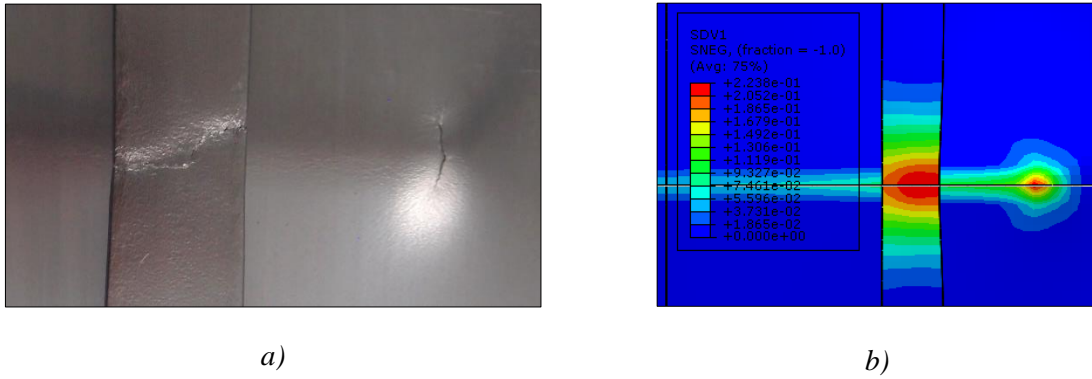


Figure 8-11: Necking of stiffeners in a) experiment and b) numerical simulation

In Figure 8-12, the velocity versus time plot is shown for this model in both directions, and compared to the representative experiments. The velocity in the transverse direction is well captured by the simulations. The slope is a bit more steep than in the experiment, but it results in about the same residual velocity. With the indenter in the longitudinal direction, the curve from the simulations is closely following the velocity in the experiment up to fracture. The small differences in velocity can be described by variances in boundary conditions and friction in the experiment and the model, and by a difference in stiffness since a numerical model usually is stiffer than real life.

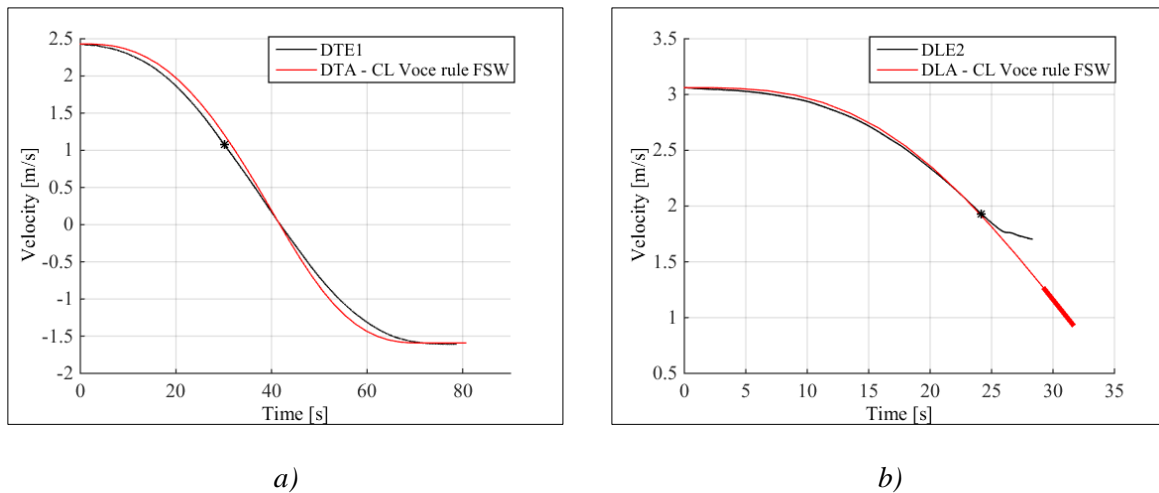


Figure 8-12: Velocity-time plots for analysis versus experiments for a) Transverse indenter and b) longitudinal indenter.

Figure 8-13 a) and b) shows the absorbed energy for the experiment versus the analysis with stiffer material and FSW in the transverse and longitudinal direction, respectively. This indicates that the numerical model cannot reproduce the exact energy at fracture as the experiment. In both directions of the indenter, the absorbed energy increases faster in the numerical analysis, than in the experiment, and Figure 8-13 b) shows that for the longitudinal indenter, where fracture is initiated in the analysis, the fracture energy is 50-60% larger than the experiment. Some explanations to this might be, as previously mentioned, the numerical model does not consider anisotropy in the material, it is stiffer than real life and does not consider impurities. Other reasons for this disagreement in absorbed energy might be difference in boundary conditions and difference in friction state. As seen in the parameter study conducted in section 5.2.4, the stiffness of the model is dependent on the friction between the support and the plate.

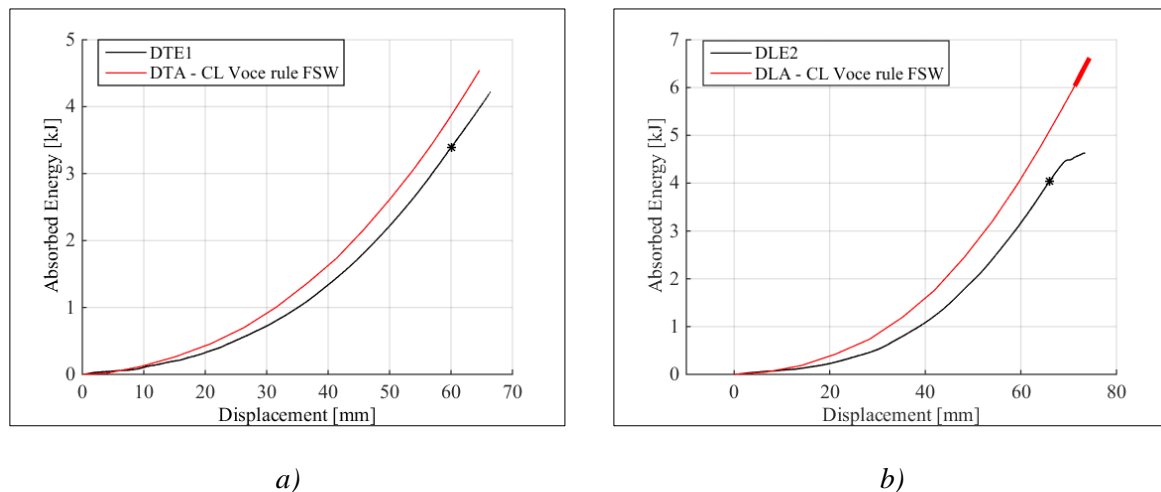


Figure 8-13: Experiment versus analysis energy-displacement plot for a) transverse indenter and b) longitudinal indenter.

In section 7.4.2, both directions of the indenter showed good correlation between the quasi-static and the dynamic experiments. This is also the case for the numerical simulations. In both directions of the indenter there is good correlation between the dynamic and quasi-static simulations, see Figure 8-14. In the dynamic simulations for the transversal indenter, since fracture was not initiated, the damage factor at maximum displacement was studied instead. The damage factor for the most exposed element in the flange for the dynamic simulation was found to be 0.72, and in the quasi-static at the same displacement 0.73. For the longitudinal indenter fracture occurred at approximately the same force and displacement. This shows, as in the experimental results, that a quasi-static analysis could be sufficient validation for this type of experiment on AA6082-T6.

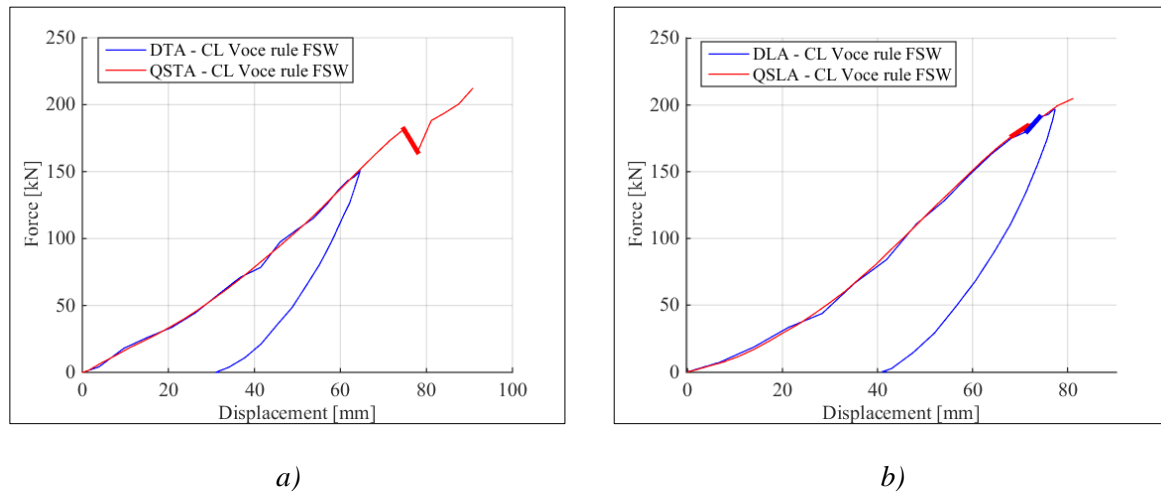


Figure 8-14: Dynamic analyses versus quasi-static analyses for a) Transverse indenter and b) Longitudinal indenter

8.2 The Bressan-Williams-Hill Instability Criterion

The Bressan-Williams-Hill (BWH) instability criterion is strain path independent, which is favourable when applying it to sheet metals under large deformations, such as deformation due to impact loading. In section 6.2, a low degree of hardening in the material was noticed. With a low degree of hardening, the BWH criterion could give an inaccurate estimation of fracture, since a small change in stress might give a large change in strain. The criterion applies the power law formulation described in section 2.6.3 and initiates fracture when instability is detected in an element in Abaqus/Explicit. Alsos et al. (2008) found that the BWH criterion predicts failure without being overly sensitive to the mesh size, so the BWH criterion was run with mesh size equal to the thickness, 2.5 times the thickness and 5 times the thickness to validate this statement. Mesh sizes larger than five times the thickness do not detect local instability and to account for this, the fracture criterion needs to be element size dependent (Alsos et al., 2009). Alsos et al. (2008) set the $\hat{\epsilon}_1$ equal to the hardening exponent of the power law, n , but in this master thesis a mesh-scaling factor is used to reduce the ductility when elements larger than the thickness are applied. The matlab script used to generate the material card for the BWH criterion was provided by Postdoc. David Morin, and is shown in appendix E.4.

Figure 8-15 a)-c) shows the FLDs for the base material, stiffener material and FSW, respectively, where the effect of the mesh-scaling factor is illustrated. Figure 8-15 d) is a comparison of the different materials with mesh size five times the thickness and shows that the material in the FSW is very different from the base material and the stiffener material. This can be explained by a value of n in the power law, which differs considerably from the other two materials, and leads to a steeper curve on the left-hand side of the plot, see sections 6.3.2 and 6.3.3.

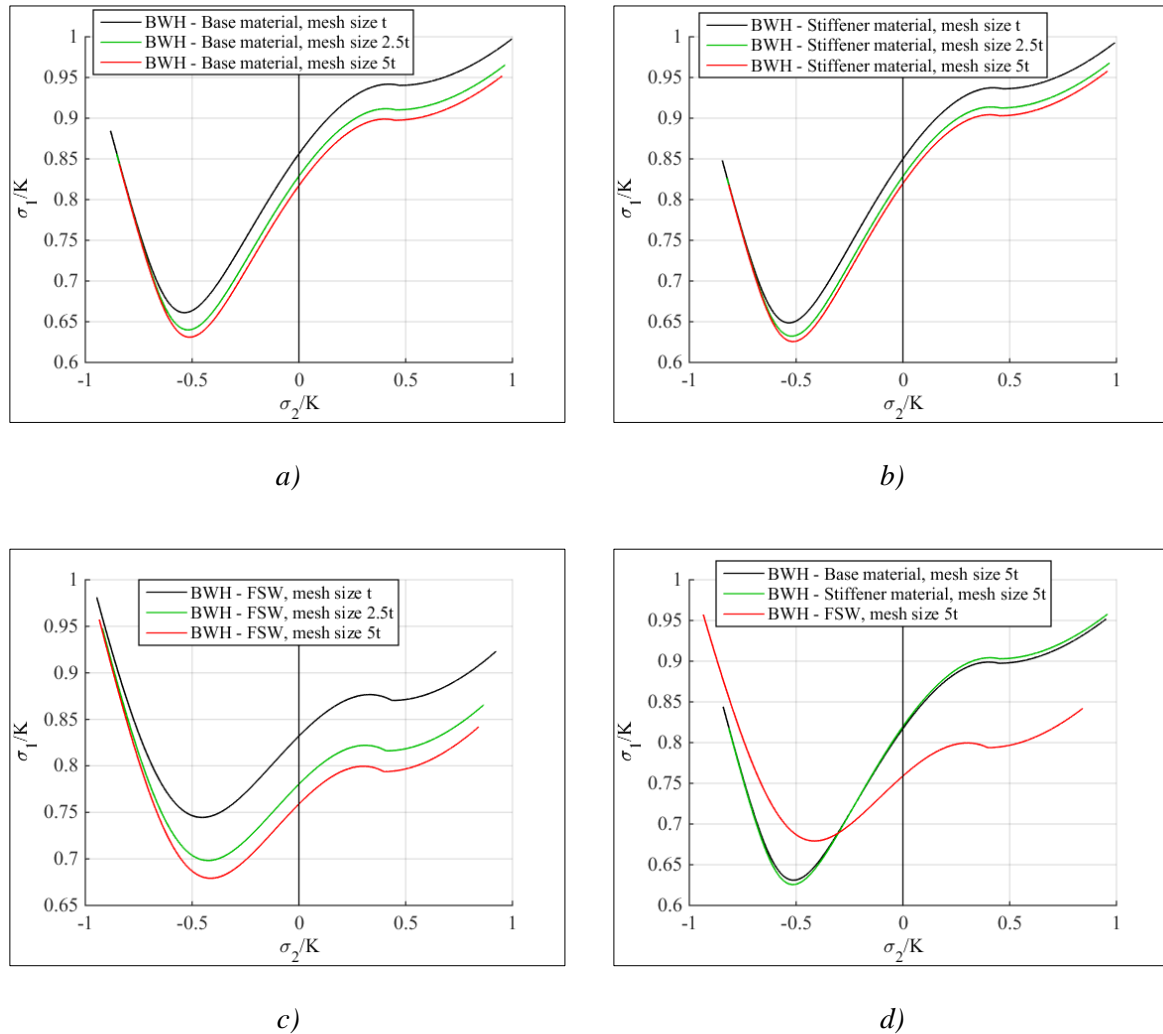


Figure 8-15: BWH FLDs for a) base material, b) stiffener material, c) FSW and d) the three materials compared with mesh size $5t$.

First, the model without the FSW was implemented with the BWH criterion. This showed good correlation with the experimental results for all mesh sizes, but fracture was initiated at different displacements for the different mesh sizes, see Figure 8-16. This indicates that the criterion might have some sensitivity to the mesh size, which could be because large mesh sizes do not detect strain concentrations as well as finer mesh sizes. For the transversally placed indenter,

fracture occurred earlier than the experiment for all mesh sizes tested. This is still a valid approximation since the BWH criterion predicts local instability, not final fracture. For mesh sizes 2.5 and 5 times the thickness, fracture occurred earlier than when the mesh size is equal to the thickness. This was not expected since the force usually decreases for a smaller mesh size. One explanation for this could be that the contact formulation between the indenter and the plate changes for the different mesh sizes. It could also be a result of the effect from the mesh-scaling factor. For the longitudinally placed indenter, fracture did not occur for a mesh size 5 times the thickness while for mesh size 2.5 times the thickness and mesh size equal to the thickness, fracture occurred approximately at the same displacement as the experiment.

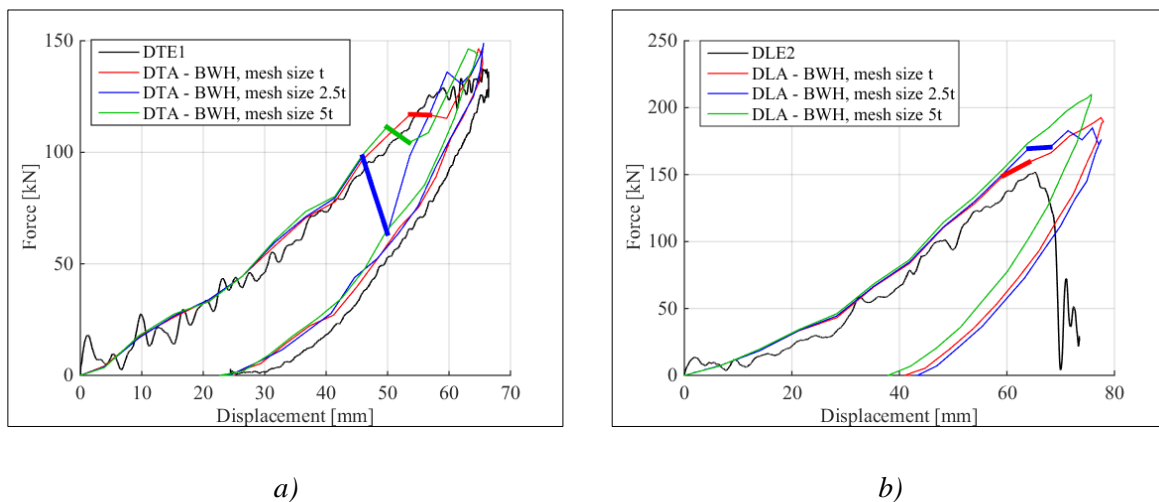


Figure 8-16: Dynamic analysis with BWH instability criterion compared to experiment for the a) transverse and b) longitudinal indenter

A BWH material card was also made for the FSW in the plate, and implemented in the model. Figure 8-17 shows the results for the numerical analyses with the FSW included. These results have been compared to the results when FSW is not included, and they are very similar. From this observation, it was decided that in large-scale analyses, the FSW could be excluded without affecting the results too much. The “lips” were not included in these analyses, as it was assumed that because they gave no difference in result for the CL fracture criterion, they would also not affect the results for the BWH criterion. In addition, since the BWH criterion is meant to function for large mesh sizes, it should not be included since it can distort a large mesh.

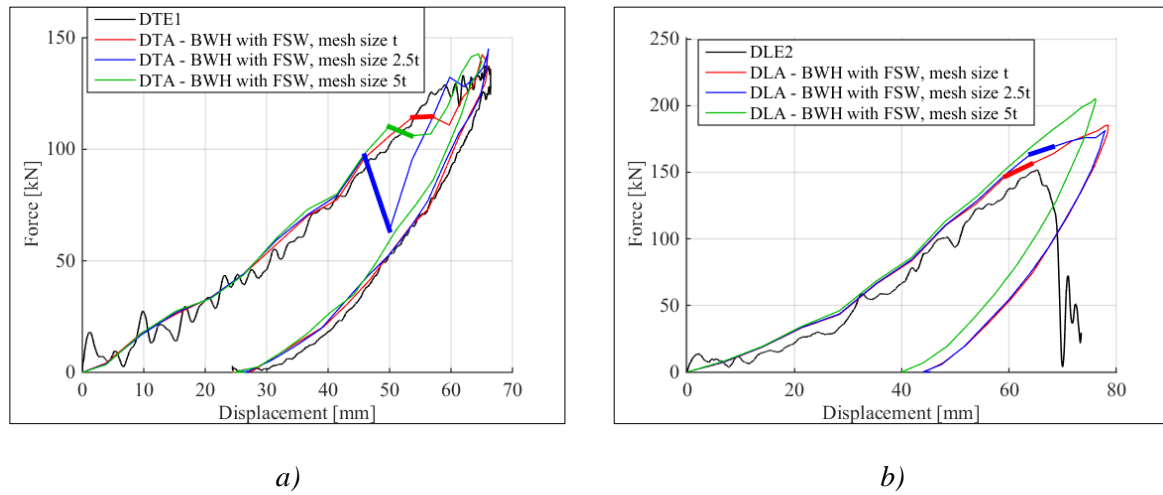


Figure 8-17: Dynamic analysis with BWH instability criterion with FSW included compared to experiments for the a) transverse indenter and b) longitudinal indenter

Fracture did not occur for the mesh size five times the thickness for the longitudinally placed indenter. Therefore, a plot showing the σ_1 calculated from the BWH criterion using the maximum and minimum principal strain from the analysis, and comparing it to the maximum principal stress from the analysis is shown in Figure 8-18. In this figure, it can be seen that for mesh size five times the thickness, the analysis is very close to fracture. The plot also shows that the two analyses with and without including the FSW are approximately equal, with only a small difference after maximum stress occurred. The calculated stress from the BWH criterion, σ_1 , for the two models were overlapping, so only one is shown in the plot.

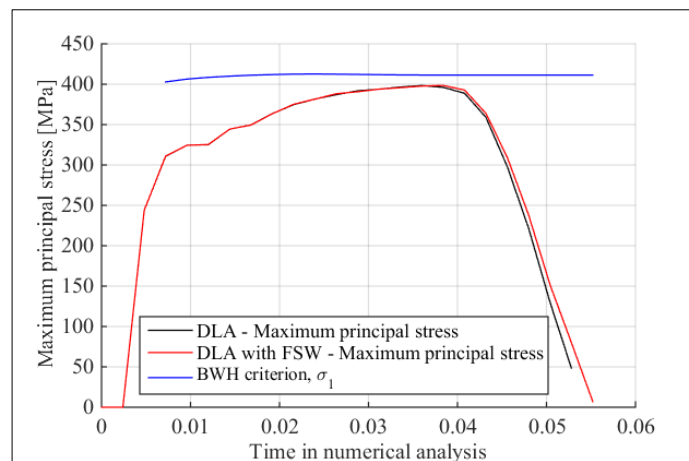


Figure 8-18: Maximum principal stress versus σ_1 from the BWH criterion

The numerical simulations were also run as quasi-static analyses for the model without the FSW. The force-displacement plot for the model not including the FSW is shown in Figure 8-19, where the same trend as in the dynamic analyses is detected. In the transverse direction, fracture is initiated in the stiffener in the analyses before it occurred in the experiment, while for the longitudinal indenter, fracture is initiated in the plate in the analyses at the same time or after it occurred in the experiment. When fracture occurs in the stiffeners, the flange is subjected to tension and the fracture is described by the left side of the FLD, and Hill's theory, but when fracture occurs in the plate, the fracture is described by the right side of the FLD, and the Bressan-Williams theory. This is could be an explanation as to why the fracture happens at different displacements relative to the experiments for the transverse and the longitudinal indenter.

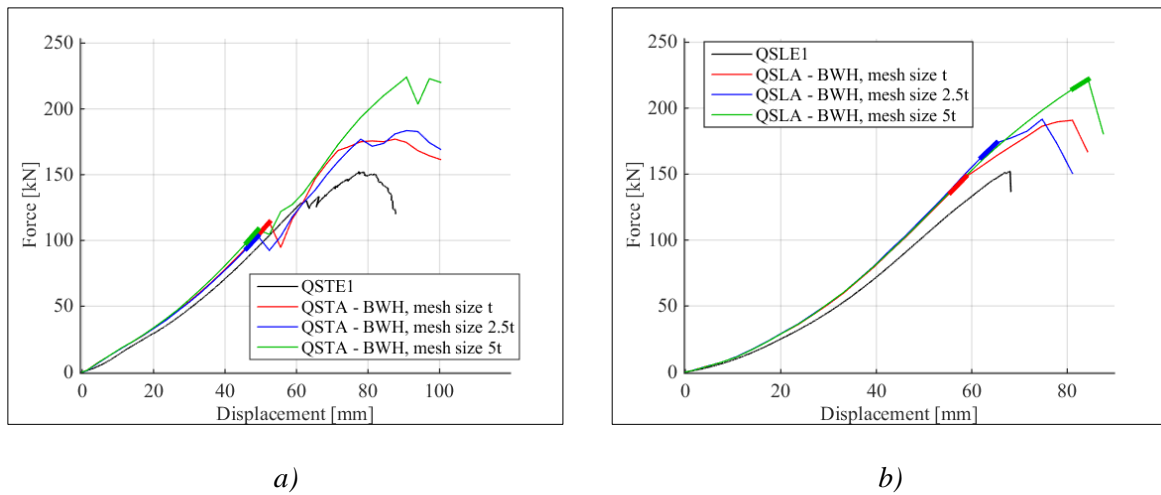


Figure 8-19: Quasi-static analysis for the BWH criterion without the FSW for the a) transverse and b) longitudinal indenter

As for the CL criterion, the energy at fracture was compared for the BWH instability criterion with the experimental results. As for the CL criterion, the energy increases faster in the analyses than in the experiment, but since fracture occurs earlier in the BWH criterion, the agreement is better than in the CL criterion. It shows acceptable compliance between the different mesh sizes, which is good for the use of large meshes.

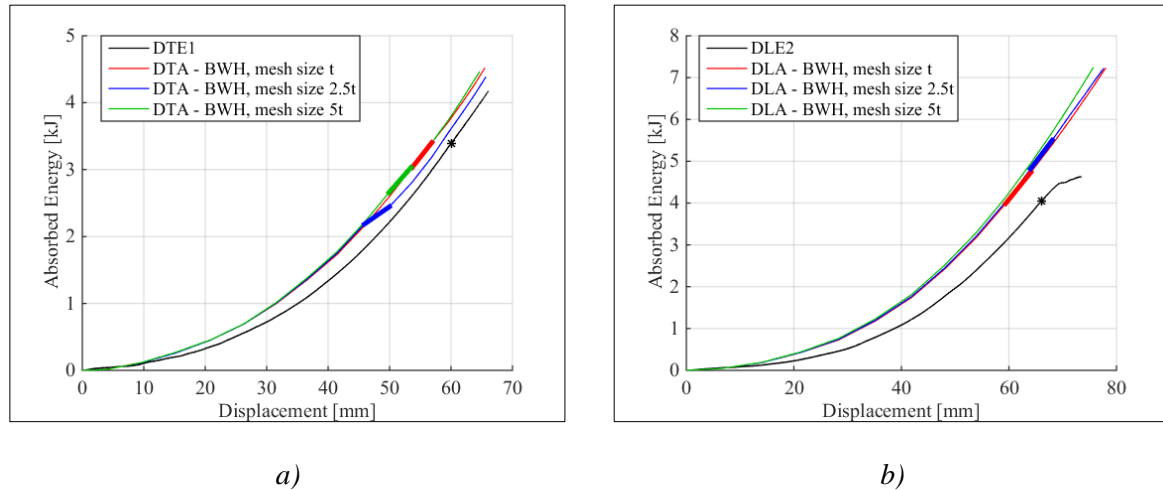


Figure 8-20: Absorbed energy versus displacement plots for dynamic analyses for the a) transverse and b) longitudinal indenter

8.2.1 Comparison between the BWH Instability Criterion and the CL Fracture Criterion

In the previous section, the BWH instability criterion has been implemented in the numerical model with different mesh sizes and has been compared with the experimental results. The criterion has shown acceptable correlation to the experimental results, when considering the uncertainties that have been mentioned in previous sections. In Figure 8-21, the Cockcroft-Latham fracture criterion has been implemented with different mesh sizes to be able to compare it to the BWH instability criterion. It appeared that the damage factor in the CL criterion decreased significantly as the mesh size was increased, so it is not a good approximation when using large mesh sizes. The BWH criterion showed good correlation for all mesh sizes, and as the mesh size was increased the mesh scaling factor ensured that fracture occurred sooner due to lower ductility for large elements. It should be added that a mesh-scaling factor was not used for the CL criterion, which could be an explanation to the damage factor decreasing fast. In Table 8-1, the computational time for some representative analyses are shown for the transverse indenter. This shows that the analyses with the BWH criterion needs less time than the analyses with the CL criterion for the same mesh size. Since the CL criterion only has acceptable results for a fine mesh, and the BWH has acceptable results for a coarser mesh, the BWH criterion can be called much more effective than the CL criterion in large scale analyses.

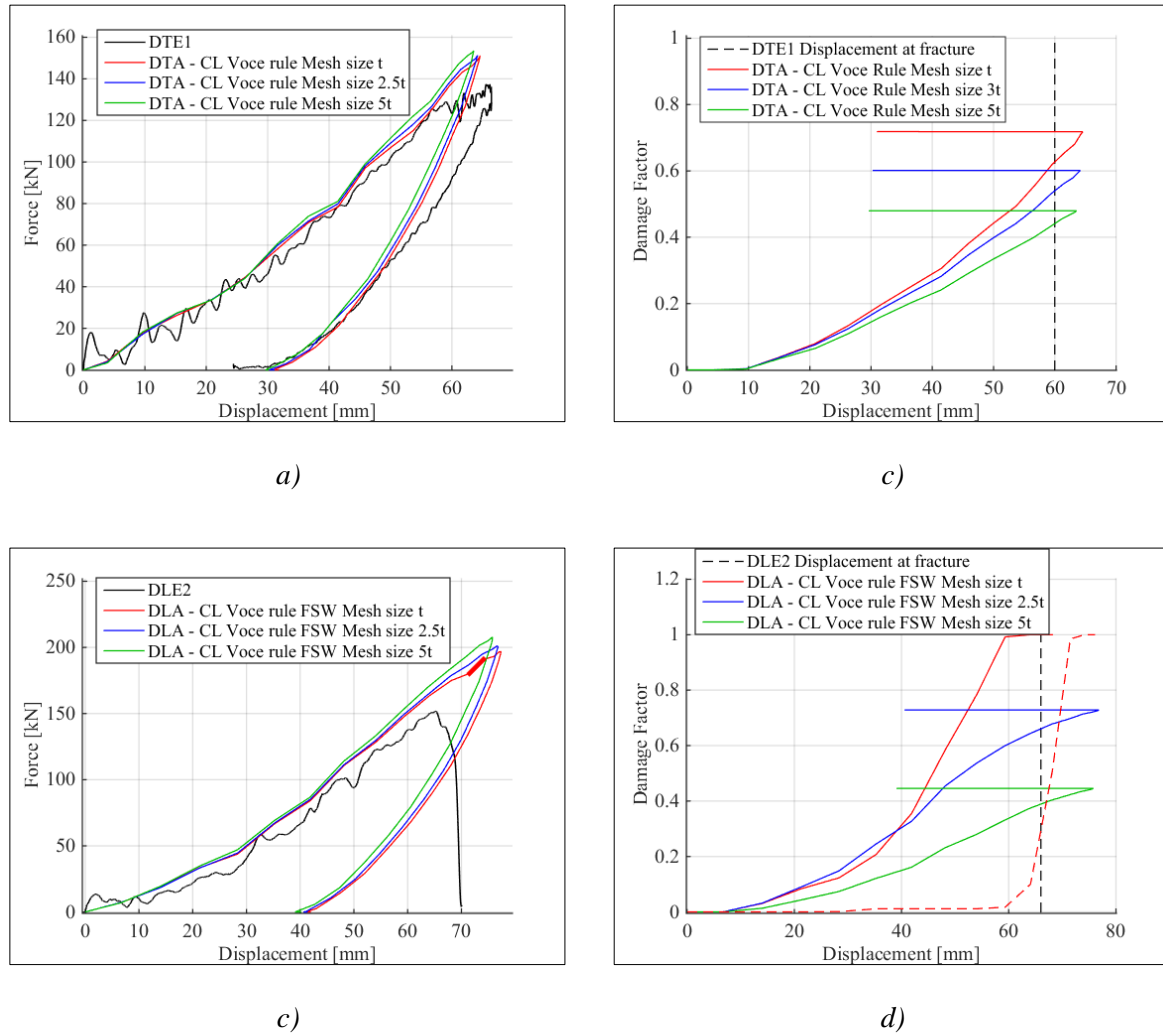


Figure 8-21: Dynamic experiment versus CL dynamic analysis with different mesh sizes. a) force-displacement for the transversal indenter, b) damage factor-displacement for the transversal indenter, c) force-displacement for the longitudinal indenter and d) damage factor-displacement for the longitudinal indenter.

Table 8-1: Computational time for representative analyses

Transverse indenter	Quasi-Static		Dynamic	
	CL	BWH	CL	BWH
Mesh size t	8t 33min	5t 14min	2t 57min	1t 46min
Mesh size 2.5t	-	-	21min	11min
Mesh size 5t	-	-	8min	8min

8.2.2 Marciniak-Kuczynski Analyses

A more commonly used forming limit diagram, is the strain based FLD, Marciniak-Kuczynski (MK). This FLD was included to investigate the difference when using the MK FLD and when using the BWH criterion. The procedure suggested by Marciniak and Kuczynski is used to calculate the right-hand side of the FLD, while the right side is calculated by the method of Hill and shifted down to intersect at the corresponding plane strain for MK. The right-hand side is calculated by assuming a pre-existing defect in form of a groove or a trough oriented perpendicular to the axis of largest principal stress and strain. In the groove, the material is either thinner or weaker than outside it. Let 'a' denote the region outside the groove, and 'b' the region inside the groove. The force must be the same inside and outside the groove and deformation is assumed to occur so that the ratio of stresses and strains ($\alpha_a = \sigma_{a2} / \sigma_{a1}$ and $\rho_a = \Delta\varepsilon_{a2} / \Delta\varepsilon_{a1}$) remain constant. The numerical solution involves imposing increments of strain in the groove ($\Delta\varepsilon_{b1}$) and finding the corresponding strain outside the groove ($\Delta\varepsilon_{a1}$). The strain outside the groove becomes smaller and smaller as the deformation progresses for a given increment of the strain in the groove, and consequently $\Delta\varepsilon_{a2} = \Delta\varepsilon_{b2}$ decreases, and the flow in the groove approaches plane strain when $\Delta\varepsilon_{b2} = 0$. Failure is set to occur when the relation between the strain outside and in the groove ($\Delta\varepsilon_{a1} / \Delta\varepsilon_{b1}$) is very large (Hosford and Caddell, 1993). For more detailed calculations of the FLD, see chapter 15-5 'Calculations of forming limit diagrams' in Hosford and Caddell's (1993) book, 'Metal Forming'.



Figure 8-22: FLD for BWH with all mesh sizes and MK with von Mises and Hershey yield criterion compared for a) base material and b) stiffener

In Figure 8-22, the FLDs from Marciniak-Kuczynski for both the von Mises and the Hershey yield criterion compared to the FLD from the BWH instability criterion is shown. It is important to consider that the FLD from the BWH criterion is based on the power law, while the FLDs from MK is based on the Voce rule, so the different FLDs cannot be compared directly. In this master thesis, the calibration for the Voce rule and the power law are very similar, as seen in 8.1, where they gave comparable results for the Cockcroft-Latham fracture criterion.

The MK with the von Mises yield criterion was implemented in matlab with different mesh sizes to investigate how it differs from the BWH criterion. The MK with the Hershey criterion was not included in this master thesis due to its complicated implementation and how time consuming it would have been. In addition, the Hershey criterion did not show a large difference from the von Mises criterion when implementing it in the CL fracture criterion, so it can be presumed that it would not show a large difference in the MK FLD either. Figure 8-23 shows the force displacement plots for the analyses implemented with the MK FLD with the von Mises yield criterion. As expected, since the FLD for the MK and the FLDs for the BWH are very similar, the force displacement plots for MK give approximately the same results as for BWH. This gives more reason to state that the estimates from the BWH instability criterion are acceptable.

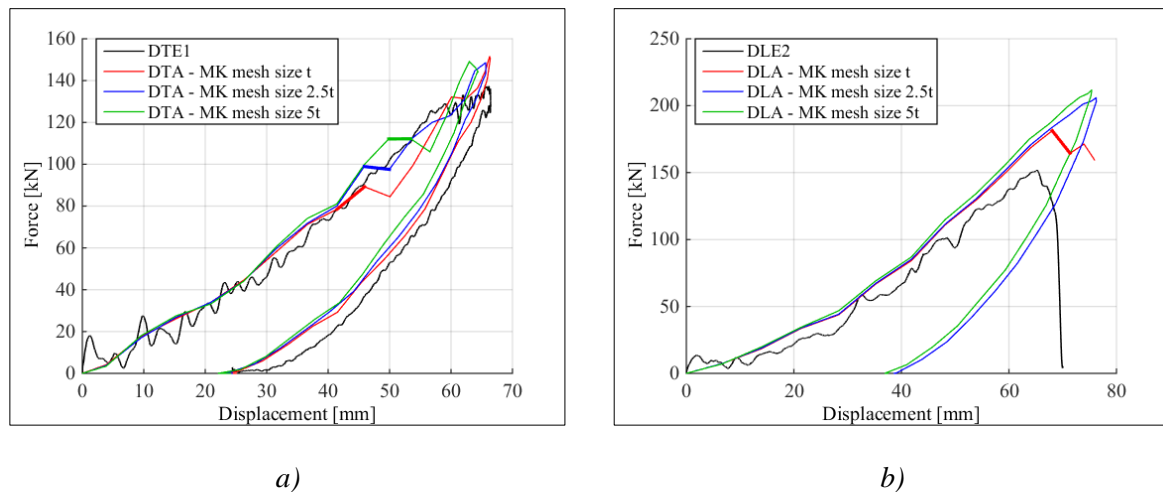


Figure 8-23: Dynamic analysis for the MK FLD without the FSW for the a) transverse and b) longitudinal indenter

9 Conclusions and Proposals for Future Work

In this master thesis, dynamic and quasi-static experiments were conducted on stiffened aluminium plates with a cylindrical indenter pointing transversal and longitudinal to the stiffeners. The plate consists of aluminium profiles welded together by friction stir welds, and the indenter hits the plate between the welds. The experiments were simulated and attempted validated in Abaqus/Explicit. In order to perform the laboratory experiments, a rig fixing the aluminium plate in the test machine was designed. In the following sections, concluding remarks and proposals for future work are presented.

9.1 Conclusions

- In the material tests it was discovered that the material that was investigated in this master thesis, aluminium alloy AA6082 with temper T6, have a greater degree of anisotropy than expected.
- A large difference of the material properties in the top flange, stiffeners and the friction stir welds (FSW) was detected.
- In the component tests, a good correlation was detected between the quasi-static and dynamic experiments for both the transverse and the longitudinal indenter. This gives grounds to conclude that a quasi-static experiment could give satisfying validation for this type of experiment on AA6082-T6.
- The Cockcroft-Latham fracture criterion gave acceptable estimates in regards of initiation of fracture with a mesh size equal to the thickness of the plate. With coarser mesh size the accuracy decreased significantly.
- The Bressan-Williams-Hill instability criterion gave acceptable estimates in regards of initiation of fracture with mesh sizes varying from equal to the thickness to five times the thickness. The estimates are somewhat conservative, and a slight mesh sensitivity was detected.
- When including the friction stir welds in the numerical simulations of the plate, it did not show a significant effect in either the Cockcroft-Latham fracture criterion or the Bressan-Williams-Hill instability criterion. It may therefore be safe to model the plate without the FSW in a large-scale analysis in this type of tests, where the impact area is between the welds.

- The small “lip” on the side of the aluminium profile was included in the numerical model as solid elements. Including the “lips” did not affect the force-displacement plots from the numerical model. It can thus be concluded that excluding the “lips” are a reasonable presumption in large scale analyses.

9.2 Proposals for Future Work

In this master thesis, the isotropic von Mises yield criterion was used when approaching the material model, and in the discussion, the Hershey yield criterion was implemented. Since a strong anisotropy was detected for the aluminium alloy AA6082-T6 in section 6.2.1, an anisotropic yield criterion could give improved results.

A more advanced fracture model could improve the fracture initiation in the numerical model.

In the material test, only the web in the stiffener was tested. Performing material tests of the flange in the stiffeners as well, could improve the material model. In addition, a variation between the material tests in different stiffeners were detected, material tests on multiple stiffeners should therefore be conducted.

In this master thesis, the indenter hit the aluminum plate between the friction stir welds with a cylindrical nose with rounded edges. It could be interesting to investigate the effect of moving the indenter so it hits closer to or on the weld. In addition, changing the geometry of the plate and indenter, and performing experiments with higher velocities might also be interesting.

Plastic strain past the diffuse necking strain in the uniaxial tensile tests was detected in the numerical model of the plate including the FSW. By calibrating the FSW using multiple terms of the Voce rule, the material behaviour in the FSW could be better described past diffuse necking. If conducting a hardness test in the area of and around the friction stir weld, a more accurate description of the material parameters may be found for and around the FSW.

Doing experiments with other aluminium alloys and with different tempers could be interesting for future experiments. Changing the temper used in this thesis from T6 to T4 would increase the ductility of the plate and thus absorb more energy in the experiments. In addition, experiments should be performed on MIG-welded plates since this type of welding gives a larger heat affected zone.

References

- ABAQUS INC. 2005. *Abaqus Lecture 5 - Quasi-Static Analyses* [Online]. Abaqus Inc., Available: <http://imechanica.org/files/15-quasi-static.pdf> [Accessed 22.04 2015].
- ALSOS, H. S., AMDAHL, J. & HOPPERSTAD, O. S. 2009. On the resistance to penetration of stiffened plates, Part II: Numerical analysis. *International Journal of Impact Engineering*, 36, 875-887.
- ALSOS, H. S., HOPPERSTAD, O. S., TÖRNQVIST, R. & AMDAHL, J. 2008. Analytical and numerical analysis of sheet metal instability using a stress based criterion. *International Journal of Solids and Structures*, 45, 2042-2055.
- ANDERSON, T. L. 2005. *Fracture Mechanics Fundamentals and Applications*, Taylor & Francis Group, LLC.
- BACKMAN, M. E. & GOLDSMITH, W. 1978. The mechanics of penetration of projectiles into targets. *International Journal of Engineering Science*, 16, 1-99.
- BLAU, P. J. 1992. *ASM Handbook, Volume 18 - Friction, Lubrication, and Wear Technology*. ASM International.
- BOHNE, R. A. & AALBERG, A. 2011. Kompendium i TBA4122 - Bygningmaterialer.
- ÇAM, G. & MISTIKOGLU, S. 2014. Recent Developments in Friction Stir Welding of Al-alloys. *Journal of Materials Engineering and Performance*, 23, 1936-1953.
- CHEN, Y., CLAUSEN, A. H., HOPPERSTAD, O. S. & LANGSETH, M. 2009. Stress-strain behaviour of aluminium alloys at a wide range of strain rates. *International Journal of Solids and Structures*, 46, 3825-3835.
- COCKCROFT, M. G. & LATHAM, D. J. 1968. Ductility and workability of metals. *Journal of the Institute of Metals*, 96, 33-&.
- COOK, R. D., MALKUS, D. S., PLESHA, M. E. & WITT, R. J. 2002. *Concepts and Applications of Finite Element Analysis, 4th Edition*, University of Wisconsin - Madison, John Wiley & Sons Inc.,.
- DASSAULT SYSTEMS 2014. *Abaqus 6.14 - Theory Guide*. 1174.
- DAVIS, J. R. 1993. *Aluminum and Aluminum Alloys*, ASM International.
- DIALOG ON ALUMINIUM. 2012. *Primary Aluminium* [Online]. Dialog on Aluminium: understanding aluminium and its applications,. Available: <http://www.thealuminiumdialog.com/en/aluminium--2/production/primary-aluminum> [Accessed 07.05 2015].
- DICTIONARY OF CONSTRUCTION. 2015. *Dictionary of Construction: Impact load* [Online]. Dictionary of Construction: WebFinance Inc. Available: <http://www.dictionaryofconstruction.com/definition/impact-load.html> [Accessed 10.05 2015].

References

- ENGINEERS HANDBOOK. 2006. *Reference Tables - Coefficient of Friction* [Online]. Available: <http://www.engineershandbook.com/Tables/frictioncoefficients.htm> [Accessed 20.05 2015].
- EUROPEAN ALUMINIUM ASSOCIATION. 2009. *Recycling is critical to sustainable development* [Online]. European Aluminium Association,. Available: <http://www.alueurope.eu/eu-policies/recycling/> [Accessed 21.04 2015].
- EUROPEAN COMMITTEE FOR STANDARDIZATION (CEN) 2008. Eurocode 3: Design of Steel Structures. *Part 1-1: General Rules and Rules for Buildings*. Norwegian Standard.
- EUROPEAN COMMITTEE FOR STANDARDIZATION (CEN) 2009. Eurocode 3: Design of Steel Structures. *Part 1-8: Design of Joints*. Norwegian Standard.
- FOURMEAU, M., BØRVIK, T., BENALLAL, A. & HOPPERSTAD, O. S. 2013. Anisotropic failure modes of high-strength aluminium alloy under various stress states. *International Journal of Plasticity*, 48, 34-53.
- GOTTSTEIN, G., BUESCHER, M. & HIRSH, J. 2010. *Anisotropy Overview* [Online]. alumatter. Available: <http://aluminium.matter.org.uk/content/html/eng/default.asp?catid=99&pageid=1028022659> [Accessed 09.04.2015 2015].
- GRAEVE, I. D. & HIRSH, J. 2010. *T-Temper Process Steps* [Online]. Alu Matter. [Accessed 21.04.2015 2015].
- HANSEN, A. G., AUESTAD, T., TRYLAND, T. & LANGSETH, M. 2003. The kicking machine: A device for impact testing of structural components. *International Journal of Crashworthiness*, 8, 385-392.
- HATCH, J. E. 1984. *Aluminum : Properties and Physical Metallurgy*, Materials Park, OH, USA, ASM International.
- HE, J., ZENG, D., ZHU, X., CEDRIC XIA, Z. & LI, S. 2014. Effect of nonlinear strain paths on forming limits under isotropic and anisotropic hardening. *International Journal of Solids and Structures*, 51, 402-415.
- HILDRUM, H. G. 2002. *Stiffened Aluminium Plates Subjected to Impact Loading*. Dr., Norwegian University of Science and Technology, Faculty of Engineering Science and Technology.
- HOFMANN, P. 1999. *Physics Figures* [Online]. Available: <http://users-phys.au.dk/philip/pictures/physicsfigures/physicsfigures.html> [Accessed 21.04 2015].
- HOPPERSTAD, O. S. 2013. Formability of Aluminium Alloys. Unpublished.
- HOPPERSTAD, O. S. & BØRVIK, T. 2013. *Lecture Notes, Material Mechanics, Part 1*, Structural Impact Laboratory.
- HOSFORD, W. F. & CADDELL, R. M. 1993. *Metal Forming*, Prentice Hall PTR,.

-
- KALLEE, S. W., NICHOLAS, E. D. & THOMAS, W. M. 2001. Friction stir welding - invention, innovations and applications.
- KEY TO METALS. 2010. *Heat treating of aluminium and aluminium alloys* [Online]. Key to Metals - The World's most comprehensive metals database. Available: <http://www.keytometals.com/Article7.htm> [Accessed 10.03 2015].
- KHAN, A. S. & HUANG, S. 1995. *Continuum theory of plasticity*, John Wiley & Sons.
- LADEMO, O. G., HOPPERSTAD, O. S. & LANGSETH, M. 1999. An evaluation of yield criteria and flow rules for aluminium alloys. *International Journal of Plasticity*, 15, 191-208.
- LANGSETH, M., HOPPERSTAD, O. S. & BERSTAD, T. 1999. Impact Loading of Plates: Validation of Numerical Simulations by Testing. *International Journal of Offshore and Polar Engineering*, 9, 6.
- LANGSETH, M. & LARSEN, P. K. 1994. Dropped Objects' Plugging Capacity of Aluminium Alloy Plates. *International Journal Impact Engineering*, 15, 225-241.
- LARSEN, P. K., CLAUSEN, A. H. & AALBERG, A. 1993. *Stålkonstruksjoner: profiler og formler*, [Trondheim], Tapir.
- LIU, B., VILLAVICENCIO, R. & GUEDES SOARES, C. 2015. Simplified analytical method to evaluate tanker side panels during minor collision incidents. *International Journal of Impact Engineering*, 78, 20-33.
- LU, G. & YU, T. 2003. *Energy Absorption of Structures and Materials*. Woodhead Publishing.
- MATHISEN, K. M. 2014a. Lecture notes for course TKT4192 - Finite Element Methods in Strength Analysis. Norwegian University of Science and Technology.
- MATHISEN, K. M. 2014e. Lecture notes for course TKT4197 - Nonlinear Finite Element Analysis. Norwegian University of Science and Technology.
- MEIJERS, S., TERRY, H., GRAEVE, I. D., CAICEDO-MARTINEZ, C., BLEISTEIN, A., RYCKEBOER, M. & ARNOUX, E. 2010. *Impurities in Aluminium* [Online]. Alu matter. Available: <http://aluminium.matter.org.uk/content/html/eng/default.asp?catid=179&pageid=2144416668> [Accessed 17.04 2015].
- MISHRA, R. S. & MA, Z. Y. 2005. Friction stir welding and processing. *Materials Science and Engineering: R: Reports*, 50, 1-78.
- MOREIRA, P. M. G. P., SANTOS, T., TAVARES, S. M. O., RICHTER-TRUMMER, V., VILAÇA, P. & DE CASTRO, P. M. S. T. 2009. Mechanical and metallurgical characterization of friction stir welding joints of AA6061-T6 with AA6082-T6. *Materials & Design*, 30, 180-187.
- NDT RESOURCE CENTER. 2014. *Strengthening/Hardening Mechanisms* [Online]. www.ndt-ed.org: Iowa State University. Available: <https://www.ndt-ed.org/EducationResources/CommunityCollege/Materials/Structure/strengthening.htm> [Accessed 17.04 2015].
-

References

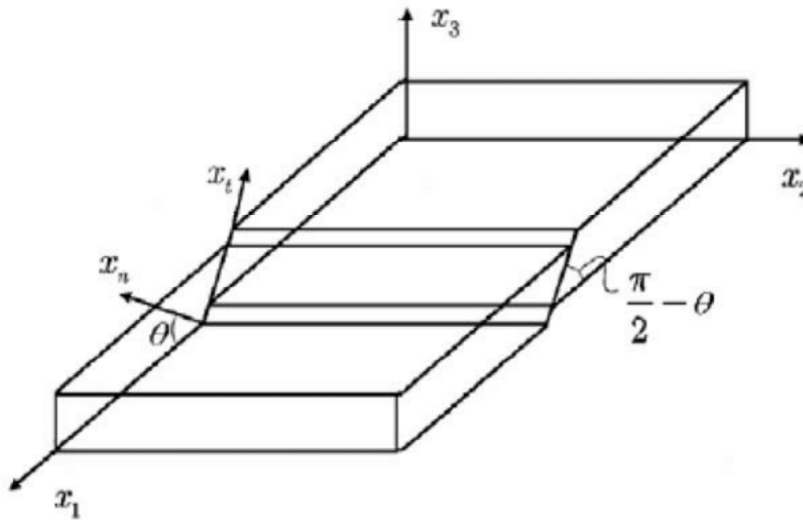
- REINERTSEN AS. 2015. *Kunstig sjøbunn for lange flytebroer* [Online]. Available: <http://www.reinertsen.no/engineering-arkitekt-land/prosjekt?pid=96#> [Accessed 10.06 2015].
- SIMULIA. 2014. *13.4 Energy balance* [Online]. Abaqus 6.14 Documentation - Tutorials. Available: <http://server-afb147.ethz.ch:2080/v6.14/books/gsk/default.htm> [Accessed 22.04 2015].
- STATENS VEGVESEN. 2010. *Ferjefri E39* [Online]. Available: <http://www.vegvesen.no/Vegprosjekter/ferjefriE39> [Accessed 08.03 2015].
- STATENS VEGVESEN. 2014. *Fakta om ferjefri E39* [Online]. Available: <http://www.vegvesen.no/Vegprosjekter/ferjefriE39/Fakta> [Accessed 08.03 2015].
- STATENS VEGVESEN. 2015. *Fjordkryssinger* [Online]. Available: <http://www.vegvesen.no/Vegprosjekter/ferjefriE39/Fjordkryssing> [Accessed 08.03 2015].
- STRUCTURAL IMPACT LABORATORY 2014. SIMLab Metal Model (SMM) - Theory, user's and example manual. 73.
- TAKUDA, H., MORI, K. & HATTA, N. 1999. The application of some criteria for ductile fracture to the prediction of the forming limit of sheet metals. *Journal of materials processing technology*, 95, 116-121.
- TEIRLINCK, D., ZOK, F., EMBURY, J. & ASHBY, M. 1988. Fracture mechanism maps in stress space. *Acta Metallurgica*, 36, 1213-1228.
- TINGSTAD. 2015. *Teknisk informasjon - Merking og fasthetsklasser* [Online]. Available: http://www.tingstad.no/upload_images/A780CD33521044F59352DF00C91AC1E1.pdf [Accessed 07.05 2015].
- VILLAVICENCIO, R. & GUEDES SOARES, C. 2012. Numerical modelling of laterally impacted plates reinforced by free and end connected stiffeners. *Engineering Structures*, 44, 46-62.
- VILLAVICENCIO, R. & GUEDES SOARES, C. 2013. Impact response of rectangular and square stiffened plates supported on two opposite edges. *Thin-Walled Structures*, 68, 164-182.
- WANG, G. 2002. Some Recent Studies on Plastic Behavior of Plates Subjected to Large Impact Loads. *Offshore Mech. Arct.*, 124, 7.
- WANG, G., ARITA, K. & LIU, D. 2000. Behavior of a double hull in a variety of stranding or collision scenarios. *Marine Structures*, 13, 147-187.
- WANG, T. 2006. *Modelling of Welded Thin-Walled Aluminium Structures*. Doctoral thesis, NTNU.
- WEISSTEIN, E. W. 2015. *Kronecker Delta* [Online]. Mathworld - A Wolfram Web Resource. Available: <http://mathworld.wolfram.com/KroneckerDelta.html> [Accessed 20.03 2015].

Appendices

Appendix A

In this appendix, the derivation of the Bressan-Williams shear instability criterion and Hill's local necking criterion is shown.

A.1 – Bressan-Williams shear instability criterion



First, a strain transformation from directions 1,2,3 to t,n:

$$\varepsilon_t = \varepsilon_1 \cdot \left(\cos \left(\theta + \frac{\pi}{2} \right) \right)^2 + \varepsilon_3 \cdot \left(\sin \left(\theta + \frac{\pi}{2} \right) \right)^2$$

set: $\alpha = \theta + \frac{\pi}{2}$ so: $\varepsilon_t = \varepsilon_1 \cdot (\cos(\alpha))^2 + \varepsilon_3 \cdot (\sin(\alpha))^2$

$$(\cos(\alpha))^2 = \frac{1 + \cos(2\alpha)}{2}$$

$$(\sin(\alpha))^2 + (\cos(\alpha))^2 = 1$$

$$\varepsilon_t = \varepsilon_1 \cdot (\cos(\alpha))^2 + \varepsilon_3 \cdot (1 - (\cos(\alpha))^2)$$

$$\varepsilon_t = (\varepsilon_1 - \varepsilon_3) \cdot (\cos(\alpha))^2 + \varepsilon_3$$

$$\varepsilon_t = (\varepsilon_1 - \varepsilon_3) \cdot \frac{1}{2} \cdot (1 + \cos(2\alpha)) + \varepsilon_3$$

$$\varepsilon_t = \frac{\varepsilon_1 - \varepsilon_3}{2} \cdot \cos(2\alpha) + \frac{\varepsilon_1 - \varepsilon_3}{2} + \varepsilon_3 = \frac{\varepsilon_1 - \varepsilon_3}{2} \cdot \cos(2\alpha) + \frac{\varepsilon_1 + \varepsilon_3}{2}$$

The material experiences zero elongation in the t-direction:

$$\varepsilon_t' = 0$$

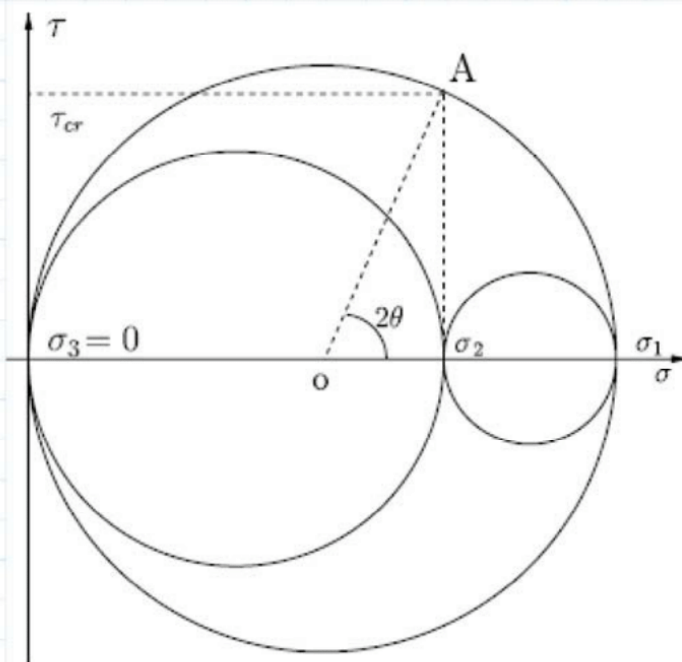
$$\frac{\varepsilon_1 - \varepsilon_3}{2} \cdot \cos \left(2 \left(\theta + \frac{\pi}{2} \right) \right) + \frac{\varepsilon_1 + \varepsilon_3}{2} = 0$$

If: $\cos\left(2\left(\theta + \frac{\pi}{2}\right)\right) = -\cos(2\theta)$

$$\cos(2\theta) = \frac{\varepsilon_1 + \varepsilon_3}{\varepsilon_1 - \varepsilon_3}$$

Plastic incompressibility: $\varepsilon_3 = -\varepsilon_1(1 + \beta)$

$$\cos(2\theta) = \frac{\varepsilon_1 - \varepsilon_1(1 + \beta)}{\varepsilon_1 + \varepsilon_1(1 + \beta)} = -\frac{\beta}{2 + \beta}$$



Mohr's circle gives:

$$\tau_{cr} = \frac{\sigma_1}{2} \sin(2\theta)$$

$$\sin(2\theta) = \sqrt{1 - (\cos(2\theta))^2}$$

This gives the BW criterion:

$$\sigma_1 = \frac{2 \tau_{cr}}{\sqrt{1 - \left(\frac{\beta}{2 + \beta}\right)^2}}$$

A.2 – Hill's local necking criterion

$$\beta = \frac{\Delta \varepsilon_2}{\Delta \varepsilon_1} \quad \alpha = \frac{\sigma_2}{\sigma_1} \quad \sigma_1 > 0 \quad \sigma_2 = \alpha \cdot \sigma_1 \quad \sigma_3 = 0$$

For proportional strain paths:

$$d\varepsilon_1 + d\varepsilon_2 + d\varepsilon_3 = 0 \quad d\varepsilon_1 > 0 \quad d\varepsilon_2 = \beta \cdot d\varepsilon_1 \quad d\varepsilon_3 = -(1 + \beta) \cdot d\varepsilon_1$$

Principal traction in the sheet are defined by:

$$t_1 = \sigma_1 \cdot h \quad t_2 = \sigma_2 \cdot h$$

$$dt_1 = d\sigma_1 \cdot h + \sigma_1 \cdot dh = 0$$

$$\frac{d\sigma_1}{\sigma_1} + \frac{dh}{h} = 0 \quad \frac{d\sigma_1}{\sigma_1} + d\varepsilon_3 = 0 \quad \frac{d\sigma_1}{\sigma_1} - (1 + \beta) d\varepsilon_1 = 0$$

Criterion for local necking: $\frac{d\sigma_1}{d\varepsilon_1} = \sigma_1 (1 + \beta)$

Equivalent Von Mises stress:

$$\sigma_{eq} = \left[\frac{1}{2} \cdot \left((\sigma_1 - \sigma_2)^2 + (\sigma_2 - \sigma_3)^2 + (\sigma_3 - \sigma_1)^2 \right) \right]^{\frac{1}{2}}$$

$$\sigma_{eq} = \left[\frac{1}{2} \cdot \left((\sigma_1 - \alpha\sigma_1)^2 + (\alpha\sigma_1 - 0)^2 + (0 - \sigma_1)^2 \right) \right]^{\frac{1}{2}}$$

$$\sigma_{eq} = \sqrt{1 - \alpha - \alpha^2} \cdot \sigma_1$$

$$\sigma_{eq} = \sqrt{1 - \frac{1 + 2\beta}{\beta + 2} + \left(\frac{1 + 2\beta}{\beta + 2} \right)^2} \cdot \sigma_1$$

$$\sigma_{eq} = \frac{\sqrt{3}}{2} \cdot \frac{\sqrt{\beta^2 + \beta + 1}}{1 + \frac{1}{2}\beta}$$

$$\sigma_1 = \frac{2}{\sqrt{3}} \cdot \frac{1 + \frac{1}{2}\beta}{\sqrt{\beta^2 + \beta + 1}} \cdot \sigma_{eq}$$

$$\frac{d\varepsilon_1}{d\sigma'_1} = \frac{d\varepsilon_2}{d\sigma'_2} = \frac{d\varepsilon_3}{d\sigma'_3} \quad \sigma'_i = \sigma_i - \sigma_m$$

$$\frac{d\varepsilon_1}{2-\alpha} = \frac{d\varepsilon_2}{2\alpha-1} = \frac{d\varepsilon_3}{-(1+\alpha)} \quad \alpha = \frac{2\beta+1}{2+\beta} \quad \beta = \frac{2\alpha-1}{2-\alpha}$$

$$\sigma_{eq} \cdot d\varepsilon_{eq} = \sigma_1 \cdot d\varepsilon_1 + \sigma_2 \cdot d\varepsilon_2 + \sigma_3 \cdot d\varepsilon_3 \quad d\varepsilon_{eq} = \left[\frac{2}{9} \cdot \left((d\varepsilon_1 - d\varepsilon_2)^2 + (d\varepsilon_2 - d\varepsilon_3)^2 + (d\varepsilon_3 - d\varepsilon_1)^2 \right) \right]^{\frac{1}{2}}$$

$$d\varepsilon_3 = 0 \quad d\varepsilon_{eq} = \frac{2}{3} \cdot \left[d\varepsilon_1^2 + d\varepsilon_2^2 - 2 d\varepsilon_1 \cdot d\varepsilon_2 \right]^{\frac{1}{2}} = \frac{2}{3} \cdot \sqrt{\beta^2 - 2\beta + 1} \cdot d\varepsilon_1$$

$$\varepsilon_{eq} = \frac{2}{\sqrt{3}} \cdot \sqrt{1+\beta+\beta^2} \cdot \varepsilon_1$$

Stress based Hill expression: $\varepsilon_1 = \frac{\hat{\varepsilon}_1}{1+\beta}$

$$\varepsilon_{eq} = \frac{2 \cdot \hat{\varepsilon}_1}{\sqrt{3}} \cdot \frac{\sqrt{1+\beta+\beta^2}}{1+\beta}$$

Equivalent stress, Power Law:

$$\sigma_{eq} = K \varepsilon_{eq}^n = K \cdot \left(\frac{2 \cdot \hat{\varepsilon}_1}{\sqrt{3}} \cdot \frac{\sqrt{1+\beta+\beta^2}}{1+\beta} \right)^n$$

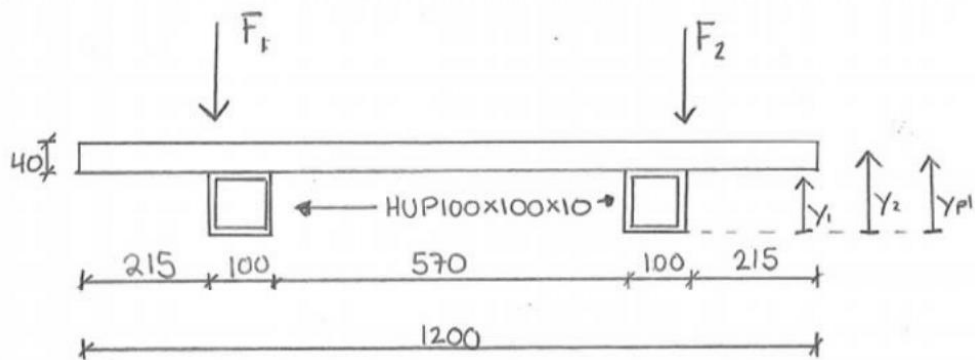
Hill's local necking criterion:

$$\sigma_1 = \frac{2 \cdot K}{\sqrt{3}} \cdot \frac{1 + \frac{1}{2}\beta}{\sqrt{\beta^2 + \beta + 1}} \cdot \left(\frac{2 \cdot \hat{\varepsilon}_1}{\sqrt{3}} \cdot \frac{\sqrt{1+\beta+\beta^2}}{1+\beta} \right)^n$$

Appendix B

In this appendix, the moment capacity of the quasi-static test rig is found.

B.1 – Moment capacity of test rig



NA:

$$A := 40 \text{ mm} \cdot 1200 \text{ mm} + 2 \cdot 3.55 \cdot 10^3 \text{ mm}^2 = (5.51 \cdot 10^4) \text{ mm}^2$$

$$Ay := 40 \text{ mm} \cdot 1200 \text{ mm} \cdot 120 \text{ mm} + 2 \cdot 3.55 \cdot 10^3 \text{ mm}^2 \cdot 50 \text{ mm} = (6.115 \cdot 10^6) \text{ mm}^3$$

$$y := \frac{Ay}{A} = 110.98 \text{ mm}$$

Plastic moment capacity:

$$M_{pl_Rd} = \frac{W_{pl} \cdot f_y}{\gamma_{M0}} \quad \text{for class 1/2}$$

$$f_y := 355 \text{ MPa} \quad \gamma_{M0} := 1.05$$

$$NA_{pl} := \frac{\frac{A}{2}}{1200 \text{ mm}} = 22.958 \text{ mm}$$

$$A_1 := \frac{A}{2} = (2.755 \cdot 10^4) \text{ mm}^2 \quad A_2 := \frac{A}{2} = (2.755 \cdot 10^4) \text{ mm}^2$$

$$Ay_1 := (40 - 23) 1200 \left(100 + \frac{40 - 23}{2} \right) \text{ mm}^3 + 2 \cdot 3.55 \cdot 10^3 \cdot 50 \text{ mm}^3 = (2.568 \cdot 10^6) \text{ mm}^3$$

$$y_1 := \frac{Ay_1}{A_1} = 93.227 \text{ mm}$$

$$y_2 := 100 \text{ mm} + (40 \text{ mm} - 23 \text{ mm}) + \frac{23 \text{ mm}}{2} = 128.5 \text{ mm}$$

$$y_{pl} := 100 \text{ mm} + (40 \text{ mm} - 23 \text{ mm}) = 117 \text{ mm}$$

$$a_1 := y_{pl} - y_1 = 23.773 \text{ mm} \quad a_2 := y_2 - y_{pl} = 11.5 \text{ mm}$$

$$W_{pl} := \frac{A}{2} \cdot (a_1 + a_2) = (9.718 \cdot 10^5) \text{ mm}^3$$

$$M_{pl_Rd} := \frac{W_{pl} \cdot f_y}{\gamma_{M0}} = 328.553 \text{ kN} \cdot \text{m} \quad arm := 235 \text{ mm}$$

$$F_{pl_Rd} := \frac{M_{pl_Rd}}{arm} = (1.398 \cdot 10^3) \text{ kN}$$

Appendix C

In this appendix, material properties of the aluminium alloy AA6082-T6 provided by Sapa is shown.

C.1 – Properties of aluminum alloy, AA6082-T6

Extruded products

Technical datasheet

Alloy EN AW-6082 [Al Si1MgMn]



Medium strength alloy with higher strength than 6005A. Due to elements like manganese, added to increase toughness, it is less suitable for decorative anodising.

Commonly used for structural applications in engineering and transportation due to good toughness and high yield- and ultimate tensile strength. Examples of applications include seat-rails, bumper beams, scaffolding, train-floors, and valve-blocks.

Typical Applications

- Structural beams
- Bumper rails
- Scaffolding
- Train floors

Chemical Composition¹

Si		Fe		Cu		Mn		Mg		Cr		Zn		Ti		Pb		Bi		Sn		Others	
Min	Max	Min	Max	Min	Max	Min	Max	Min	Max	Min	Max	Min	Max	Min	Max	Min	Max	Min	Max	Min	Max	Tot	
0,70	1,30		0,50		0,10	0,40	1,00	0,60	1,20		0,25		0,20		0,10							0,05	0,15

¹ Chemical composition according to EN-573-3:1994

Mechanical Properties^{2 3}

Temper	Wall thickness t [mm]	R _{p0.2} [MPa]	R _m [MPa]	A [%]	A _{50mm} [%]	HBW ^c TYPICAL VALUE	Vickers ^c TYPICAL VALUE	Webster ^c TYPICAL VALUE
T4 ^a	t≤25	110	205	14	12	70	80	14
Open Profile T5	t≤5	230	270	8	6	90	105	16
Open Profile T6 ^a	t≤5	250	290	8	6	95	111	16
	5<t≤25	260	310	10	8	95	111	16
Hollow Profile T5	t≤5	230	270	8	6	90	105	16
Hollow Profile T6 ^a	t≤5	250	290	8	6	95	111	16
	5<t≤25	260	310	10	8	95	111	16

² Properties according to EN 755-2:2008 for extruded profile, minimum values unless else specified

³ If a profile cross section is comprised of different thickness which fall in more than one set of specified mechanical property values, the lowest specified value shall be considered as valid for the whole profile section

^a Properties may be obtained by press quenching

^c Brinell hardness values for information only. Vickers and Webster converted from Brinell value and should be considered approximate

Temper Designations⁴

T4	Solution heat treated and naturally aged
T5	Cooled from an elevated temperature shaping process and then artificially aged
T6	Solution heat treated and then artificially aged
T64	Solution heat treated and then artificially aged in underageing conditions (between T6 and T61) to improve formability
T66	Solution heat treated and then artificially aged – mechanical property level higher than T6 achieved through special control of the process

⁴ Temper designations according to EN 515:1993

Extruded products

Technical datasheet

Alloy EN AW-6082 [Al Si1MgMn]



Physical Properties⁵

Alloy	Temper	Modulus of Elasticity	Modulus of Rigidity	Melting Range	Density	Thermal Conductivity	Specific Heat Capacity	Electrical Resistivity	Coefficient of linear expansion
		[GPa]	[GPa]	[°C]		[W/m·K]	[J/kg·K]	[nΩm]	[10 ⁻⁶ K ⁻¹]
6082		70	26	575 - 650	2,71		897		23,1
	T4					150		41	
	T6					172		39	

⁵ Reference: MNC Handbok nr 12, version 2, SIS, 1989. Typical properties at room temperature 20°C

Comparative Characteristics of Related Alloys⁶

Property	6060	6063	6005	6005A	6082
Tensile strength	1	2	3	3	4
Impact strength	2	2	1	3	4
Surface finish	5	4	3	3	2
Suitability for decorative anodising	5	5	4	3	2
Corrosion resistance	5	5	4	4	4
Machinability	2	3	4	4	5
Coldforming	5	5	4	4	3
Weldability	5	5	5	5	4

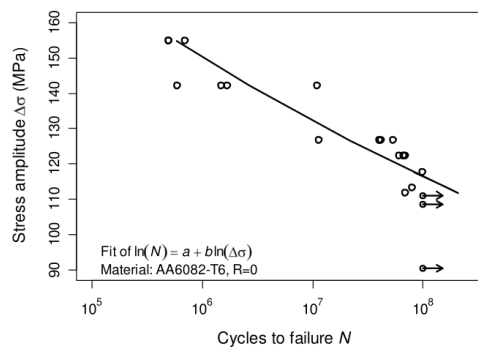
⁶ Relative grading, 5 = top grade

Fatigue Properties

Example of fatigue properties for 6082 in temper T6. Provided for informational purposes only, not to be considered as guaranteed properties. Results are valid for the investigated specimens taken from a specific sample.

Tests performed at 20 ± 2 °C on 7 mm diameter cylindrical specimens parallel to the extrusion direction by Sapa Technology, Finspång, Sweden.

Axial testing, constant amplitude, sine wave loading at around 100 Hz test frequency. Load ratio (min. stress / max. stress) R = 0. Runouts after 10⁸ cycles are indicated by the arrows.



Extruded products

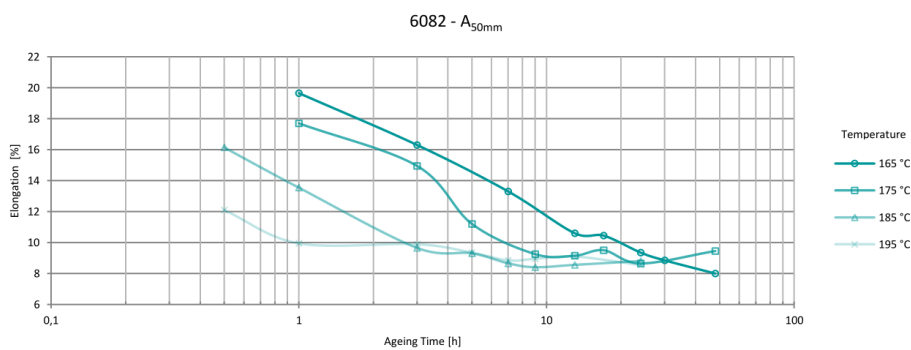
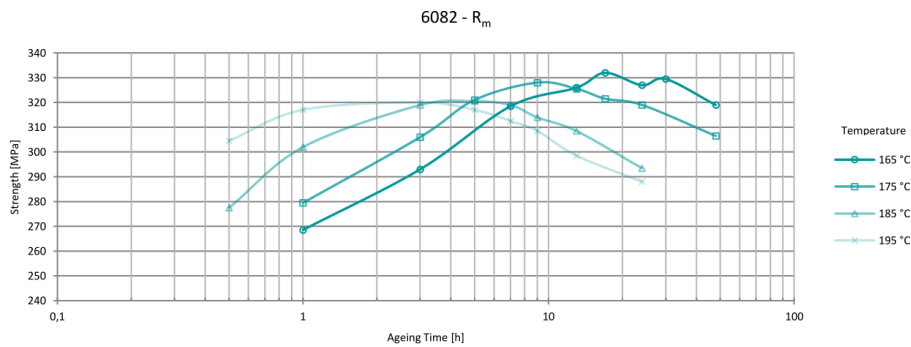
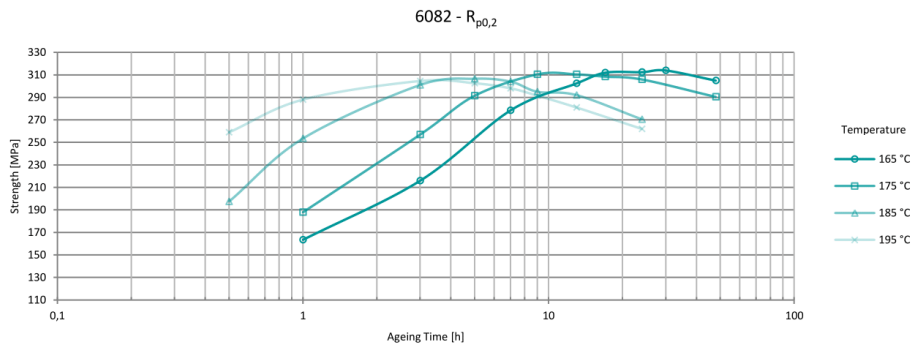
Technical datasheet

Alloy EN AW-6082 [Al Si1MgMn]



Heat Treatment Response

Example of heat treatment response for alloy 6082.



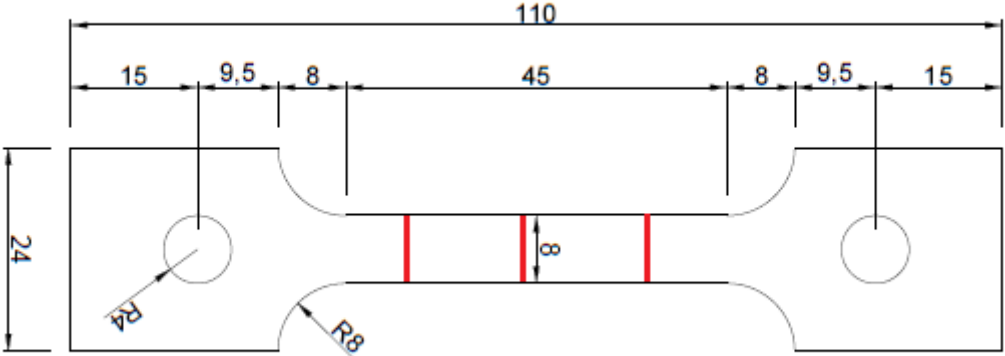
⁷ Solid profile, 200 x 3mm, water quenched after extrusion, 24h natural ageing prior to artificial ageing, samples are taken parallel to extrusion direction

Appendix D

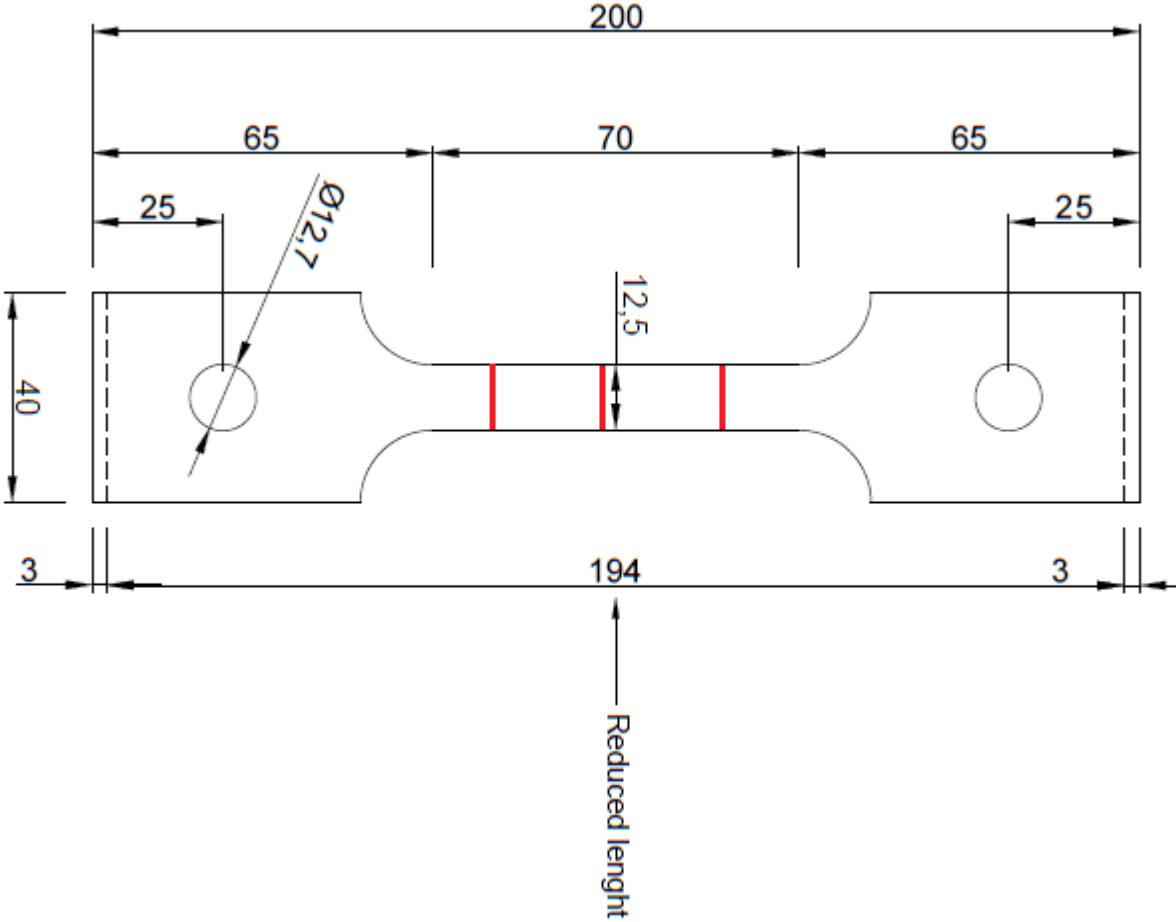
In this appendix, the exact measurements of all specimens in the material tests are included.

D.1 – Measurements of width and thickness of all test specimens in the material test

Measuring points along specimen UT110



Measuring points along specimen UT200



Measurements of tensile tests in base material of top flange and stiffener material, UT110

Test specimen	w [mm]	t [mm]	A [mm ²]	E [MPa]	σ_0 [MPa]	σ_u [MPa]
00-1	7.995	4.292	34.31454	60000	262.278	322.318
	7.992	4.289	34.277688			
	7.992	4.289	34.277688			
00-2	8.007	4.293	34.374051	66000	271.536	320.887
	8.002	4.294	34.360588			
	8.003	4.287	34.308861			
00-3	8.016	4.29	34.38864	66300	272.998	322.904
	8.004	4.286	34.305144			
	8.003	4.287	34.308861			
45-1	8.012	4.114	32.961368	61300	226.48	287.659
	7.995	4.11	32.85945			
	8	4.108	32.864			
45-2	7.994	4.112	32.871328	62500	215.341	284.824
	7.991	4.116	32.890956			
	7.996	4.114	32.895544			
45-3	7.983	4.113	32.834079	62600	243.395	285.807
	7.987	4.111	32.834557			
	7.987	4.115	32.866505			
90-1	8.003	4.293	34.356879	63500	290.079	329.186
	8	4.292	34.336			
	8.003	4.29	34.33287			
90-2	8.013	4.288	34.359744	62700	288.427	329.374
	7.998	4.289	34.303422			
	8	4.289	34.312			
90-3	8	4.29	34.32	62500	284.302	329.23
	7.995	4.29	34.29855			
	7.997	4.292	34.323124			
WEB00-1	7.974	2.849	22.717926	65500	240.977	311.21
	7.979	2.849	22.732171			
	7.973	2.846	22.691158			
WEB00-2	7.974	2.867	22.861458	63000	238.728	311.691
	7.978	2.862	22.833036			
	7.974	2.857	22.781718			
WEB00-3	7.987	2.851	22.770937	67200	258.32	326.3777
	7.988	2.847	22.741836			
	7.987	2.847	22.738989			

Measurements of tensile tests over the FSW, UT200

Test specimen	w [mm]	t [mm]	A [mm ²]	E [MPa]	σ_0 [MPa]	σ_u [MPa]
FSW90-1	12.475	3.901	48.664975	59600	150	256.425
	12.473	3.995	49.829635			
	12.476	4.013	50.066188			
FSW90-2	12.461	3.933	49.009113	60000	150	256.19
	12.456	3.984	49.624704			
	12.471	3.987	49.721877			
FSW90-3	12.484	3.916	48.887344	65000	150	257.24
	12.482	3.988	49.778216			
	12.487	3.97	49.57339			

Appendix E

In this appendix, a selection of the material cards implemented in this master thesis is included along with a malab code for generation of a material card in the BWH instability criterion.

E.1 – Material card for preliminary model

```
*Material, Name = SMM_S355_with_fracture
*Density
7.8e-9
*Include, input = DEPVAR_SMM.inc
*User material, Constants = 25
**      EFLAG,          YFLAG,          RMAPFLAG,          HFLAG,
VFLAG,          TFLAG,          DFLAG,          SFFLAG
          1,          1,          5,          1,
0,          0,          1,          0
**      STFLAG,          E,          PR,          SIGMA0,
SUBSTEP,          THETAR1,          QR1,          THETAR2
          0,          210000,          0.33,          360, 1.00000e-
01,          935.51,          129.02,          861.99
**      QR2,          THETAR3,          QR3,          dRdpmin,
DINIT,          DCRIT,          BIGS0,          PHI
          118.92,          0.0,          0.0,          0.0,
0.0,          1.0,          989,          1
**      EXPS0,
          1
```

E.2 – Material card, Cockcroft-Latham fracture criterion with the Voce rule for base material (BM) and stiffener material (SM)

```
*Material, name=SMM_AA6082T6_WITH_FRACTURE_BM
*Density
 2.7e-09,
*Depvar, delete=61
 61,
*User Material, constants=25
1., 1., 5., 1., 0., 0., 1., 0.
 0., 66000., 0.33, 271.5, 0.1, 36632.4, 17.78,
1350
 90, 0., 0., 0., 0., 1.0, 107.1192,
1.
 1.,

*Material, name=SMM_AA6082T6_WITH_FRACTURE_SM
*Density
 2.7e-09,
*Depvar, delete=61
 61,
*User Material, constants=25
1., 1., 5., 1., 0., 0., 1., 0.
 0., 63000., 0.33, 238.7, 0.1, 63294.55, 36.65,
1462
 86, 0., 0., 0., 0., 1.0, 94.9543,
1.
 1.,
```

E.3 – Material card, Cockcroft-Latham fracture criterion with the power law for base material (BM), stiffener material (SM) and friction stir weld (FSW)

```
*Material, name=SMM_AA6082T6_WITH_FRACTURE_BM
*Density
2.700000e-09,
*Elastic
66000,3.300000e-01
*Plastic
2.715000e+02,      0
2.759858e+02,1.000000e-03
2.798455e+02,2.000000e-03
...
...
4.399037e+02,      1.0
*Depvar, delete=5
5,
1,PEEQ,"equivalent plastic strain"
2,DAMAGE,"Damage Cockcroft-Latham"
3,ratio,"Distance to BWH"
4,beta,"strain ratio"
5,FAIL,"Failure status"
*User Defined Field, properties=8
** Wc, dcrit, BWH,      K,          n, thick,  iptf,  nip
   117.6938,      1,      0, 439.7,  0.09129,  4.0,      0,      5

*Material, name=SMM_AA6082T6_WITH_FRACTURE_SM
*Density
2.700000e-09,
*Elastic
 63000,3.300000e-01
*Plastic
2.387000e+02,      0
2.505090e+02,1.000000e-03
2.583233e+02,2.000000e-03
...
...
4.216479e+02,      1
*Depvar, delete=5
5,
```

```
1,PEEQ,"equivalent plastic strain"
2,DAMAGE,"Damage Cockcroft-Latham"
3,ratio,"Distance to BWH"
4,beta,"strain ratio"
5,FAIL,"Failure status"
*User Defined Field, properties=8
** Wc, dcrit, BWH, K, n, thick, iptf, nip
   101.3674, 1, 0, 421.6, 0.08584, 3.0, 0, 5
```

```
*Material, name=SMM_AA6082T6_WITH_FRACTURE_FSW
```

```
*Density
```

```
2.700000e-09,
```

```
*Elastic
```

```
60000,3.300000e-01
```

```
*Plastic
```

```
150, 0
```

```
1.573611e+02,1.000000e-03
```

```
1.634233e+02,2.000000e-03
```

```
...
```

```
...
```

```
4.274966e+02,1.100000e+00
```

```
*Depvar, delete=5
```

```
5,
```

```
1,PEEQ,"equivalent plastic strain"
```

```
2,DAMAGE,"Damage Cockcroft-Latham"
```

```
3,ratio,"Distance to BWH"
```

```
4,beta,"strain ratio"
```

```
5,FAIL,"Failure status"
```

```
*User Defined Field, properties=8
```

```
** Wc, dcrit, BWH, K, n, thick, iptf, nip
```

```
34.4908, 1, 0, 420, 0.18, 4.0, 0, 5
```

E.4 – Matlab code for generation of material card for the BWH instability criterion

```
clc
clear all
%%%%%%%%%%%%%%%%%%%%%%%%%%%%%%%%%%%%%%%%%%%%%%%%%%%%%%%%%%%%%%%%%%%%%%%%
% Define material parameters
%%%%%%%%%%%%%%%%%%%%%%%%%%%%%%%%%%%%%%%%%%%%%%%%%%%%%%%%%%%%%%%%%%%%%%%%
rho      = 2.7e-9; % Density
E0       = 66000; % Young's modulus
nu       = 0.33; % Poisson's ratio
sigma0   = 271.5; % Yield stress
K        = 439.7; % Power law modulus
n        = 0.09129; % Power law exponent
epspl    = 0; % Yield plateau strain
matname  = 'AA6082T6_BWH_ABAQUS'; % Name of the material card
%%%%%%%%%%%%%%%%%%%%%%%%%%%%%%%%%%%%%%%%%%%%%%%%%%%%%%%%%%%%%%%%%%%%%%%%
% Mesh scaling factor
%%%%%%%%%%%%%%%%%%%%%%%%%%%%%%%%%%%%%%%%%%%%%%%%%%%%%%%%%%%%%%%%%%%%%%%%
element_size = 10; % Shell element size
plate_thickness = 4; % Shell element thickness
scale_factor = (1+plate_thickness/element_size)/2; % Scaling factor
%%%%%%%%%%%%%%%%%%%%%%%%%%%%%%%%%%%%%%%%%%%%%%%%%%%%%%%%%%%%%%%%%%%%%%%%
% Define additional parameters
%%%%%%%%%%%%%%%%%%%%%%%%%%%%%%%%%%%%%%%%%%%%%%%%%%%%%%%%%%%%%%%%%%%%%%%%
p = (0:0.001:3)'; % Equivalent plastic strain
beta = (-0.999:0.001:1)'; % Strain rate ratio
%%%%%%%%%%%%%%%%%%%%%%%%%%%%%%%%%%%%%%%%%%%%%%%%%%%%%%%%%%%%%%%%%%%%%%%%
% Compute stress strain curve
%%%%%%%%%%%%%%%%%%%%%%%%%%%%%%%%%%%%%%%%%%%%%%%%%%%%%%%%%%%%%%%%%%%%%%%%
epsp0 = (sigma0/K)^(1/n)-epspl; % strain for power law
for i=1:length(p)
    if p(i,1) <= epspl
        sigmay(i,1) = sigma0;
    else
        sigmay(i,1) = K*(p(i,1)+epsp0)^n;
    end
end
end
figure
plot(p,sigmay,'r')
grid on
xlabel('equivalent plastic strain')
ylabel('Yield stress')
```

```

csvwrite('yield_stress.csv',[p,sigmay]) % Export the stress-strain curve
for plot
%%%%%%%%%%%%%%%%%%%%%%%%%%%%%%%%%%%%%%%%%%%%%%%%%%%%%%%%%%%%%%%%%%%%%%%%
% Compute BWH
%%%%%%%%%%%%%%%%%%%%%%%%%%%%%%%%%%%%%%%%%%%%%%%%%%%%%%%%%%%%%%%%%%%%%%%%
for i=1:length(beta)
    if beta(i) <= 0.0
        factor1 = 2*K*(1.0+beta(i)/2)/(sqrt(3*(beta(i)^2+beta(i)+1)));
        factor2 = 2*sqrt(beta(i)^2+beta(i)+1)/(sqrt(3)*(1.0+beta(i)));
    else
        factor1 = 2*K/(sqrt(3*(1-(beta(i)/(2+beta(i))))^2));
        factor2 = 2/sqrt(3);
    end
    sig1c(i) = factor1*(factor2*n*scale_factor)^n;
    sig2c(i) = (2*beta(i)+1)/(2+beta(i))*sig1c(i);
end
figure
plot(sig2c/K,sig1c/K,'r')
grid on
xlabel('sigma2/K')
ylabel('sigma1/K')
csvwrite('BWH_locus.csv',[sig2c'/K,sig1c'/K]) % Export the critical
principal stress for plot
%%%%%%%%%%%%%%%%%%%%%%%%%%%%%%%%%%%%%%%%%%%%%%%%%%%%%%%%%%%%%%%%%%%%%%%%
% Write material card
%%%%%%%%%%%%%%%%%%%%%%%%%%%%%%%%%%%%%%%%%%%%%%%%%%%%%%%%%%%%%%%%%%%%%%%%
disp('Write material card');
fich=fopen('mat.inp','w');
% Write material card name
fprintf(fich,['*Material, name=' matname '\n']);
% Write density
fprintf(fich,'*Density\n');
fprintf(fich,'%6d,\n',rho);
% Write elastic properties
fprintf(fich,'*Elastic\n');
fprintf(fich,'%6d,%6d\n',E0,nu);
% Write crushable foam keyword
fprintf(fich,'*Plastic\n');
for i=1:length(p)
    fprintf(fich,'%6d,%6d\n',sigmay(i,1),p(i,1));
end
% Add fracture model
fprintf(fich,'*Damage Initiation, criterion=FLSD\n');

```

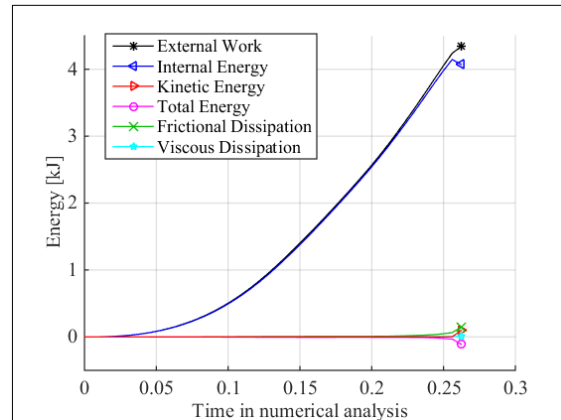
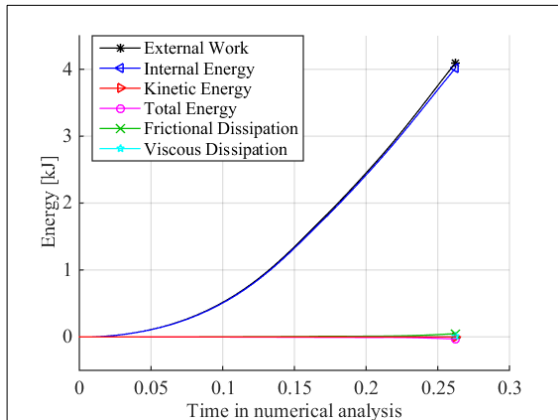
```
for i=1:length(beta)
    fprintf(fich, '%6d,%6d\n', sig1c(i), sig2c(i));
end
fprintf(fich, '*Damage Evolution, type=DISPLACEMENT\n');
fprintf(fich, '%6d,\n', 0.001);
fclose(fich);
```

Appendix F

In this appendix, some additional results from the numerical simulations are included.

F.1 – Additional plots for the Cockcroft-Latham fracture criterion with the Voce rule in transverse and longitudinal direction

Energy plots for CL with Voce rule in transverse (left) and longitudinal (right) direction of the indenter



Force-displacement plots for CL with Voce rule and Hershey yield criterion in transverse (left) and longitudinal (right) direction of the indenter

